Multimode Absorption Spectroscopy of CO and CO_2 Gas Mixtures.

Alexander W. J. Thompson
Christ Church, Oxford

Thesis submitted in fulfilment of the requirements for the degree of Doctor of Philosophy at the University of Oxford

Trinity Term, 2013

Abstract

The development of multimode absorption spectroscopy (MUMAS) for multi-species detection and its potential for process control or environmental monitoring is reported. The simultaneous detection of CO and CO_2 is demonstrated in a proof-of-principle experiment for applications in industrially relevant gas species monitoring. The technique of MUMAS is extended to the near infrared in order to detect these and other industrially relevant species.

A laser was designed and constructed to emit a multimode spectrum in the region of 1.57 µm to take advantage of the spectral overlap of the second vibrational overtone of CO and the combination band $3\nu_1 + \nu_3$ of CO_2. The laser consisted of a semi-confocal cavity employing an Er:Yb glass chip as the gain medium. The laser was pumped by a 1 W laser diode at 980 nm and emitted up to 30 mW in a bandwidth of 180 GHz. The laser emitted between 6-10 modes depending upon the selective cavity length. Mode spacings varied between 18 GHz to 33 GHz with an individual mode linewidth of less than 8 MHz. The laser modes were simultaneously scanned using a piezo-electric transducer (PZT) in order to modulate the cavity length at frequencies between 1 Hz and 10 Hz.

A system for linearizing the MUMAS spectra with respect to frequency was devised based on a transmission spectra of a confocal Fabry-Pérot etalon. Refinements to the MUMAS fitting code were developed to improve the computational efficiency.

An initial demonstration of MUMAS on a known gas mixture of CO and CO_2 was performed. The ratio of CO:CO_2 concentrations in the gas mixture was measured with an accuracy of 0.4% which was within the supplier's quoted uncertainty.

MUMAS is then applied to the detection of CO and CO_2 concentrations in exhaust gas produced by a 1.3 litre 4-cylinder turbo-charged spark ignition engine. Relative and absolute concentrations were derived from MUMAS signals and values compared to measurements using a 4-gas analyser. Concentrations of CO and CO_2 were measured using MUMAS to a precision of 0.17% and 0.23% respectively compared to less than 0.1% for the 4-gas analyser. Ratios of CO and CO_2 were determined with a precision of 0.28 using MUMAS compared to 0.11 with the 4-gas analyser. The detection limit of CO was found to be 1486 ppm in these circumstances.

Finally a discussion is presented of potential improvements arising from wavelength modulation spectroscopy and cavity enhancement techniques.

Dedicated in loving memory to my Godfather

Peter Chadbone

13th January 1938 - 31st August 2011

A truly wonderful role model who gave me and my family so much love and kindness.
You are forever missed.

Acknowledgements

After almost eight years in Oxford a substantial chapter in my life is sadly coming to an end. It's been a roller-coaster ride of amazing highs and unhappy lows, and I'd definitely do it all again! I'd like to thank a number of people in particular for without their help over the years I could not be where I am today.

Firstly, my DPhil could not have been possible without my supervisor Prof. Paul Ewart. Having struggled to decide how I wanted to proceed as a graduate, I am hugely grateful to Paul for giving me this opportunity at an uncertain point of my life. I also want to thank Paul for providing invaluable guidance in overcoming technical problems and for 'thinking out loud', which would often result in a right answer. I'd like to thank the EPSRC for funding me and allowing the group to purchase all of the necessary equipment.

I'd like to thank Dr Benjamin Williams for his crucial contribution to my engine work and his MATLAB intuition, Dr Michelle Hamilton for her insight into spectroscopy and helping me find my feet during the early years, as well as always supporting me when I found it hard going. Fellow DPhil student Henry Northern for his help with writing MATLAB scripts and for all the time we spent in the office bouncing ideas off each other, as well as trying to make it weather-proof. Gratitude also to Prof. Richard Stone who gave me the time to work on the engine. A special thank you to Kai Sun from the Hanson Group at Stanford University for helping me to understand how WMS could be implemented using MATLAB software.

I am forever indebted to Rob Harris (retired) and Mathew Newport from the workshop for their teaching and advice which gave me the skills to build my laser housing, along with many other jobs. Simon Moulder and the rest of the machine workshop for doing the fiddly jobs which I couldn't manage, Richard Makin for his expertise in mirror coatings, the computing department, and the electronics group.

To all my friends at The House and beyond who made my life in Oxford extremely enjoyable. To my best friend Fof forever being the one who could cheer me up. To my other half Sarah, who's stood by me over the last three years and who I've been able to share my Oxford experience with.

Finally to my parents, Bob and Julie, to whom I owe everything. For their unerring and undeviating support throughout my life.

Contents

List of Figures

List of Tables

Glossary

BAS Broadband absorption spectroscopy

BRD Balanced ratiometric detection

$\boldsymbol{c}$ speed of light in vacuum

CAD Computer-aided design

CARS Coherent anti-Stokes Raman spectroscopy

CEAS Cavity enhancement absorption spectroscopy

COSCPEC Correlation spectroscopy

CRDS Cavity ring down spectroscopy

cw Continuous-wave

DFB Distributed feedback laser

DIAL Differential absorption LIDAR

ECDL External cavity diode laser

FP diode Fabry-Pérot diode

FSR Free spectral range

FWHM Full-width-half-maximum

GASMAS Gas scattering media absorption spectroscopy

HWHM Half-width-half-maximum

ICL Interband cascade laser

ICOS Integrated cavity output spectroscopy

IED Improvised explosive device

IR Infrared

$\boldsymbol{k_B}$ Boltzman constant

LASE LIDAR atmospheric sensing equipment

LIDAR Light detection and ranging

MDLCOSPEC Multimode diode laser correlation spectroscopy

MUMAS Multimode-absorption spectroscopy

NASA National Aeronautics and Space Administration

NIR Near Infrared

OF- Optical feedback-

PDM Phasor decomposition method

ppb Parts per billion (by volume)

ppm Parts per million (by volume)

PSD Phase sensitive detection

PZT Piezo-electric transducer

QCL Quantum cascade laser

RADAR Radio detection and ranging

RAM Residual amplitude modulation

SCR Selective catalyst reduction

SI engine Spark ignition engine

SLED Superluminescent light emitting diode

STP Standard temperature and pressure

T Temperature

TDLAS Tuneable diode laser absorption spectroscopy

TEM Transverse electromagnetic mode

TTL Transistor-transistor logic

UV Ultra violet

VCSEL Vertical cavity surface emitting laser

WMS Wavelength modulation spectroscopy

Chapter 1

Introduction

1.1 Motivation

The need for optical sensors in industry and for environmental monitoring is continuing to grow with the desire for systems to be more sensitive, cheap, and robust. Stimulus factors include the constant drive to achieve a more efficient process and government legislation to curb pollution and greenhouse gas emissions [1]. An increasing demand on the use of instruments in-situ and portability has placed a strong emphasis on compact designs as well as robustness. Optical diagnosis devices can also be applied in the medical sciences to offer non-invasive breath diagnoses [2, 3] as well as high purity gas monitoring [4].

To that end techniques have been developed and installed to monitor particular gas species. For example, acetylene impurities are important for the petrochemical industry [5], oxygen sensors for the control of combustion engines [6], and the control of raw gas ingredients used in manufacturing processes.

Carbon dioxide (CO_2) and carbon monoxide (CO) are two very common gases mainly produced as by-products in combustion. Carbon dioxide is non-toxic, but is a common greenhouse gas produced throughout the globe and its emission into the atmosphere is causing our climate to change [7]. Carbon monoxide is also a greenhouse gas with a global warming

potential 1.4 times that of CO_2, however its short residence time reduces its long-term impact [8]. The main motives for monitoring CO emissions are three-fold. Carbon monoxide is:

1. a highly toxic gas,
2. explosive in large quantities and at suitable pressure [9],
3. an indicator of inefficient combustion

Whilst all three reasons are very important the largest economic impact concerns the need for efficient combustion processes. With cost-cutting becoming ever more important in the current economic climate, having an efficient process is essential. To this end a cheap, robust and accurate CO/CO_2 detector could save companies and individuals significant amounts on their fuel bills as combustion occurs in many situations including engines, heating systems and power generation. A CO/CO_2 detection system has been developed which monitors car exhaust emissions from the roadside but this requires a known gas cell for a wavelength reference [10], so an integrated system without the need of a wavelength reference would be potentially more attractive to industry. A single system for detecting multiple species has been developed [11] based on acoustic modulation spectroscopy, but this involves multiplexing four separate laser systems which is expensive.

Multimode absorption spectroscopy (MUMAS) is a direct laser absorption spectroscopy technique that requires one laser and one detector. One system can cover a spectral region of typically 200 GHz which allows for multiple species detection and multiple line detection of the same species. The laser system largely uses off-the-shelf components which keeps costs down and gives it the potential to be easily commercialized. The optical coatings of the mirrors are produced to a custom specification but as this is priced per run, the number produced each time can be scaled up thus decreasing unit cost. By designing the laser to operate in a suitable region, both carbon monoxide and carbon dioxide can be simultaneously detected with a reasonable sensitivity. The ultimate limitation of any detection system is the absorption line strength, which is dependent upon whether the transitions are overtone

or fundamental.

To be a feasible sensor in any combustion process any laser system needs to be small, robust, insensitive to vibrations, and operate on a time scale similar to that of the combustion process. A typical spark ignition (SI) engine will normally operate at 4000rpm which corresponds to a frequency of approximately 67 Hz, so any system ideally needs to respond on a timescale similar to this. Any laser design system needs to take these considerations into account.

1.2 MUMAS overview

The MUMAS technique has already been demonstrated as a feasible spectroscopy technique with high resolution and a large spectral coverage [12, 13, 14]. The solid state erbium micro-laser [13] is to be redesigned such that CO_2 and CO can simultaneously be detected in the near infrared (NIR) and that the laser modewidth is reduced from 1 GHz to a more suitable value in the low MHz range.

MUMAS uses a multiple longitudinal mode laser whereby the optical cavity length specifies the mode spacing. Through modulation of the cavity length these modes are scanned or tuned over the mode spacing interval. If during the scan, any mode comes into resonance with an absorption feature then power will be absorbed. As the modes are scanned simultaneously, the transmitted power spectrum will be a superposition of all the laser modes as they come into resonance with absorption features at different points during the scan. The transmitted intensity yields a characteristic spectrum called the MUMAS fingerprint and is dependent on the absorbing species and the laser parameters.

The MUMAS technique is extremely versatile and how it's implemented depends upon its intended purpose. By simulating and fitting the entire MUMAS spectrum partial pressures of all absorbing gases, total pressure and temperature can be inferred. Alternatively, through monitoring a few specific regions in the fingerprint, via a calibration, gas concentrations can be calculated without the need for extensive computation.

1.3 Thesis structure

The second chapter of this thesis presents a literature review and considers where a MUMAS laser system would fit in with current research and developments. The chapter initially discusses the gases relating to the combustion of fossil fuels and some current experimental sensitivities of their detection are summarized. Next these spectroscopy techniques are reviewed in more detail with their advantages and disadvantages being discussed and compared. Finally, common methods for sensitivity enhancements are mentioned followed by a review of MUMAS.

The third chapter explores the theory behind MUMAS. After introducing the concept of MUMAS, typical physical phenomena are discussed which are required for the correct simulation of the MUMAS fingerprint. The Beer-Lambert Law, spectral line strengths, spectral broadening, basic laser theory and Gaussian optics are all laid out.

The fourth chapter looks at the experimental design of the laser system and the process that led up to its building. The spectral overlap of carbon dioxide and carbon monoxide is investigated and then a suitable laser gain medium chosen. The laser design is shown and the necessary parts to build it are listed. Finally the performance characteristics of the laser system are described with regard to power output, linewidth, smoothness of scanning, mode envelope FWHM, mode envelope threshold and mode spacing.

Chapter five goes through the data analysis procedure which converts the raw data collected into a usable format to allow the simulation to be fitted to it. Steps to filter out some of the signal noise are discussed, and finally the MUMAS simulation code is discussed in detail along with the fitting algorithm.

Chapter six will discuss the application and suitability of using a newly designed laser system to achieve simultaneous detection of carbon monoxide and carbon dioxide from a spark ignition (SI) engine. The data produced from fitting the MUMAS fingerprint to the simulation are then compared to a 4-gas analyser; similar to those found in car service garages. The precision and accuracy of the laser system compared to the gas analyser is also

discussed.

Penultimately, chapter seven will look into the application of sensitivity enhancements to the MUMAS technique and see if WMS can be applied to an actuator modulated cavity.

Finally, chapter eight will look into future enhancements of the current MUMAS laser design, the application of quantum cascade lasers to carbon monoxide/carbon dioxide detection in the mid infrared and propose further research into detection of ammonia using a micro-cavity laser. The long term MUMAS application to medical diagnostics will be touched upon and finally the main conclusions from this thesis will be summarized.

Chapter 2

Gas sensing techniques

Common gas species from combustion, industrial processes, and environmental pollutants are first discussed and achieved experimental precisions and uncertainties are catalogued. The motivation of designing a cheap and robust simultaneous CO and CO_2 detector is discussed. Particular spectroscopic techniques are then examined and their advantages and disadvantages compared. Finally, MUMAS is introduced and some initial experimental work is summarized.

Gas sensing plays a pivotal role in many situations including industrial processes, breath analysis, efficiency monitoring, pollution/environmental control, and national security. The required characteristics of each gas sensing system are dependent not just upon what species are being detected and the desired sensitivity, but also typical response time, operating environment, and operational lifetime. Numerous techniques have been proposed, built and tested with each having their own advantages and disadvantages.

In-situ monitoring systems can be difficult to build and install for field applications of monitoring processes such as atmospheric pollutants, incinerator operation or power production in furnaces. The harsh, noisy and potentially volatile environment poses many challenges to the design and construction of the apparatus and can frequently lead to degradation and failure of the system. In this chapter, a review of different gas spectroscopy techniques will be given as well as the description of several methods which aim to improve the experiment's sensitivity. Applications of the technology will also be discussed. Typical species detected, sensitivities, precisions and construction will be analysed and the requirements of partic-

ular applications will be considered. The ideal monitoring system for any task would be small, robust, have low fabrication costs, high resolution, operate over a broad bandwidth, reasonable output power level and high immunity from vibrations, temperature fluctuations and other noise sources [15]. The importance of each of these parameters will vary between applications and environments, as well as depending upon target market, available finances and technological developments.

Where possible a standardized approach to quoting detection limits and sensitivity has been undertaken. The detection limit, or minimum detectable amount, is defined as the smallest concentration that can be detected with reasonable confidence i.e. when the signal-to-noise ratio equals one. This can also be referred to as the noise equivalent signal (NES) and is typically normalized by path length and the square root of detection bandwidth:

$$\mathrm{NES} = \frac{\text{minimum detectable absorbance}}{\sqrt{\text{detection bandwidth}} \times \text{path length}}, \tag{2.1}$$

where the detection bandwidth is the measurement frequency divided by the number of averages. The units of NES are typically $\mathrm{cm^{-1}\,Hz^{-0.5}}$. Some literature references will refer to the minimum detectable amount by converting the minimum detectable absorbance into a concentration, such as parts per million. This instead results in a noise equivalent concentration, which is normalized in the same manner as to equation 2.1, and has units of $\mathrm{ppm\,m\,Hz^{-0.5}}$.

2.1 Combustion

Gas sensing is an important aspect of combustion diagnostics. Detection of gas species is often required in exhaust emissions or inside combustors such as the combustion chambers of engines. The main products of combustion from a simple fuel such as methane are:

1. Carbon dioxide (∼14%)
2. Carbon monoxide (∼0.1%)

3. Water (∼12%)

4. Nitrogen oxides (∼0.1%)

5. Unburnt hydrocarbons (∼0.1%)

In principle monitoring of these gases can be used to control the fuel/air ratio being injected into the engine which in turn can influence the efficiency and power output. Extensive research has gone into producing monitoring devices for water, carbon dioxide and carbon monoxide.

2.1.1 Carbon dioxide

A controlled greenhouse gas, carbon dioxide accounts for one of the largest controlled substances emitted into the atmosphere as a by-product of any fossil fuel combustion by mass. Some 34 billion tonnes were emitted in 2011 globally and it is feared that this may be causing our climate to change [16]. Being a trivalent molecule, carbon dioxide has numerous absorption bands across the spectrum as it has 4 vibrational modes - symmetric (ν_1), asymmetric (ν_2) and two degenerate bending modes (ν_3). As such, combinations of fundamental and overtone transitions produce the CO_2 spectrum. Examples include the combination $3\nu_1 + \nu_3$ transition in the NIR around 1.5 µm, the $\nu_1 + \nu_3$ combination band near 2 µm and the ν_3 fundamental band in the IR around 4 µm. The absorption line strength is significantly greater in the fundamental bands, but the detector technology is not as developed. Background noise is far greater in the mid IR due to blackbody radiation from all of the surrounding objects.

Gas monitoring systems utilizing the fundamental absorption bands at 4.3 µm have attained minimum detectable levels of 150 ppb (581 ppmHz$^{-0.5}$) using differential absorption LIDAR[1] (DIAL) [17] and 40 ppb (NES = 6.15 ppb m Hz$^{-0.5}$ or 1.96×10^{-6} cm^{-1}Hz$^{-0.5}$) using tuneable diode laser absorption spectroscopy (TDLAS) utilizing a distributed feedback quantum cascade laser (QCL) [18]. Systems based upon 2.0 µm radiation have produced a

[1] Light detection and ranging

minimum detectable change of 0.2% [2], with 1-2% precision using the DIAL technique [19], and 59 ppm m^{-1} (NES = 8 ppm m Hz$^{-0.5}$ or 3.5×10^{-4} cm^{-1}Hz$^{-0.5}$) using a novel hollow-core photonic bandgap fibre as the gas cell [20]. Using photoacoustic methods in the overtone region between 1500 nm to 1600 nm, minimum detectable amounts of 171 ppm (NES = 28 ppm Hz$^{-0.5}$ or 3.6×10^{-10} cm^{-1} W Hz$^{-0.52}$) [21], 153 ppm m at 1000 K [22], and even as low as 300 ppb (NES = 1.7×10^{-10} cm^{-1} W Hz$^{-0.5}$) for 100 s acquisition time [23] have been achieved.

The first in-situ combustion measurements of carbon dioxide were performed by Mihalcea et al [24] using a room temperature external cavity laser diode operating at 2 µm. A minimum detectable amount of 200 ppm (14 ppm m Hz$^{-0,5}$) was achieved at an exhaust gas temperature of 1470 K. This monitoring system also detected a water transition and utilized the ratio of the integrated line intensities to determine the temperature. Earlier work by Mihalcea et al [25] demonstrated the multi-species detection of the previously described laser in detecting carbon monoxide, carbon dioxide, methane and hydroxide radicals. The large spectral output range of the laser system allowed for such a variety of detectable species, however simultaneous detection was not permissible. The narrow mode-hop-free tuning range of the laser prevented this, being restricted to 1.2 cm^{-1}.

It is also worth noting that a significant amount of research has gone into carbon isotope identification where the emphasis is on determining the ratio of ^{13}C to ^{12}C. Detection limits have been reported of between 16 ppb to 5000 ppb with a precision of 0.003% and accuracy of 0.13% [26, 27, 28, 29].

2.1.2 Carbon monoxide

Carbon monoxide is a diatomic molecule with a carbon to oxygen triple bond. As a simple diatomic molecule, carbon monoxide only has one fundamental vibrational mode. This limits the number of absorption transitions the molecule has, when compared to triatomic molecules

[2]The signal detected from photoacoustic absorption spectroscopy is proportional to the laser power transmitted through the target gas.

such as water or carbon dioxide. Carbon monoxide like carbon dioxide has absorption lines in the NIR and mid-IR, which are in the region of 1570 nm (second vibrational overtone), 2.3 µm (first vibrational overtone) and 4.7 µm (fundamental vibrational mode). Minimum detectable amounts vary from 2 ppb (NES = 1.48×10^{-8} cm^{-1} W Hz$^{-0.5}$) for TDLAS using QCLs, to 250 ppm (NES = 3.4×10^{-9} cm^{-1} W Hz$^{-0.5}$) for DFB lasers in the NIR [30, 11]. The first detection of carbon monoxide at 2.35 µm was performed by Nicolas et al [31] using a multiple-quantum-well laser operating near room temperature. The laser could be temperature-tuned across 150 GHz of continuous spectrum and had a linewidth of 20 MHz. Following technological improvements, Wang et al [32] utilized a room temperature operated semiconductor laser to perform in-situ measurements of carbon monoxide in the exhaust duct and directly above a burner. Direct absorption yielded a sensitivity of 1.5 ppm m (NES = 8.3×10^{-8} cm^{-1} Hz$^{-0.5}$) whilst WMS improved that figure to 0.1 ppm m. This setup was entirely battery powered which demonstrates its suitability for in-situ measurements.

As an indicator of complete combustion carbon monoxide has been monitored in exhaust gases from a variety of sources. Detection from a boiler exhaust utilizing pulverized coal as fuel yielded a dynamic range of 6 ppm to 10 000 ppm for a 2300 nm system [33]. Shock tube measurements have shown a temperature precision of 0.8% between 1100 K to 2000 K for a measurement frequency of 2.5 kHz using a QCL at 4.7 µm [34]. Acquisition rates of 10 kHz [35] and even as high as 50 kHz have been achieved in shock tube experiments [36].

Houston Miller et al [37] performed an early demonstration of tuneable diode lasers for in-situ diagnostics of laminar hydrocarbon diffusion flames. Utilizing a cryogenically cooled lead-salt crystal operating near 4.7 µm, the temperature and carbon monoxide concentration profile of the flame was produced.

Along with acetylene, carbon monoxide has been studied in atmospheric observations using aircraft-borne monitoring systems [38]. The origin of these two gases from combustion are strongly correlated in atmospheric observations, offering constraints on atmospheric dilution and chemical ageing. In this instance, the observations were interpreted using a global chemical transport model.

Carbon monoxide is naturally produced in the body by the breakdown of haemoglobin and is also used by the body as a natural anti-inflammatory. It is a biomarker for hyperbilirubina and asthma, and is found in increased quantities in the breath of smokers [3]. A very sensitive detection system is required owing to the low concentrations encountered in human breath. These detection levels needed for human breath are far lower than those normally encountered in combustion exhaust gas, and it is anticipated that the present work will not be sufficiently sensitive.

2.1.3 Water

Water is a nonlinear triatomic molecule and has a large abundance of absorption lines over all of the spectrum. Notable regions of reduced absorption include the visible region as that is where the human eye is sensitive. Other than in combustion water vapour can be found in exhaled breath and occurs naturally in the atmosphere. Humidity detectors in controlled atmospheric environments are vital if delicate and old objects are to be stored correctly, most notably books, ancient mummies and other organic items which will absorb water over time and deteriorate.

A convenient region to detect water is between 1370 nm to 1390 nm as there are very strong bands and laser sources are readily available. A smallest detectable difference of 0.003% absorption with 10 ms resolution has been achieved [2]. As water vapour is a by-product of combustion it can be used as a marker to identify the conditions within the combustion chamber of an engine. The ease of use of this technology has even allowed in-cylinder detection of water to be studied as this can give information concerning the pressure and temperature during the combustion cycle of a spark ignition (SI) engine. A limit if detection of 285 ppb m $Hz^{-0.5}$ to 477 ppb m $Hz^{-0.5}$ with a time resolution of 250 µs [39], as well as 40 K precision [40] with a 5% accuracy [41] have all been achieved using in-cylinder spectroscopy. All of these experiments utilized DFB semiconductor lasers. The work reported by Mattison et al [41] involved wavelength multiplexing of three laser systems together and used a photo-acoustic cell for the detection of the absorption resonances.

Water has also been detected using LIDAR with precision of better than 10% using an 815 nm titanium sapphire 30 ns 150 mJ pulsed laser which allowed measurements to be taken between 16 km to 21 km altitude above sea level [42].

2.1.4 Nitrogen oxides

Nitric oxide (NO) and nitrogen dioxide (NO_2) are produced through the oxidation of nitrogen due to high-temperature oxidation mechanisms (e.g. Zel'dovich) present during the combustion cycle. The final product of nitrogen dioxide is a reddish brown gas that is toxic, a pollutant, and an environmental hazard. In an effort to make combustion processes as efficient as possible excess air can be pumped into the chamber to cool the vessel and so reduce the thermal NOx production.

In-situ detection of NO has been demonstrated on diesel engine exhaust gases [43]. A detection limit of 50 ppb was demonstrated over a measurement time of 20 seconds. Likewise NO_2 has been detected in exhaust gases but only with a sub parts per million limitation [44].

NO is naturally produced by the human body in a process relating to blood pressure control. It is present in human breath and less than 1 ppb has been detected using QCLs [45]. Similar detection sensitivities for NO_2 have also been demonstrated [46]. Considerably increased sensitivity from MUMAS would be necessary for such an application. This is theoretically possible but the current technology of MUMAS is not sufficient to offer the necessary detection limits.

2.1.5 Selected other species

Ammonia

Ammonia is an important molecule in breath analysis, soil fertility, nitrogen oxide reduction from exhaust gases and national security by aiding in detection of explosives in IEDs (Improvised explosive device). Ammonia is a biomarker for renal failure and oral cavity disease

and is normally found in human breath at concentrations of a few parts per million [3]. The ammonia cycle plays a crucial role in allowing plant life to absorb nitrogen as nitrogen from the atmosphere cannot be directly assimilated. Ammonia needs to be present in the soil, however leaching into water systems can be extremely harmful to any aquatic life so close monitoring of fertiliser being used on fields is essential. Ammonia has also been identified as a potential reagent for the removal of NOx through selective catalyst reduction (SCR). Ammonia deposited in the form of NH_4^+ ions on a metal surface interact with the nitrogen oxides to reduce them to nitrogen [47]. However, too much ammonia would result in the release of a pollutant into the atmosphere, so high speed ammonia detection schemes would be needed if this NOx removal scheme were to be implemented in diesel engines. Finally, ammonia can be used as a marker for the detection of homemade explosives. Whilst the vast majority of explosives will leave a residue trail giving a unique spectrum they are often difficult to produce or get hold of. Ammonia-based explosives can be easily made from fertiliser and other of-the-shelf ingredients. Ammonium nitrate salt has a vapour saturation pressure of 29 ppb at 35 °C and so trace amounts should be easily detected on clothes and objects of anyone who has been in contact with such materials. The required minimum detection level would have to be in the region of 5 ppb [48]. By utilising the 10 µm spectral bands of ammonia, 25 ppb detection limit (NES = $1.5 \times 10^{-6}\,\mathrm{cm^{-1}\,Hz^{-0.5}}$) has been demonstrated with a 1 s measurement time [49]. This could be a suitable system for national security purposes, especially as signal-to-noise enhancements have been proposed. It would however not be suitable as a monitoring device for the removal of NOx gases as the sampling time needs to be substantially shorter.

Methane

Methane is a powerful greenhouse gas with a 3.7 times stronger global warming effect than carbon dioxide when released into the atmosphere [8]. Due to methane's natural scarcity from the atmosphere the effect of introducing the next tonne of CH_4 to the atmosphere has a stronger global warming effect than the previous tonne - an exponential trend.

Sources of methane in the atmosphere are a complex subject and the interaction between sources and sinks is not fully understood. Natural sources include wetlands and certain animals such as termites. Non-natural sources of atmospheric methane include decomposition of landfill sites, rearing livestock, sewage and waste treatment, and biomass burning. There are natural mechanisms which remove methane from the atmosphere. One of the main processes carried out is by the methanotrophic bacteria present in soil. The most effective sink however is the hydroxyl radical present in the troposphere. The reaction of methane with hydroxyl ions produces only water and carbon dioxide [50].

2.1.6 Multi-species detection systems

Numerous monitoring systems have been developed which can detect multiple species simultaneously. A diode laser based system developed by Gabrysch et al [51] allowed for simultaneous detection of carbon monoxide and carbon dioxide at 1578 nm. In addition, environmentally and spectroscopically relevant self-broadening and nitrogen broadening coefficients for both gases were measured for the first time. A limit of detection of $500\,\mathrm{ppm\,m^{-1}}$ for carbon monoxide and $800\,\mathrm{ppm\,m^{-1}}$ for carbon dioxide (NES $= 5.4 \times 10^{-6}\,\mathrm{cm^{-1}\,Hz^{-0.5}}$) was achieved. In related work, a spectral survey of carbon monoxide and carbon dioxide was performed by Sonnenfroh et al [52] using a semiconductor diode laser centred at 1.57 µm. Although capable of simultaneous detection, this system was used to verify the line position and strength of the two gases individually. Another system for simultaneously detecting CO and CO_2 has been demonstrated by Oh et al [53] which uses frequency modulation multiplexing to mix two laser frequencies - 1.548 µm and 1.558 µm for CO_2 and CO respectively. Each laser was modulated at a different frequency which allowed separate demodulation by different lock-in amplifiers.

A novel laser design by Upschulte et al [54] produced a quasi-continuous tuning range of over 100 nm near 1550 nm. This laser system simultaneously detected carbon monoxide and carbon dioxide in room temperature gas mixture, however the laser did mode hop so a continuous sweep was not possible. A detection limit on this work was not possible due

to the uncertainty in the detector output near to the mode hop regions. There is also an uncertainty in the absolute frequency calibration of the current laser system. Secondly, in-situ measurements of CO, H_2O and OH in the exhaust gas of a methane/air flame were performed. These gases were not measured simultaneously as the laser had to be tuned to a specially chosen spectral window. This latter study was the first observation of in-situ flame measurements of CO and OH by use of a NIR laser diode.

The first example of a NIR diode-laser-based absorption spectrometer that performed simultaneous in-situ measurements of carbon monoxide, water vapour and temperature in the combustion chamber of a 600 MW lignite-fired power plant is described by Teichert et al [55]. This system utilized two separate lasers - one for each gas detected. A detection limit of 200 ppm (NES = $4.4 \times 10^{-6}\,\mathrm{cm^{-1}\,Hz^{-0.5}}$) was achieved with a measurement time of 30 s. The laser and optical components were water cooled to protect them from the heat produced in the furnace. A pure carbon monoxide gas cell was used as a wavelength reference.

Another example of multi-species detection was performed by Ebert et al [56]. This is the first reported example of simultaneous in-situ detection of oxygen and water vapour in a full-scale incinerator using a AlGaAs diode laser. Real time monitoring of the gases was demonstrated on a time scale of one second. Two separate lasers were employed for this purpose and the correction applied to the detected signal due to light scattering off aerosols was successfully done using an analogue algorithm.

A femtosecond laser frequency comb could also be utilized to detect multiple species simultaneous [57]. A wide spectral coverage in excess of 1 THz and narrow linewidth is possible with this system. However high cost and complex detection methods typically exclude this technique from in-field applications.

2.2 Species summary

Some common gas species have been discussed as an indicator or marker for various combustion analysis, medical applications, and environmental monitoring. The detection methods

are highly dependent upon the situation and circumstances in which the measurement will take place. The desired resolution, spatial coverage, time response, number of gases measured and other factors vary dependent upon the technique used.

Given the selection of common gas species discussed, a sensible demonstration of the application of MUMAS to an industrially relevant process would be to simultaneously monitor carbon dioxide and carbon monoxide. Fuel combustion occurs globally often at a great cost to the user. Monitoring systems that can increase combustion efficiency will save money as well as monitoring greenhouse gas emissions. Any device which could perform such a task in-site and in real time that is robust, cheap to manufacture and easy to use, could become a vital tool in tackling fossil fuel use and curbing greenhouse gas emissions. This test case could also be a starting point for the use of MUMAS as an in-situ monitoring device for multi-species gas detection in process control or other industrial operations. The NES of any suitable MUMAS setup would preferably be of the order $1 \times 10^{-7}\,\mathrm{cm}^{-1}\,\mathrm{Hz}^{-0.5}$ or better.

The next part of this chapter will look closely at some of these spectroscopy techniques and comment further on their advantages, drawbacks, ease of use and cost.

2.3 Spectroscopic techniques

Most spectroscopy techniques require a line-of-sight through the sample gas and thus optical access. (Some techniques do not require a direct line-of-sight through the sample, but still need optical access as they utilize backward scattering.) Generally, variation in the transmitted power through the line-of-sight beam path will be used to infer information on the gas or gases. The type of light used depends on the requirements of the particular measurement as well as the apparatus used. Commonly, lasers will be used as light sources because of their mostly single wavelength emission and their output can be collimated.

2.3.1 Tuneable diode laser absorption spectroscopy

TDLAS is a simple method of determining the presence of gas species by measuring the changes in the transmitted laser power. Semiconductor diode lasers often have narrow laser line widths and can be tuned over a spectral distance typically of only 30 GHz by the application of an amplitude modulation to the driving current. Their narrow linewidth means they are suitable for high resolution spectroscopy; however, the limited tuning range is rather restrictive because a spectral window has to be identified in order to avoid spectral interferences. This can often lead to a single laser being able to only identify one species.

The semiconductor diode laser was first demonstrated in 1962 by the emission of coherent light from a gallium arsenide semiconductor junction [58]. By driving a current through the junction holes and electrons recombined to emit coherent photons. The frequency of each photon could be set chiefly by the width of the energy gap across the junction and then fine-tuned by either temperature or the magnitude of the current. Now, over fifty years later, the semiconductor laser has been heavily developed and can boast numerous designs due to the wide range of elements that can be used to determine the energy gap. As a result, semiconductor lasers have a wide range of emission wavelengths and their diversity has led to them being employed in high resolution spectroscopy of gases, often referred to as tuneable diode laser absorption spectroscopy (TDLAS).

A problem with semiconductor lasers is their tendency to operate on multiple modes. Whilst not necessarily a problem in itself, it can make their power output rather erratic and unpredictable whilst tuning and during operation [59]. The laser cavity of a semiconductor laser can be modelled as a Fabry-Pérot cavity and hence has a restricted output such that only frequencies which match the boundary conditions of the cavity are permitted to build their intensity. The free-spectral range $\Delta\nu$ of a cavity of length L and refractive index n is given by

$$\Delta\nu = \frac{c}{2nL}, \tag{2.2}$$

where c is the speed of light. So if the spectral gain width is larger than $\Delta\nu$ then multiple

modes could be output. This is usually undesirable and there are possible design alterations which can eliminate this behaviour.

A typical TDLAS setup is simple to implement and a schematic is shown in figure 2.1. The main elements are the single mode laser and its driver, which is tuned by a function

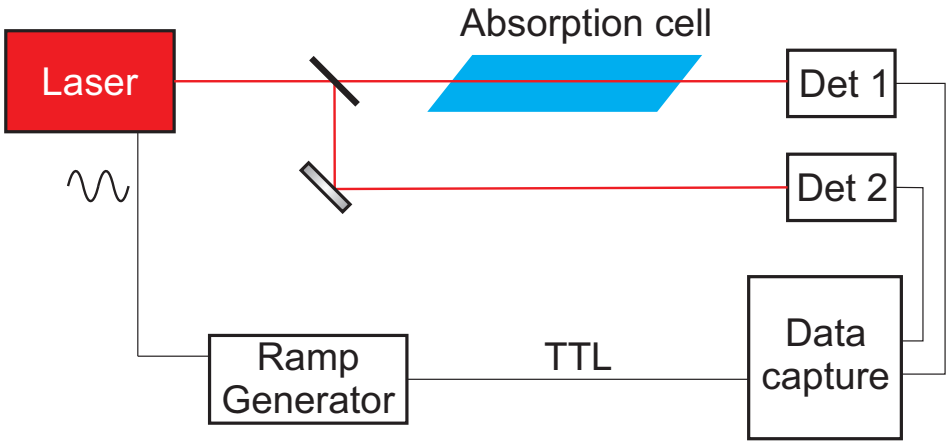

Figure 2.1: The basic setup of TDLAS. The laser source is tuned by the oscillatory signal from the ramp generator and the direction of the emitted radiation is represented by the red line. The light is split and part is sent through the sample gas (blue) and the power detected by Det1, and the other reference beam is monitored by Det2. Both data feeds are then captured and analysed using the TTL pulse to trigger.

generator; a gas cell of known optical length with angled windows to reduce etalon effects; a detector and data storage, which is often an oscilloscope or computer. A trigger from the function generator is fed into the data capture system.

2.3.2 Diode lasers

Distributed feedback laser

The distributed feedback (DFB) laser works on the principle that one of the cavity mirrors is replaced by an integrated Bragg reflector. This feeds back only a narrow band of frequencies into the cavity, which when combined with the boundary conditions of the cavity results in single mode operation. As the gain is concentrated in a single mode the amplification naturally narrows the line width. This means that spectral resolution of 1 MHz or below is readily obtainable. By altering the temperature the lattice spacing in the Bragg diffraction

structure will change as the refractive index is dependent upon this parameter. This allows the output wavelength to be tuned over a reasonable range.

The DFB laser will provide a very stable power output and high resolution spectroscopy can be performed. However the tuning range of such a device is limited by the temperature range that can be safely applied and such temperature changes cannot be implemented at high frequency. Current tuning can be applied at frequencies well over 1 kHz however the tuning distance is severely limited by the magnitude of the current that can be driven through the semiconductor junction.

The DFB laser response to current tuning is repeatable and predictable thus allowing the baseline to be subtracted from the captured signal without the need to record a separate measurement. Provided the scanning distance is much larger than the absorption width, a substantial part of the spectrum will represent only the power modulation of the DFB laser. A polynomial can be fitted to this power modulation signal and the baseline will be extrapolated across the region where the absorption feature exists. This can be implemented very easily in software analysis and is a commonly used technique in laser sensing. If the desired absorber is present in the background (for example carbon dioxide or water, and part of laser beam passes through the air) then this polynomial fit will not work. Instead, a background measurement of an empty gas cell can be recorded prior to the data measurement and divided away in the data processing. Another possibility would be to contain the laser beam in a controlled atmosphere, such as argon or nitrogen, however this increases the cost and complexity of the sensing system.

Vertical-cavity surface-emitting laser diode

Semiconductor diodes can be chiefly split into two different designs, edge-emitting (such as DFB lasers discussed in section 2.3.2) whereby the coherent light is emitted parallel to the wafer, or surface emitting lasers which emit light perpendicular to the wafer [60]. Vertical-cavity surface-emitting lasers (VCSEL), can produce much larger power outputs than their edge-emitting counterparts and due to their extremely short cavity length, which can be

around 5 µm, their intrinsic mode spacing will be very large (180 nm in this case) and only a single mode lies within the gain bandgap [61, 62].

VCSEL diodes can produce a very high quality and high power circular beam which is ideal for absorption spectroscopy. Like DFB lasers, they have to be tuned via current modulation or temperature and they will therefore have similar limitations on their usage. However, the extra-short cavity involved means that the round trip gain will be much less than an edge-emitting diode so extremely high reflective coatings are needed. Often 100% and 99% reflection coatings are needed on the two boundaries. Their high tuning range make them preferable candidates for local gas sensing and multi-species detection. However, VCSELs have relatively broad linewidths (∼50 MHz) due to the low gain in the system and they also have limited availability in operational wavelengths due to the limited number of suitable materials available to produce the junction [63].

VCSEL diodes have unstable features during their operation even without any external perturbations. Spatial structures and the polarisation modes give rise to chaotic dynamics and spatial hole burning and multi-transverse mode oscillations are often observed [64].

Distributed Bragg reflectors can be incorporated into VCSEL diodes, however DFB is usually reserved for edge-emitting laser diodes.

A microelectromechanical-system (MEMS)-tuneable single mode VCSEL has been developed which can record absorption spectra over 60 nm in a single sweep [65]. Operating near 1.58 µm this laser system was used to detect over 30 absorption lines of CO or CO_2 in a single sweep. The laser scan was performed at a rate of 5 Hz as the limiting factor in the experiment was the data acquisition rate. A 12 bit data acquisition card with 200 kHz bandwidth was used and 20000 data points captured at 100 kHz were recorded.

The experimental setup of VCSEL absorption spectroscopy is very similar to TDLAS, shown in figure 2.1. Compact and portable detection systems have been built and tested that use VCSELs. Atmospheric CO_2 monitoring has been performed using a 2 µm VCSEL both in the laboratory and in the field. A limit of detection of 140 ppb was detected from

a 1 s acquisition (NES = 0.49 ppm m $Hz^{-0.5}$) and the setup was contained within a portable cell of 16 cm x 24 cm x 9 cm in size [66].

Quantum cascade laser

Quantum cascade lasers are a type of semiconductor laser that were first demonstrated in 1994 at the Bell Laboratories [67]. They emit radiation in the infrared (IR), but unlike semiconductor diode lasers which utilize electron-hole recombination, QCLs are unipolar and laser emission is generated through the use of inter-subband transitions. A QCL is a series of one dimensional quantum wells and by deliberately designing the type and thickness of each layer an electric potential is generated along the structure. This series of finite quantum wells results in a spatially-dependent probability of electrons existing at certain regions in the QCL. These are known as the electron subbands, and it is transitions between these states which produce the radiation. When an electron tunnels from one well to the next a photon is released and there is a finite probability that the same electron can tunnel again, and so on. This results in a theoretical quantum efficiency greater than one as a single electron can be responsible for a number of generated photons equal to the number of tunnels it goes through. This is called cascading.

The semiconductor-type design means that QCLs have similar advantages to laser diodes. They have a narrow linewidth [18], high power output, a good tuning range which can be selected by temperature, small in size and robust. The quantum well design has the added advantage of being able to be run at room temperature, as opposed to cryogenic temperatures required for lead-salt diode. QCLs currently operate from 2 µm to approximately 200 µm [68, 69, 70, 71], although the spectrum is not yet fully accessible.

QCLs can be combined with external cavities to enhance linewidth and tuning abilities, and are advantageous in spectroscopy because they cover the spectral region which contains the majority of fundamental transitions, which are inherently stronger than overtones.

Some of the main issues in the use of QCLs in TDLAS relate to the detection of the

radiation. The detector technology in the IR is not as developed as that in the NIR and the signals are often noisy[3] by comparison. Only recently has detector technology become available which does not require cryogenic cooling [72].

2.3.3 External cavity diode laser spectroscopy

An external cavity diode laser (ECDL) is essentially the same as a DFB laser, with the notable difference that the grating is external to the laser gain cavity, unlike a DFB laser in which the Bragg grating is incorporated into the semiconductor junction. The separate nature of the diffraction grating allows a wide tuning range to be accessed by this type of laser system. Essentially the gain medium part of the laser system can be a standard Fabry-Pérot diode laser and there are two common setups: the Littrow configuration [73] and the Littman configuration [74]. Both versions require the exit facet of the FP diode to be coated with an antireflection layer to suppress any optical feedback. It is essential to suppress any modes of the sub-cavity formed by the boundaries of the gain medium in order to ensure that the external cavity determines the mode structure of the laser output.

The Littrow configuration, seen in figure 2.2a, shows the output light of the FP diode being coupled onto the diffraction grating via collimation optics. The first order diffracted beam from the grating is fed back into the FP diode causing amplification of the selected wavelength. This occurs when the angle of incidence θ_i is equal to the diffraction angle ϕ_1. The grating equation then reduces to

$$\lambda_i = 2d \sin \theta_i, \tag{2.3}$$

where the groove spacing is given by d. The angular dispersion $D_{Littrow}$ of the reflected beam is identical to the diffracted beam, so we have

$$D_{Littrow} = \frac{\mathrm{d}\phi_1}{\mathrm{d}\lambda} = \frac{2 \tan \theta}{\lambda}. \tag{2.4}$$

[3]Background thermal radiation is a constant problem for IR detection and being able to filter this out of the signal, especially in a dynamic and hot environment such as a furnace is challenging.

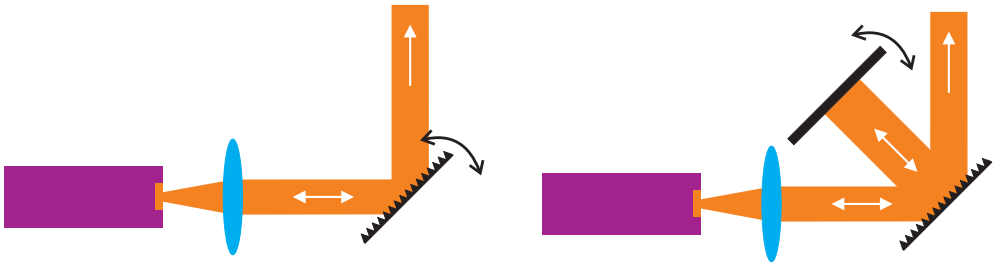

(a) Littrow configuration (b) Littman configuration

Figure 2.2: Figure a) shows the Littrow, and b) shows the Littman setup of external cavity laser diodes. Both configurations start with a Fabry-Pérot diode emitting radiation onto a diffraction grating, often through collimation optics due to the large divergence of the diode facet. By feeding back a narrow frequency band back into the diode facet, the laser emission spectrum will collapse down onto a single mode - the negative or positive first order from the diffraction grating is often chosen.
In the Littrow case (a), the diffraction grating is rotated to tune the laser output, and this has the unwanted side effect of also moving the laser propagation direction. The Littman setup (b) has an extra mirror which reflects the diffracted order back onto the grating and back into the diode. In this example the grating is static and instead the mirror angle is adjusted. This allows the exit angle of the laser beam to be fixed, thus improving on the Littman setup.

This angular dispersion gives an indication of the maximum value the linewidth of the emitted beam can take. It is a maximum value because gain narrowing from multiple passes through the diffraction system and amplification which favours the more intense spectral lines has been neglected. One disadvantage of this setup is that the zero-order reflection from the grating, which is the output beam, moves as the grating is tuned.

Figure 2.2b shows the Littman configuration which differs from the Littrow setup by the presence of a reflecting mirror. The main operational change is that the grating in this system is static and the mirror is rotated instead. This gives the added advantage of having an output beam in a constant direction independent of mirror angle and thus frequency selection. This is a more practical implementation of an ECDL. As each round trip of the laser cavity experiences frequency-dependent diffraction twice, the angular dispersion is double the value of the Littrow setup.

$$D_{Littman} = 2D_{Littrow} \tag{2.5}$$

This extra diffraction results in a narrower beam linewidth but less power as the zero-order reflection is lost in this instance.

2.3.4 Raman spectroscopy

When light propagates through a medium there are many possible scattering effects that can occur which depend on the particular circumstances and conditions of the medium. Rayleigh, Raman, and Brillouin scattering occur when the light interacts elastically, inelastically, and with phonons respectively. The technique most relevant to combustion analysis is Raman spectroscopy. Raman spectroscopy can occur spontaneously, however it is unsuitable for probing the highly luminous particle-laden flames typical of many practical combustion media. Coherent anti-Stokes Raman spectroscopy (CARS) is a widely used technique that overcomes these issues seen with spontaneous Raman spectroscopy, however it works only with majority species of those present at relatively high concentrations 1 - 10%.

CARS

Coherent anti-Stokes Raman spectroscopy is the generation of a coherent signal at frequency ω_3 through the 3^{rd} order term of the nonlinear susceptibility of the probed media. Two pump laser beams of frequency ω_{pump} and the Stokes beam of frequency ω_{St} overlap in parallel and by phase matching the three beams as shown in figure 2.3a, the CARS signal is generated in such a manner as to conserve momentum. $\vec{k_i}$ is wave vector at frequency ω_i and has a magnitude given by the following relation

$$\vec{k_i} = \frac{\omega_i n_i}{c}, \tag{2.6}$$

where n_i is the refractive index of the host material at frequency ω_i.

The pump laser is often pulsed and single mode, and a frequency doubled Nd:YAG laser operating at 532 nm is a common choice. The Stokes beam can either be narrow-line single mode operation or a broadband laser resulting in the narrow band scanning approach or the

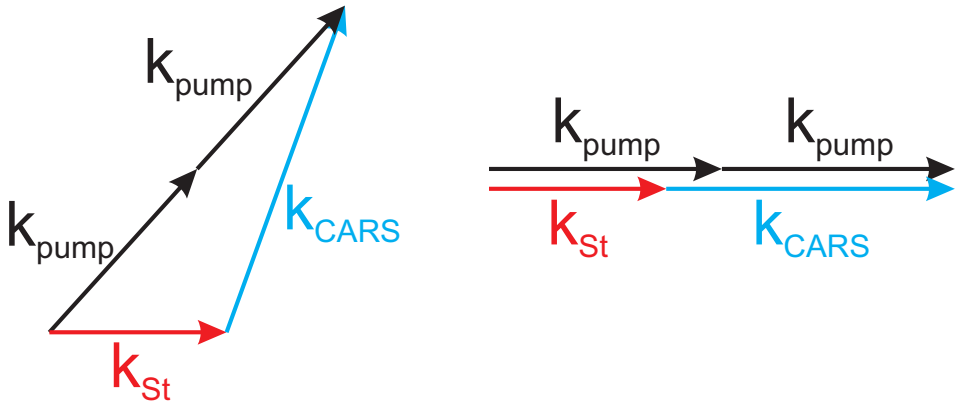

(a) The CARS radiation ω_{CARS} must satisfy momentum and energy conservation. The $\vec{k}_{CARS}$ (blue) of the ω_{CARS} radiation must be phased matched with the two incoming pump beams $\vec{k}_{pump}$ (black) and the Stokes beam $\vec{k}_{St}$ (red). The left-most figure shows a generic example of phase matching and the right-most example shows a co-linear setup.

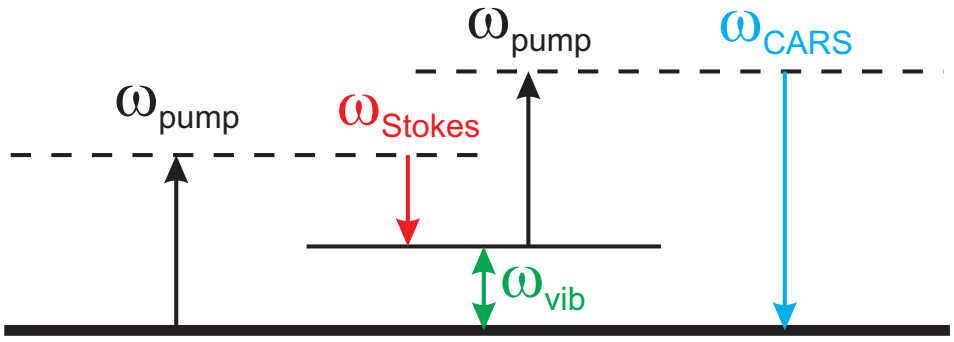

(b) The energy levels used during coherent anti-Stokes Raman spectroscopy are shown. The pump light (black) and the Stokes beam (red) undergo a nonlinear interaction with the lower vibrational state to induce a transition ω_{vib} via a virtual state (dashed line). A similar process happens again from the upper vibrational state to the ground state, again via a virtual state, only this time a signal of frequency ω_{CARS} (blue) is emitted in a particular direction.

Figure 2.3: Energy and momentum conservation of CARS.

broadband multiplex method respectively. The CARS signal can give information regarding the temperature, species concentration, temporal information and in some cases, spatial information.

High time resolution is easily achieved with this technique as it's predominantly determined by the pump laser pulse length. The temperature measurement is largely unhindered by the presence of soot or aerosols as it's the spectral shape of the signal which gives this information not the intensity; however radiation emitted from soot can distort the spectral shape in some cases. The CARS signal is heavily affected by the sample gas pressure. At very high pressures collisional narrowing effects can become prominent, however the bandwidth remains largely unchanged and in fact can be advantageous as the lines become substantially overlapped producing a single peaked strong feature, although this overlapping presents a difficult theoretical challenge to the analysis. There is no power threshold limit as such, however the CARS signal depends upon the square of the intensity of the pump laser I_P, so signal-to-noise ratio improvements are often tackled by having I_P as large a possible which can be readily done. The only limitation here is that optical breakdown by ionisation of the gases should not occur. Information on the species concentration can be calculated in this instance, however this is dependent upon soot and other factors as it is derived by referencing the resonant to the non-resonant signal.

One of the main issues with CARS is that it is a double-ended technique requiring line-of-sight optical access, and as depicted in figure 2.3a, the CARS beam is forward-generated so there can be difficulties in filtering out the pump and Stokes beams. It is extremely difficult to implement on more than one species at a time and the laser frequencies ω_{Pump} and ω_{St} are carefully chosen for a particular case. Femtosecond CARS allows multiple species detection as the large bandwidth of the laser can encompass Raman resonances in several species but such lasers are often very expensive to purchase. The modelling is computationally intense, especially at high pressures. The spectra can also suffer from interference effects due to the modulus squaring of the 3rd order nonlinear CARS susceptibility.

CARS has been combined with TDLAS to allow accurate determination of species concen-

tration and temperature determination. Dependent on temperature, a minimum detectable amount of 200 ppm to 2500 ppm was achieved on CO detection (NES $= 2.7 \times 10^{-7}$ cm^{-1} Hz$^{-0.5}$ or 54.6 ppm m Hz$^{-0.5}$). CARS allowed a 65 µm spatial resolution to be found which is a very powerful tool for combustion analysis [75]. The time resolution for the TDLAS was 3.2 s

With parallel beam propagation, no spatial information can be inferred as the coherent beam is generated from all point among the interaction volume. Three wave mixing can also be a hinderance, so to eliminate this and to increase the spatial information, a different setup can be used, known as BOXCARS. The lasers are crossed in a 3-D arrangement of the pump and Stokes beams which can lead to spatial information being determined.

2.3.5 Broadband absorption spectroscopy

Broadband absorption spectroscopy (BAS) is a cheap and simple technique to monitor a very large spectral range so multiple species can be detected simultaneously. In a manner some what similar to TDLAS, light from a single source is passed through a gas and the transmitted power is monitored using a spectrometer. The broadband light source is typically an incoherent light source such as a lamp or emission tube, low coherence superluminescent diode (SLED), or a light emitting diode (LED).

The advantage of using a lamp is often the ease of operation, the wide variety of different bulbs, as well as long-term stable operation and large amount of working hours before a service or bulb change is required. A thermal bulb will have a power spectrum based on its operating temperature via Stefan's law, however an emission tube will emit at several discrete lines which normally have to be broadened by increasing the pressure of the lamp. A filter is sometimes employed to narrow the spectral output of the broadband source.

A SLED is similar to a regular laser diode in that a pn junction has a current driven through it and the recombination of holes and electrons causes stimulated emission of light. However, there is insufficient feedback from the facets of the junction to achieve lasing which prevents the broad spectrum collapsing into longitudinal modes. SLEDs have a very high

single pass amplification generated along the waveguide. This leads to them having a low level of coherence which can be utilized for high resolution spatial imaging purposes [76]. Sub parts per million sensitivities were detected on 1,3-butadiene with this scheme, but it did incorporate a path enhancement of 5000 on a cell of 25 cm in length.

Gao et al [77] have developed a LED that operates between 3.8 µm and 5.0 µm, with a peak power output at 4.5 µm. It was been suggested that this device could be used as a potential monitor for simultaneous detection of CO and CO_2 in various applications. By utilising the fundamental transitions in this spectral region, good sensitivity could potentially be achieved.

Super-continua sources created by nonlinear processes upon intense pumping of optical materials has also been demonstrated [78].

Simultaneous detection of nitrous acid and nitrogen dioxide has been demonstrated using incoherent broadband cavity enhanced absorption spectroscopy. Using a 366 nm UV LED, a spectral resolution of 0.77 nm was achieved and this led to a minimum detectable amount of 430 ppt for NHONO and 1 ppb for NO_2 over 90 s acquisition time (NES = $7.5 \times 10^{-8}\,\mathrm{cm^{-1}\,Hz^{-0.5}}$). Both species were simultaneously detected in the open air with an effective cavity length of 2.8 km. Aerosol scatter was a substantial problem with this setup because of the UV light being used [79].

A main disadvantage of BAS comes from extracting the information from the light source once it is passed through the sample gas. The transmitted light has to be separated into its spectral components, often through the use of a spectrometer [80]. This often places a spectral resolution limit of order of several GHz on the result, so high resolution spectroscopy is not possible with this technique. Yet $0.14\,\mathrm{ppm\,m\,Hz^{-0.5}}$ detection of SO_2 was achieved using a deuterium lamp. As the SO_2 was at atmospheric pressure high resolution spectroscopy is not possible anyway. To improve the resolution a larger spectrometer can be utilized but this can be cumbersome and expensive.

BAS is advantageous in high pressure/temperature environments where the substantial

broadening terms dominate the resolution, however the low spectral power density means it can struggle to penetrate optically thick gases or those with a high aerosol content.

2.3.6 Differential absorption light detection and ranging

Differential absorption LIDAR (DIAL) is a specialized spectroscopy technique that has the unique ability to monitor a single species over a huge spatial volume, hence its main application of environmental monitoring especially water vapour measurements in the troposphere [42]. LIDAR works in a similar manner to RADAR with the obvious difference that it utilizes much shorter wavelengths in the visible or near infrared. The detection of backscattered radiation is used to determine the distance of an object or phase transition. The conversion of LIDAR over to DIAL requires an additional laser system. Both lasers are often short-pulsed and single mode in operation. An example of water detection uses 150 mJ in a pulse width of 30 ns from a Ti:sapphire laser. One is tuned to be resonant with an absorption feature of the species of interest and the other will be tuned off-resonance in a spectral window so no direct absorption takes place [81]. The backscattered light from both sources is detected and analysed. The backscatter from the off-resonance beam mirrors the optical path of the resonant beam but as it does not interact with the target species it allows the removal of any losses caused by atmospheric disturbances, aerosol scatter and other noise sources [19].

To utilize the superb spatial coverage on offer from a DIAL system it is often necessary to place it in a satellite or on an aircraft. This allows large portions of the atmosphere to mapped in a single session and gives access to the different layers. The LASE (LIDAR atmospheric sensing experiment) is flown aboard a NASA/Ames ER-2 aircraft and can record continuous data for 8.5 hours of flight time [42]. LIDAR also has applications in ground-based measurements where it can be used to monitor emissions from a chimney and see how they disperse over the local area [82]. Typical distances covered by DIAL detection schemes range from 30 m [17] to 21 km [82]. Hardy et al was able to have a minimum detectable amount of 150 ppb (NES = 581 ppmHz$^{-0.5}$) using a 4.2 µm QCL with a measurement error

of 3.6% on carbon dioxide with a portable device.

A DIAL system is therefore generally not suited to confined measurements or applications which require a cheap system. The laser systems are expensive and for such large power outputs a substantial amount of cooling is required which adds weight and cost. Access to large voltage power supplies is also necessary and all of these requirements will severely reduce its portability. Moreover, DIAL is only sensitive to one species at a time and each species requires two separate laser beams.

2.3.7 Correlation spectroscopy (COSPEC)

Correlation spectroscopy can have several variants most of which revolve around the light source being used. This technique relies upon direct absorption, similar to TDLAS, but the basic setup employs a reference gas cell alongside the cell of unknown gas. By comparing the absorbed signal from both gas cells the composition of the unknown gas can be determined. Although a single mode laser can be used in this way COSPEC strongly demonstrates its advantages using a multimode laser.

Often a multimode laser will be employed as this will have a large spectral coverage so multiple species can be detected simultaneously. The performance of the multimode laser will be highly dependent on the anti-reflection coating on the exit facet as feedback from this surface into the laser can cause the mode structure to collapse into a single mode. Feedback into a multimode laser could cause mode instability, however some feedback is necessary to reduce the number of modes being produced [83]. Unfortunately, there will always be some feedback from the exit facet and this will cause some instability within the laser modes. This is typically manifested as random fluctuations in laser mode intensity, potential mode-hopping, and mode competition. COSPEC offers to bypass these issues by temporal correlation of two detected signals. One signal contains the absorption from the unknown gas and the other contains only absorptions from a known reference cell. Both signals however contain any laser fluctuations which will be correlated on both detectors. Any differences are then attributed to the absorption independent of the fluctuations. COSPEC

does not necessarily require a laser as a light source - any fluctuating light source will suffice provided the it has the necessary spectral width to cover the absorptions of interest.

The light from the laser source is split into two parts where one is sent through the reference cell and the other through the unknown gas cell. Any behaviour relating to mode intensity variation, mode hop, or other laser noise is instantly removed by this simultaneous detection of the transmitted light from both gas cells. By comparison of the two signals the concentration of the unknown cell can be determined. Often the ratio of the two signals is used. By being able to target a wide spectral region many absorption features can be detected in one measurement which allows this technique to be extended to multiple species by the inclusion of each target gas species in the reference cell.

Acetylene has been detected with a minimum detection limit of 3 ppm in 48.5 cm (NES = 0.3 ppm m $Hz^{-0.5}$) optical path length [84]. COSPEC has also be demonstrated on oxygen at 760 nm in one instance with the use of porous gas-filled materials for path length enhancement [85, 86]. These porous materials are several centimetres in length but can offer over a meter of optical path. A minimum detection of of 15 ppm m (NES = 3 ppmm $Hz^{-0.5}$) has been demonstrated with this system on atmospheric oxygen, and the compactness of the absorption cell is very advantageous for any portable device. The very small amount of transmitted signal is an issue with this particular path enhancement.

One further advantage of COSPEC is that a detailed knowledge of the theoretical spectrum is not required, so the computational power required is very low as an oscilloscope with a differential amplifier is sufficient to determine the concentration of the sample cell. One major disadvantage of COSPEC is the intrinsic requirement that the reference cell be at the same temperature and pressure as the sample cell as any temperature/pressure fluctuation would manifest itself as a signal [87]. This issue severely limits the industrial applications of this technique as most processes operate in a dynamic environment.

Nadezhdinsky et al [87] however, demonstrated the use of COSPEC in an environmental monitoring application by placing the system onboard an aircraft equipped with a laboratory. By drawing in samples of outside air, different heights were analysed in real time for CH_4,

CO_2 and H_2O concentration. By combining the three laser beams, the three target species of water, carbon dioxide and methane were detected at 1392 nm, 1602 nm and 1650 nm respectively. Over a 30 ms measurement time minimum detectable amounts of 30 ppm, 4 ppm, and 25 ppb were obtained. The sampled air was warmed to the reference temperature and reduced in pressure to 100 mbar. This setup was also able to monitor the different isotopes of oxygen ^{16}O and ^{17}O.

2.4 Enhancement techniques

Some spectroscopy techniques have been discussed, each having their own advantages and disadvantages. These benefits or hindrances can be further amplified or reduced respectively by the addition of other technology and techniques. Often, a particular enhancement is only suited to some applications and considerations have to be made as to the limiting factor of the current system, (signal size or noise for example) and how that can be improved upon.

2.4.1 Cavity enhancement techniques

By injecting the laser radiation into an optical cavity a signal enhancement can be achieved which improves the sensitivity of the system by increasing the effective path length the laser light transverses. There are several methods by which this cavity can be utilized. All optical cavities have cavity modes which must be matched by any radiation that is coupled in to it. By taking advantage of this condition more robust and improved sensitivity spectroscopic techniques have been developed over the last 10 years or so.

Cavity ring-down spectroscopy

Cavity ring-down spectroscopy (CRDS) monitors the decay of light from a cavity after the light has ceased being injected into the cavity. Initially, this technique was done using a pulsed dye laser system [88] whereby the laser radiation was coupled into an optical cavity

containing a trace gas which had a resonance with the laser light. By monitoring the decay time of the light in the cavity the amount of absorber can be determined. For a cavity of length L, with mirror reflectivity R, the natural decay coefficient τ_0 is given by

$$\tau_0 = \frac{L}{c\,(1-R)}. \tag{2.7}$$

This is the time decay constant for radiation contained in the optical cavity with no absorber present. Assuming that the absorber gas occupies the whole length L then the time constant is modified to

$$\tau = \frac{L}{c\left((1-R)+\sigma C L\right)}, \tag{2.8}$$

where σ is the absorption cross-section and C is the absorber concentration [44]. This leads to a reciprocal relationship of

$$\frac{1}{\tau} = \frac{1}{\tau_0} + c\sigma C. \tag{2.9}$$

Through equation 2.9, the concentration of the absorber can be determined so long as the decay time of an empty cell, τ_0, has been previously determined.

A disadvantage of using a pulsed laser system is that it can often operate on multiple modes and has a broad line width. By coupling multiple frequencies into the cavity, multiple exponential decays can occur in the ring-down measurement which is hard to analyse. This problem can be solved by using a continuous-wave (cw) laser and utilizing a fast optical switch for rapid ring-down measurements, where the switching is fast relative to the round-trip time in the cavity [89]. CW-CRDS has increased sensitivity in comparison to pulsed operation and the superior linewidth provides an improved spectral resolution.

A CRDS signal is independent of laser intensity fluctuations and calibration is not required if the line strengths of the absorber are known. This means that this technique can be potentially suitable for hostile environments and it has been used in environmental monitoring [5].

CRDS has been used in a setup which resulted in a SNR of 28000 [28]. It has also been demonstrated for use in the UV (407 nm) for NO_2 detection [46]. This resulted in less than

1 ppb detection sensitivity, however the broadband amplified spontaneous emission from the diode laser meant that high resolution spectroscopy was not possible. CRDS has also been applied to directly measure the NO_2 emissions from a diesel engine [44]. By using a 6.13 µm pulsed QCL sub parts per million detectable limit were demonstrated after the exhaust gases were filtered and dried.

An effective path length of 2.1 km was demonstrated for real-time detection of NO at 5.26 µm which resulted in a sensitivity of 50 ppb over a 20 s measurement [43]. The exhaust gas was filtered and dried before being passed into the cavity which measured 50 cm in length. This work demonstrated the ability of the laser based system to monitor NO from exhaust gas over a dynamic range of three orders of magnitude.

Utilising the intrinsic advantages of CRDS in hostile environments this technique has also been applied to monitor OH radicals in flames. The flame is situated within the cavity and probed using a laser. In the study by Schocker and colleagues [90], a single-mode laser which is tuneable over the range of 632 nm to 639 nm is amplified using a modeless laser at a rate of 10 Hz. The laser linewidth was 200 MHz which was limited by the pulse duration of the amplifier acting on a >5 MHz diode laser beam by the Fourier transform limit. This allows high resolution spectroscopy to be taken of the OH radical in the flame and an accurate Voigt line profile to be fitted to the data. The Gaussian component of the Voigt profile yields the flame temperature as Doppler broadening is the only contribution to the Gaussian component. A temperature of 1440 K with an error of 60 K was derived [90]. The narrow, single mode laser used in this work had a linewidth much smaller than the absorption linewidth. Thus the absorption coefficient for the laser light had a single exponential ring-down time. If a broad linewidth or multimode laser is used, different parts of the laser spectrum experience different ring-down times resulting in a signal that is multi-exponential decay which is much harder to interpret quantitatively.

Cavity enhanced absorption spectroscopy

Cavity enhanced absorption spectroscopy (CEAS) continuously couples laser light into the cavity, which, similar to CRDS, uses very high reflective mirrors ($> 99\%$). The laser frequencies must match the cavity modes for efficient transfer of light into the cavity. Continuous cavity transmission is required for this technique to work, so the cavity resonance modes are adjusted along with the laser frequency to make sure that efficient coupling occurs throughout the scan. A typical method of adjusting the cavity modes is to vary the cavity length by using a piezo-electric transducer (PZT) [91] operating at a frequency much higher than the laser scan frequency. This causes the intensity fluctuations from the different cavity modes to be averaged out provided that the measurement time is sufficiently long. A typical setup is shown in figure 2.4.

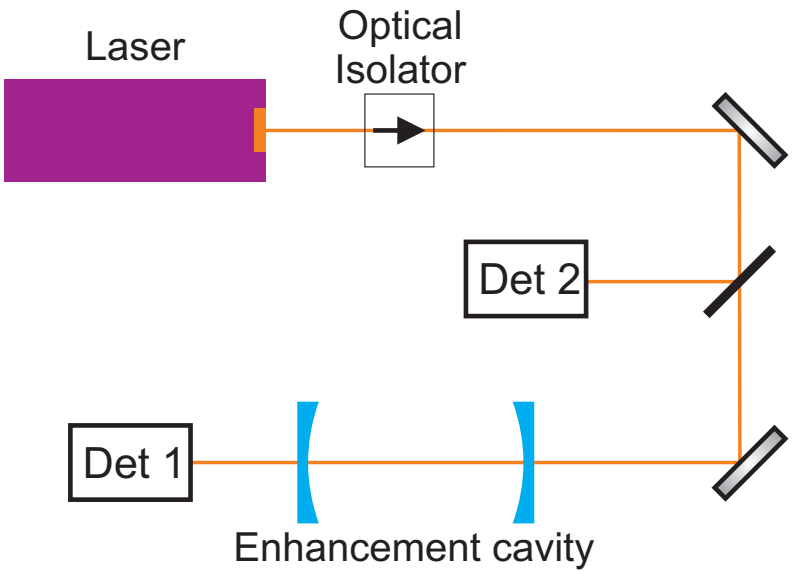

Figure 2.4: The laser light source is passed through an optical isolator so as to prevent feedback from the back surface of the cavity affecting the laser output. Part of the beam is (possibly) split off as a reference at detector 2 (Det 2), and the remaining power is coupled into the enhancement cavity which contains the gases to be measured. The effective path length is dependent upon the reflectivity coatings of both mirrors. The transmitted power is detected on detector Det 1, which would normally be an avalanche or photomultiplier tube [91] due to the extremely small signal allowed through the mirrors.

CEAS can be used with broadband sources for incoherent spectroscopy [48, 79]. This is an effective way of detecting multiple species in conditions where high resolution spectroscopy

is not needed such as complex organic molecules or atmospheric gas monitoring. Breath analysis is another such situation [76].

One drawback of CEAS is the lack of power which is transmitted through the cavity. Even though path length increases of up to several kilometres are achievable with this technique, if the original laser only produces milliwatts of power, then only picowatts of power will be transmitted [91].

The reduction in transmitted laser light intensity ΔI caused by the molecular absorptions equates to what would be obtained if in fact no cavity were present. The enhancement therefore comes not from an increase in ΔI but by a sharp decrease in I, whereby the enhancement factor is given by $\frac{\Delta I}{I}$. The increase in contrast is solely attributed by the attenuation of transmitted background light I and the reduction of any measurement noise associated with it [92].

Off-axis integrated cavity output spectroscopy

Off-axis ICOS is an upgrade from CEAS. Its main difference is the injection angle of the incident laser beam, which is a few degrees off axis [93]. By off-axis injection, the single cell becomes a multipass cell of m passes. The FSR is therefore given by

$$FSR = \frac{c}{2mL}. \tag{2.10}$$

A very dense mode spectrum is achieved leading to averaging of the absorption over all the cavity modes. An example of an ICOS cavity setup is shown in figure 2.5. When the effective FSR of the gas cell becomes less than the linewidth of the laser there will be a certain amount of radiation coupled into the cavity which is non-resonant. By having a spacing between cavity resonances which is smaller than the linewidth of each mode the effective transmission is heavily smoothed and the discontinuous output spectrum of CEAS is removed [94]. The laser light contained within the cavity can now be described by simple rate equations which

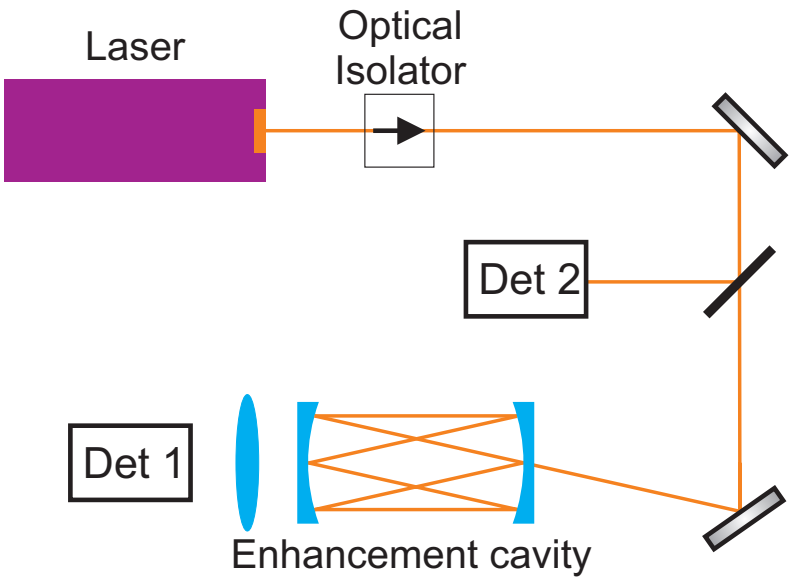

Figure 2.5: The basic ICOS setup is similar to that of CEAS shown in figure 2.4. The principle difference here is that the incident angle of the radiation into the cavity is chosen such that multiple passes of the cell are made before the beam starts back on itself. In this example, 3 round trips are possible before arriving back at the start, resulting in a free spectral range three times smaller than a regular CEAS setup with the same cavity length.

for a simple cw laser are given by

$$\frac{\mathrm{d}I}{\mathrm{d}t} = \frac{c}{2L}\left[I_0CT - 2I\left(1 - R - A\right)\right], \tag{2.11}$$

where L is the cavity length, A is the per-pass absorption, R is the mirror reflectivity, and I_0CT is the average cavity injection intensity. (C is the coupling parameter and T is the mirror transmission) The steady state solution to equation 2.11, multiplied by T is given by

$$I_t = \frac{I_0CT}{2\left(1 - R + A\right)}T \tag{2.12}$$

which can be used to calculate the fractional absorbance from a Beer-Lambert-like relationship [94].

In this regime, ICOS is intrinsically insensitive to small vibrations and misalignments. It also allows multiple modes to be injected into the cavity simultaneously. The main source of noise is the random nature of the laser power injection into cavity. Finite spot size is also a

problem as the laser beam can overlap and cause etalon effects before the re-entry condition is met. Beam overlapping can be avoided by careful selection of mirror curvature, however this will reduce the number of cell passes before the laser beam starts to retrace its own path.

The ICOS technique is suitable for field measurements due to its insensitivity to external vibrations, high sensitivity, and relative compactness which depends upon the type of gas cell used [93]. For example, a ring cell could be used which will occupy less length than a straight retro-reflecting cell. Dependent upon the particular radiation used and species detected, ICOS can increase the SNR by up to 14 if combined with wavelength modulation spectroscopy at low scanning frequencies [94]. If the scanning frequency is increased the SNR for WMS-ICOS decreases, whereas for ICOS alone the SNR kept on improving. This shows the need to balance detection limit against measurement time as one will often degrade as the other improves.

Comparative studies have shown CEAS to be inherently less sensitive than CRDS primarily due to the nature of the measurement because the cavity output intensity is subject to laser intensity fluctuations [49, 95].

2.4.2 Optical feedback enhancement

Optical feedback enhancement is a technique that is usually combined with cavity enhancement and utilizes the reflection of laser light which is then fed back into the laser source cavity. The basic idea behind optical feedback enhancement is to start by injecting a resonant frequency into a high finesse cavity. By suitable alignment of the cavity mirrors only the fundamental TEM_{00} mode will exist. This radiation will leak out of the cavity and if this light is fed back into the laser source, it will seed the laser and lock the output frequency to that of the cavity mode as well as narrowing the laser linewidth. In practice, the execution of such an effect requires some thought because only the TEM_{00} mode must be fed back into the laser and the phase and amount of feedback are critical to the correct operation of OF enhancement when applied to a spectroscopic technique.

Firstly, the shape of the cavity to be injected into is important. If a linear cavity is used, then the back reflection from the input mirror will provide unwanted feedback of potentially other TEM modes. To get around this the laser path can be spatially filtered by focusing the light through an iris. This process will reject the laser light that is reflected from the mirror face but accept the laser light transmitted from the TEM_{00} mode from the cavity. A schematic of this setup can be seen in figure 2.6 [96].

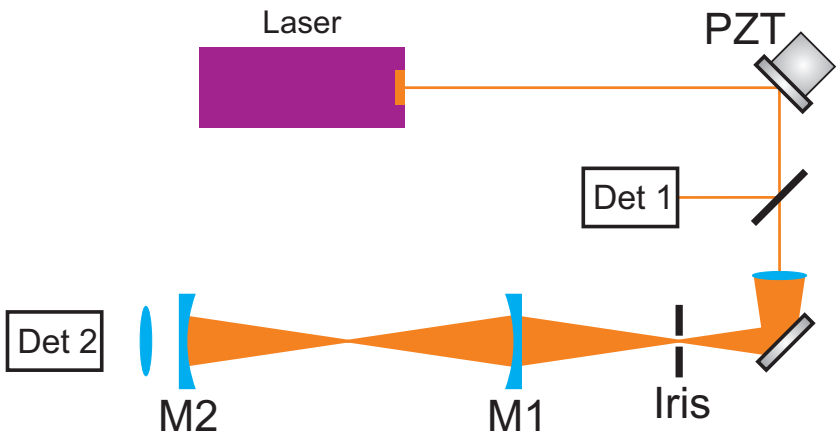

Figure 2.6: Experimental setup of optical feedback utilising a linear cavity. The iris spatially rejects any unwanted feedback from mirror (M1) that does not match the mode profile. Only radiation from the TEM_{00} mode built up inside the cavity is returned to the laser, and the amount is controlled by the iris diameter. The PZT controls the phase of the feedback which is crucial for optimising the detected signal.

Other cavity configurations can be used which remove the need for spatially filtering the light. A V-cavity [97] or a ring-cavity [89] achieve the same selective feedback but by design reject unwanted reflections. The V-cavity design is shown in figure 2.7 for comparison. A description is available in the literature [89].

One other benefit of optical feedback is laser linewidth narrowing. By feeding the TEM_{00} mode back into the laser system the laser linewidth can be reduced in size to be far less than the original laser linewidth. This is because the radiation leaking from the cavity has a very low frequency dispersion given by the cavity mode width. The saturated gain medium of the laser - especially diode lasers - is then seeded by the narrow cavity radiation which results in gain narrowing and the laser field is driven in a highly monochromatic fashion. This

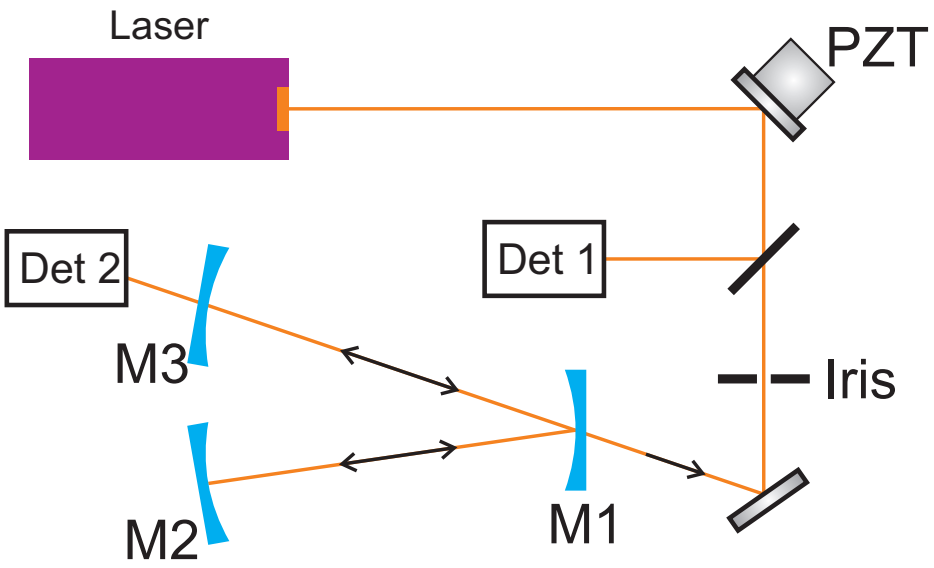

Figure 2.7: Experimental setup of optical feedback utilising a V-cavity. The reflection from the input mirror (M1) is automatically rejected. This allows the TEM_{00} mode to be fed into the cavity without undesired feedback returning to the laser. The V-cavity is formed between mirrors M2 and M3, with M1 being the base of the V. Light exiting from M3 is collected and used for spectroscopy. Light reflected from M3 and then transmitted by M1 only is allowed back along the original beam path with the returning amount being controlled by the iris. Reflections from M2 are lost as are transmissions. The PZT controls the phase of the feedback relative to the laser source, which must be varied as the laser frequency is altered due to the new cavity conditions that need to be met.

resulting field is then coupled back into the cavity where the process happens repeatedly. The outcome is a smooth and noiseless signal observed at the cavity output [98]. This same process is responsible for the frequency locking of the laser source which has uses in other optical fields.

During laser spectroscopy, in the case of optical feedback cavity enhanced absorption spectroscopy (OFCEAS), each time the laser frequency becomes resonant with a cavity mode, the transmitted power will increase sharply and the spacing of these transmission peaks will be exactly one free spectral range of the cavity [98]. By tracking the peak height of these transmissions spectra of any absorbing species can be inferred and a simulated example is shown in figure 2.8.

The phase of the returning light relative to the laser source is a crucial parameter and is dependent upon the distance between the laser and the input mirror of the cavity L_0. Ideally

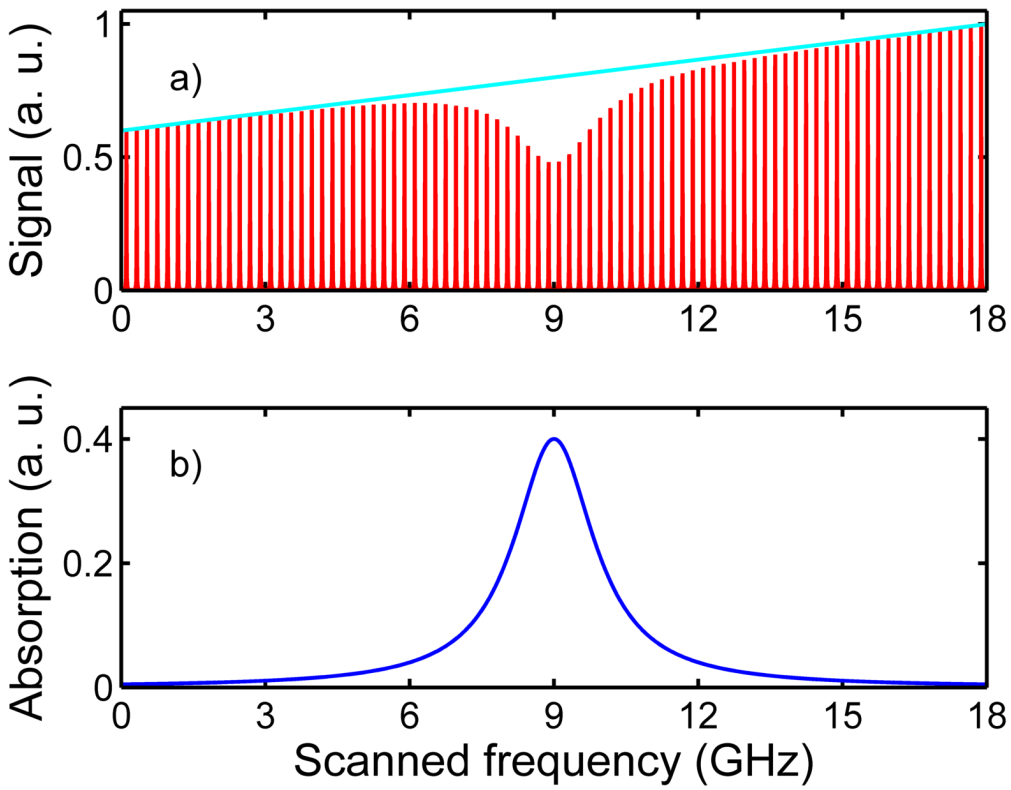

Figure 2.8: Figure a) shows the signal transmitted through the cavity when an absorber is present (red), and the background signal (cyan) if the cavity does not contain an absorber. The red transmission lines are equally spaced as they are the longitudinal cavity modes of the cavity. As the incident laser is tuned (in this example 18 GHz), every time the absolute frequency becomes resonant with the cavity free spectral range, the transmitted signal spikes. The 'bump' on the red signal can be inferred by dividing away the cyan background line, which results in the absorption signal, given in figure b). The resolution of the system is given by the FSR of the cavity, typically a few hundred mega Hertz.

this should be a multiple of the cavity length (unfolded in the case of a V-cavity). For a single mode resonance this can be easily achieved, however, during spectroscopy the laser frequency will be tuned and as the wavelength is altered, thus the phase will change and could result in non-optimal transmission of light. Strictly speaking the phase must change with the frequency and this can be done using the PZT in figure 2.7. However, the position tolerance depends upon the number of cavity modes that are being excited. The optical feedback phase my be sufficiently uniform across a suitable number of cavity free spectral ranges, so in this case, L_0 can be kept constant provided the tuning range is suitable for the absorbing species.

Optical feedback enhancement allows for high resolution gas spectroscopy to be performed

at atmospheric pressures with the resolution being limited by the free spectral range of the cavity. The cavity enhancement provides the same benefits as mentioned above, so the coupled radiation inside the cavity has an effective path length of several kilometres.

One drawback of OF enhancement is that it must be scanned at a slow rate, one example being 2 Hz [97]. This is necessary to allow sufficient time for the optical feedback to occur and produce a stable mode intensity inside the cavity.

2.4.3 Noise reduction techniques

The methods described above generally discuss how the signal size can be improved with the use of cavity and path length enhancements. This subsection examines methods of noise reduction as an alternative way of improving the signal-to-noise ratio.

Balanced detection

One easy and commonly used method of noise reduction is to use balanced detection. As depicted in figure 2.1, two detectors are used to measure the laser light intensity where one is measuring a reference arm and the other the gas sampling arm. By a simple division of detector signals, any modulation common to both signals will be removed and the resultant signal will be dependent upon the relative intensity values of the two detectors. This can also be known as balanced ratiometric detection (BRD) and the sensitivity is highest when the two signal intensities are equal. BRD devices are often slow and the bandwidth is ultimately limited by the scan rate of the laser [99].

Unlike simple division mentioned above, auto-gain digital balancing detection adjusts the gain applied to the reference arm by means of a negative feedback control loop which, ideally, results in the perfect subtraction of the two channels. The controller electronics monitors the difference between the two channels and alters the gain on the reference arm accordingly. In principle, the degree of balance is limited by electronic noise effects, not optical effects [99]. In work done by Pal et al, a precision of 1×10^{-4} at kHz bandwidth, which

gives an NES of $3.6 \times 10^{-6}\,\mathrm{Hz}^{-0.5}$ was reported. The NES was larger than the equivalent for BRD or wavelength modulation spectroscopy. Other advanced detection methods are available whereby all-electronic noise cancellation circuits that largely eliminate excess laser intensity noise [100]. They generally operate by applying feedback outside the signal path to adjust the ratio of two photocurrents with a bipolar transistor differential pair, so that when the two are subtracted, the dc component of the result is zero [100]. Noise reduction techniques such as this, however, do not remove etalon interferences and any phase noise between the two channels.

Wavelength modulation spectroscopy

Wavelength modulation spectroscopy is a common enhancement technique normally used in conjunction with TDLAS [33, 45, 66, 101]. Whereas some of the techniques mentioned earlier improve the amount of absorption, WMS reduces the level of noise observed in the signal. WMS has been shown to improve the signal-to-noise ratio of MUMAS using a laser diode light source [91]. Dependent upon which harmonic was detected, WMS alone gave a SNR improvement of 2 or 3 for $1f$ and $2f$ respectively[4]. WMS is advantageous when the background noise is at a frequency far away from the applied modulation frequency f.

One of the main disadvantages of WMS is that it is a non-absolute method, i.e., the WMS spectra need to be calibrated against known gas species. This can either be done by using test gases of known concentration or by using another technique, such as TDLAS, in parallel to calibrate the signal. This calibration is not always possible - especially if the species to be detected is found in trace amounts. However, self-calibrating methods have been discussed and implemented, most notably the phasor decomposition method [2].

[4] $1f$ represents first harmonic demodulation of the signal; $2f$ represents second harmonic demodulation.

2.5 Introduction to MUMAS

A relatively new spectroscopic approach first reported in 2008 by Arita et al [14] offers a novel approach that can achieve simultaneous detection of multiple gas species or multiple transition lines. The technique, known as multimode absorption spectroscopy (MUMAS) has a wide spectral coverage, high resolution and it only utilizes a single laser and single detector. MUMAS uses a comb of longitudinal modes of a short cavity, multimode, laser which are simultaneously scanned over the mode spacing [12]. By simultaneously scanning the laser modes the required data capture rate for a given spectral coverage is n times less than what would be required for a single mode source to scan over the same region in a single sweep, where n is the number of laser modes in the multimode source. MUMAS provides a viable alternative to multiplexing methods involving multiple lasers and unlike gas correlation absorption spectroscopy does not require a reference cell. The MUMAS setup is often inexpensive to purchase and run when compared to complex femtosecond laser systems. The power signature which is read out from the single detector used in MUMAS will be unique to the characteristics of the laser being used and the gas species conditions. Therefore if the laser is fully characterized, then this signature will be unique to the particular gas mixture being detected and is called the *MUMAS fingerprint*. By fitting a simulated MUMAS signature to this fingerprint the concentration of the target gas species, temperature and pressure of the total gas can all be inferred.

Multimode absorption spectroscopy has been demonstrated as a viable laser spectroscopy technique and it has distinct advantages over alternative systems. A proof-of-principle was performed using a multimode diode laser on atmospheric oxygen at 760 nm [14]. Furthermore, temperature and pressure measurements were later performed again on atmospheric oxygen to demonstrate that MUMAS could be utilized in barometry and thermometry. An experimental uncertainty of 2% was demonstrated in both cases for oxygen between 0.2 bar to 1 bar and 300 K to 500 K [12]. MUMAS has the advantage of measuring multiple lines of the same species and these absorptions can be used to calculate the temperature of the gas by the comparison of line strengths. This ability is based on the large spectral

coverage MUMAS has to offer, typically 200 GHz.

MUMAS was then demonstrated in the near infrared region by recording spectra of acetylene around 1.53 µm using a multi-mode Er:Yb glass microlaser [13]. However, the mode linewidth of this system was particularly wide only giving a resolution of 0.7 GHz due to the low Q of the cavity used. Whilst not a huge problem at atmospheric pressures it would be a hinderance for low pressure, high resolution applications. This laser design was then improved and the wavelength shifted to 1.565 µm for simultaneous multi-species detection [102]. 180 GHz of spectral region was covered with this new design and acetylene, nitrous oxide, and carbon monoxide were all detected simultaneously with experimental uncertainty equal to or better than previous MUMAS results. The laser linewidth has been reduced to less than 10 MHz.

MUMAS has also been demonstrated to be compatible with cavity enhanced absorption spectroscopy and wavelength modulation spectroscopy [91]. Through the adaption of the atmospheric oxygen setup, 2f WMS was shown to increase the signal-to-noise ratio by a factor of 3, whilst CEAS alone was shown to be worse. The disappointing results for CEAS were due to the less-than-optimum mirror reflectivity for the wavelengths being used, thus this figure could be improved with better system parameters. A combination of both CEAS and $2f$ WMS resulted in a 4 fold increase in the signal-to-noise ratio compared to direct MUMAS.

2.6 Summary and conclusions

The first half of this chapter has discussed some common gas species and the motivation for their detection. By-products of combustion, medical diagnostics, and environmental monitoring are applications which require detection of these gases. By-products of combustion are relevant gases to monitor because of their ability to be utilized in a controlled feedback loop to regulate the engine. Controlling the amount of fuel introduced into an engine can reduce toxic emissions and increase efficiency. Various schemes for monitoring carbon dioxide, car-

bon monoxide, water, oxides of nitrogen, and hydrocarbons have been mentioned and their sensitivity or precision noted. Selected other species including ammonia and methane have also been discussed due to their industrial and environmental importance. Finally, some of the detection techniques of these gas species have medical breath diagnoses applications such as acetylene as a marker for diabetes and ammonia for renal failure.

A proposal to apply MUMAS to the in-situ simultaneous detection of CO and CO_2 from exhaust gas was made. The motivation for fabricating a small, robust and cheap monitoring system was outlined and the potential application of MUMAS to any potential process control was stated.

After the discussion of particular gas species, a selected number of gas sensing techniques have been discussed and their advantages and disadvantages have been investigated and compared. TDLAS is a common method due to its simplicity but suffers from a limited scanning range and, as such, is normally able to detect only one species. Common types of diode laser used are also briefly discussed. CARS was then mentioned as a good candidate for fast data measurements of a hostile environment such as a flame but suffered from high cost and weak signal generation. DIAL is a good candidate for in-situ detection but is not portable and requires expensive, powerful lasers. BAS is a cheap and simple method which can detect multiple species but suffers from poor resolution often limited by the way in which the spectral information is produced. COSPEC is a rather simple and powerful technique and has the main advantage of being independent of the laser mode quality and stability. Its main weakness is that it requires a reference cell and the reference gas must be at the same temperature and pressure as the target gas. This limits the usefulness of COSPEC for time-varying situations.

Common signal-to-noise ratio enhancements were then explained, which included CRDS, CEAS, off-axis ICOS, WMS, and optical feedback improvements. The signal-to-noise improvement offered by some techniques were quantified, notably CEAS with WMS improved the signal-to-noise ratio of MUMAS on oxygen by a factor of 4. Off-axis ICOS was described as a similar technique to CEAS but the process of entering the cavity off-axis removes un-

wanted feedback from optical surfaces and lengthens the apparent cavity round trip length thus decreasing the free spectral range of the system for a fixed cavity length and size. Wavelength modulation spectroscopy was finally discussed as a noise reducing technique, however, it can suffer from the need for calibration. A calibration-free method has been devised and is now often implemented.

Finally, an introduction to MUMAS was given explaining the results of the first experiments performed using a 760 nm diode laser on atmospheric oxygen. The improvement of the signal-to-noise ratio through CEAS and WMS was described and quantified. The first demonstration of MUMAS in the NIR was described with the use of a home-built solid-state laser. The low Q of the laser cavity resulted in a wide mode linewidth which limited the resolution of the technique. Further work on MUMAS in the NIR resulted in the first demonstration of simultaneous multi-species detection using MUMAS, which was able to detect the concentrations of CO, N_2O and C_2H_2.

Chapter 3

Theory of MUMAS

The concept of MUMAS is described with its relationship to standard absorption spectroscopy and the theory of operation is presented. Aspects of spectral lineshape theory relevant to analysis of MUMAS signals are discussed. A brief outline of laser theory is given underlining the design of multimode lasers for MUMAS and a brief discussion of the optics of Gaussian beams.

Multimode absorption spectroscopy is a recent innovation and proof-of-principle work has already been done [12, 13, 14]. In this chapter, the general theory of MUMAS will be outlined along with fundamental laser theory for multimode laser operation. The quantification of the relevant laser parameters are vital to the successful fitting of the simulation to the measured data and so the validity of all the proposed models needs to be thoroughly investigated.

3.1 Concept of MUMAS

Multimode absorption spectroscopy, MUMAS, is a type of direct absorption spectroscopy whereby the transmitted power of a multimode laser through a gas is monitored. Target gas species in the line-of-sight will absorb laser intensity when they are resonant with any of the laser mode frequencies. The basic principle is displayed in figure 3.1. The modes of the laser are equally spaced by the mode spacing parameter $\Delta\nu_{space}$, have linewidth $\Delta\nu_{mode}$, scan under an envelope of full-width-half-maximum $\Delta\nu_{FWHM}$ with threshold $\Delta\nu_{thresh}$, and are centred at frequency ν_c. These five laser parameters are key to successfully modelling

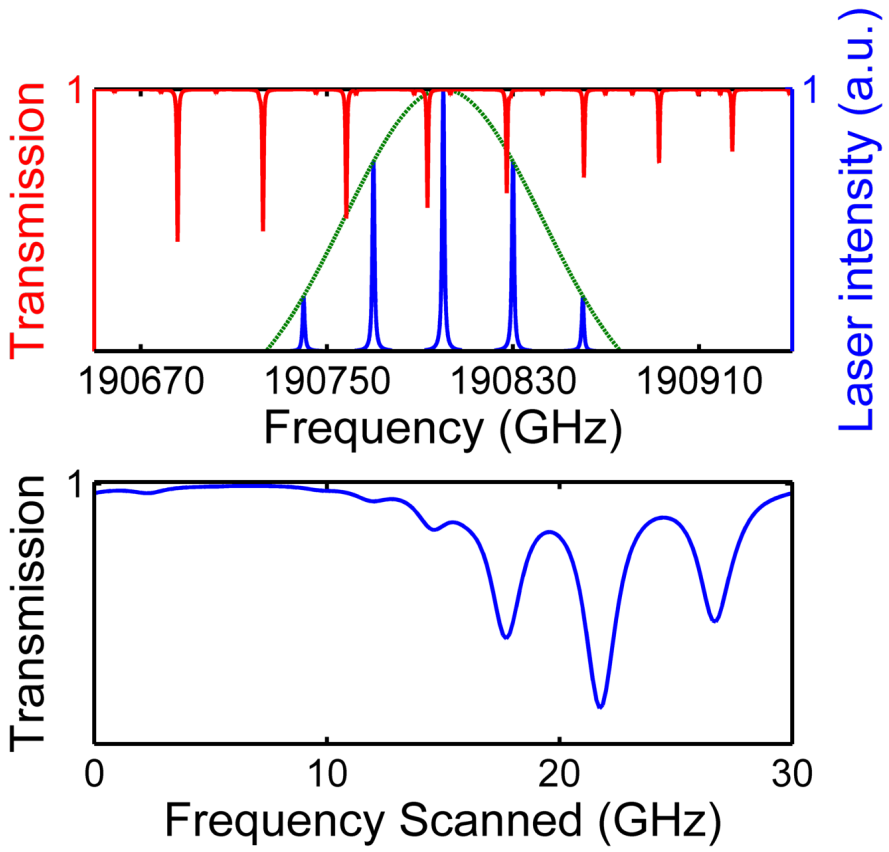

Figure 3.1: The multimode laser, shown in the upper figure (blue) is scanned one mode spacing $\Delta\nu_{space}$ (30 GHz here) and every time one of its modes comes into resonance with an absorption profile (red), the total transmitted power decreases. The total transmitted power is shown in the lower figure and this known as the MUMAS fingerprint. The laser mode intensity follows the green dashed line in the upper figure.

the MUMAS fingerprint. The laser frequencies are longitudinal modes of the cavity and are scanned a distance of $\Delta\nu_{space}$ to produce the MUMAS fingerprint. During this scan any one of the modes may come into resonance with an absorption transition of a target gas species. This will result in laser power being absorbed by the gas and a corresponding decrease in the total transmitted laser power. The variation in the transmitted power is a function that is unique to the particular laser having the specific values of the following parameters: $\Delta\nu_{space}, \nu_c, \Delta\nu_{FWHM}$, $\Delta\nu_{thresh}$, and $\Delta\nu_{mode}$, and the gas parameters: spectral location of the absorption features, total pressure, partial pressure(s), temperature, and path length through gas.

The MUMAS fingerprint is essentially a superposition of n individual single laser mode absorption spectra where n is the number of modes. Each mode will have a starting point

relative to the centre of the laser envelope and will scan a distance of $\Delta\nu_{space}$, with each molecular feature it comes into resonance with featuring somewhere in that scan. Each of the n modes will do this and the resulting transmission is the sum of every laser mode. This technique thus allows high resolution spectroscopy over a broad spectral region, typically 10 MHz resolution over a 200 GHz range. This allows multiple species to be detected as well as multiple lines of the same species. This then allows information pertaining to temperature, pressure, and concentration to be inferred with good precision. The pressure and concentration may be derived from the fitted linewidths of the MUMAS fingerprint, and the temperature may also be derived by using the (temperature dependent) Boltzman distribution of quantum state populations indicated by the relative line intensities, rather than the (temperature dependent) Doppler width which is typically small compared to the pressure broadening at room temperature as in the case of single mode TDLAS.

For high resolution spectroscopy, the laser mode linewidth $\Delta\nu_{mode}$ needs to be considerably smaller than the molecular linewidth $\Delta\nu_{molecule}$. For MUMAS, the mode spacing $\Delta\nu_{space}$ should be larger than the molecular linewidth and comparable to the spacing of the gas absorption profiles[1]. The overall bandwidth $\Delta\nu_{FWHM}$ should be wide enough to encompass multiple lines of any one species. This is obviously limited by the line spacing of the species and the bandwidth obtainable from the laser in question. Also, to increase sensitivity to temperature, it is advantageous to have multiple absorption bands either from one or different gases. Each transition in an absorption band is sequentially labelled by the angular momentum quantum number J starting at $J = 0$ at the centre of the band. The relative population of each quantum state is defined by the Boltzman distribution which is temperature dependent. A higher temperature will result in the higher quantum states having a relatively larger population when compared to cooler conditions whereby the low states are more populated and the higher states are largely unpopulated. This variation of population distribution and its dependence on temperature results in each of the absorption transition intensities being relatively more sensitive to a particular temperature range. The

[1]The mode spacing however should not be an integer multiple of the spacing between any absorption transition lines as this will pose another problem in that all of the transmission dips will appear in the same place.

quantum mechanical angular momentum number J can be used to label this temperature range, thus low J states will be more sensitive to changes at lower temperatures and high J states to changes at higher temperatures.

3.2 The Beer-Lambert Law

MUMAS may be considered an example of normal absorption spectroscopy with the added complication of effectively performing n single mode absorption experiments simultaneously. Provided certain conditions are upheld the Beer-Lambert law can be used to model the fraction of transmitted radiation power through the gas sample in question and is normally given by

$$\frac{I}{I_0} = \exp\left(-N\sigma\ell\right), \tag{3.1}$$

where N is the number density of interacting species, σ is the absorption cross-section, and ℓ is the length of the medium. I_0 is the incident laser power and I is the transmitted laser power. The Beer-Lambert law is a classical relationship and relies on all of the following assumptions being true:

(a) Any absorbers must act independently of each other

(b) The absorbing medium must be homogeneous in the interaction volume

(c) There must be no radiation scattering

(d) Each radiation ray must traverse the same length in the absorbing medium - i.e. rays must be parallel

(e) The intensity of the radiation must not induce optical saturation or optical pumping.

If any of these assumptions are not met, then modifications must be made to equation 3.1.

The cross-section σ takes the form

$$\sigma = S(T)g(\omega - \omega_0), \tag{3.2}$$

where $S(T)$ is the line strength [$\mathrm{cm}^2\,\mathrm{molecule}^{-1}\,\mathrm{cm}^{-1}$] and $g(\omega-\omega_0)$ [cm^{-1}] is the lineshape function which is dependent on temperature and pressure and a Voigt profile is used as this combines both forms of broadening.

3.2.1 Line broadening and lineshape

An extensive database of the possible transmission cross-sections σ is available from the HITRAN database [103]. The lineshape is broadened due to various mechanisms which are either homogeneous or inhomogeneous, so modifications need to be made to the σ term in the Beer-Lambert law. Homogenous mechanisms include lifetime and pressure broadening, and inhomogeneous mechanisms include Doppler broadening. Both mechanisms result in specific lineshape profiles given by Lorentzian and Gaussian shapes respectively.

If the normalized lineshape function is given by $g\left(\omega-\omega_0\right)$, such that

$$\int_0^\infty g\left(\omega-\omega_0\right)\mathrm{d}\omega = 1, \tag{3.3}$$

then the broadened cross-section $\sigma\left(\omega-\omega_0\right)$ is given by

$$\sigma\left(\omega-\omega_0\right) = \sigma_0 g\left(\omega-\omega_0\right), \tag{3.4}$$

where σ_0 comes directly from the HITRAN database.

The absorption peaks at the line centre which is defined as

$$\hbar\omega_0 = E_i - E_j, \tag{3.5}$$

where E_i is the initial state energy and E_j is the final state energy.

Doppler lineshape

The distribution of velocities at thermal equilibrium follows a Maxwellian distribution [104], therefore the inhomogeneous distribution of the resonant group frequencies can be written as

$$g_D(\omega - \omega_0) = \left(\frac{4\ln 2}{\pi \Delta\omega_D^2}\right)^{1/2} \exp\left[-4\ln 2\left(\frac{\omega - \omega_0}{\Delta\omega_D}\right)^2\right]. \tag{3.6}$$

The linewidth $\Delta\omega_D$ is defined to be the FWHM which takes the form

$$\Delta\omega_D = \sqrt{\frac{8\ln 2 k_B T}{Mc^2}}\omega_0, \tag{3.7}$$

where M is the mass of the mass of the molecule, which when simplified gives

$$\Delta\omega_D = 7.136 \times 10^{-7}\sqrt{\frac{T}{A}}\omega_0, \tag{3.8}$$

where T is the temperature in Kelvin and A is the molecular mass number of the species in question. For CO_2 at STP in the NIR ($\lambda = 1570\,\text{nm}$), Doppler broadening leads to a FWHM of approximately 0.3 GHz.

Lorentzian lineshape

The lineshape for most homogeneous broadening mechanisms is a Lorentzian profile [105] and it takes the following form

$$g_L(\omega - \omega_0) = \frac{1}{2\pi}\frac{\Delta\omega_L}{(\omega - \omega_o)^2 + \Delta\omega_L^2/4}, \tag{3.9}$$

where $\Delta\omega_L$ is the total FWHM of all of the homogeneous sources which mainly encompasses two phenomena. Firstly, natural broadening from the finite life time of the upper state E_i

and secondly collisional broadening, or pressure broadening, thus giving[2]

$$\Delta\omega_L = \Delta\omega_{lifetime} + \Delta\omega_{collision}. \tag{3.10}$$

The lifetime broadening is related to the Einstein A-coefficient, hence directly related to the natural lifetime of the state [105]

$$\Delta\omega_{lifetime} \equiv A_{12} = \frac{1}{\tau_{lifetime}}, \tag{3.11}$$

and the collision broadening term is related to the average time between molecular collisions

$$\Delta\omega_{collision} = \frac{2}{\tau_{collision}}. \tag{3.12}$$

Through kinetic theory an expression for $\tau_{collision}$ can be derived and is usually written as the following:

$$\frac{1}{\tau_{collision}} = N \left\langle \sigma\left(v\right)\right\rangle \left\langle v\right\rangle, \tag{3.13}$$

where N is the number density, $\left\langle \sigma\left(v\right)\right\rangle$ is the average collision cross-section and $\langle v\rangle$ is the average relative velocity of the two colliding species. By substituting for N and $\langle v\rangle$ the time between collisions can be re-written as

$$\frac{1}{\tau_{collision}} = \frac{2\sqrt{2}\left\langle \sigma\left(v\right)\right\rangle P}{\sqrt{\pi\mu k_B T}}. \tag{3.14}$$

$\Delta\omega_{collision}$ is therefore proportional to the pressure P and inversely proportional to the square root of the temperature T. μ is the reduced mass of the colliding species.

At STP, and for radiation in the NIR, collisional broadening dominates over lifetime broadening. So for $\lambda = 1570\,\text{nm}$ and $P = 0.1\,\text{atm}$, and looking at a CO transition, the broadening is about 2 GHz.

[2] All broadening terms in equation 3.10 are FWHM.

Voigt lineshape

In the case where $\Delta\omega_L \sim \Delta\omega_D$, any such lineshape function used must incorporate both broadening mechanisms. As shown in figure 3.2, one of the main differences between the two lineshapes can be seen in the wings of the function.

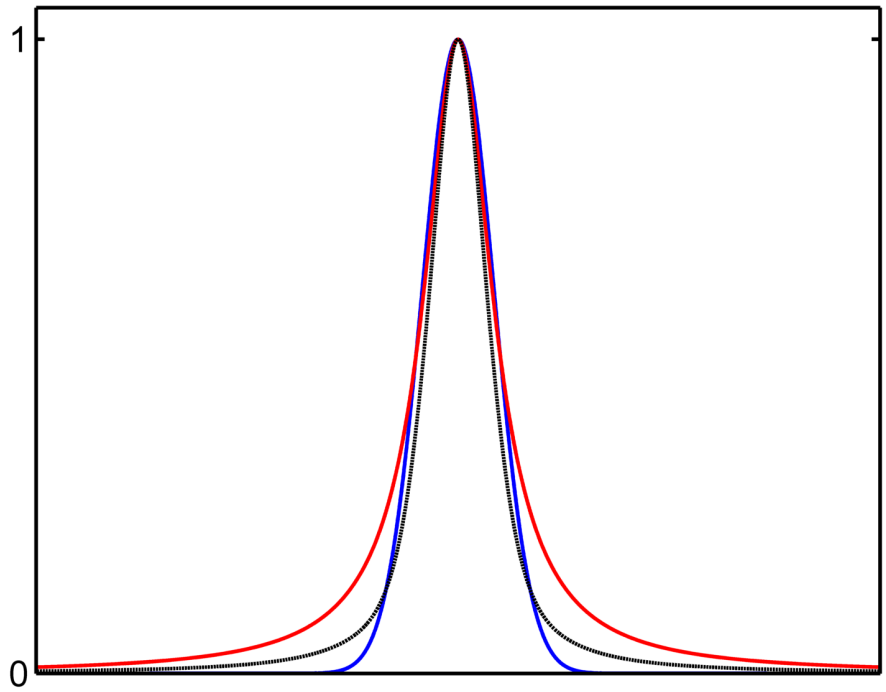

Figure 3.2: Unit-normalized Lorentzian (red) and Gaussian (blue) distribution curves are shown for a given FWHM $\Delta\nu_{FWHM}$. A Voigt profile (black) composed of equal Lorentzian and Gaussian contributions which together have the same FWHM as the other two curves is shown for completeness.

One example of such a function is a convolution of a Gaussian with a Lorentzian distribution. This is known as a Voigt profile and is represented by the following

$$g_V\left(\omega-\omega_0\right)=\int_{-\infty}^{\infty} g_D\left(\omega'-\omega_0\right) g_L\left(\omega'-\omega_0\right)\mathrm{d}\omega'. \tag{3.15}$$

Likewise, this equation can be area-normalized to unity. The FWHM of this lineshape will be a function of both the Lorentzian and Gaussian widths. Whilst this has no exact analytical form many approximations can be found in the literature [106, 107]. An example is also shown in figure 3.2 together with a Lorentzian and Gaussian for comparison.

3.3 Transitions and line strengths

A transition occurs when an initial state energy E_i is turned into a higher state energy E_j through the absorption of a single photon. Transitions of this type are electron dipole coupled. Each energy state belongs to an energy band which can be described as the sum of a vibrational state and various rotational states with the following parameters

$$E_\nu = G_\nu + B_\nu X + H_\nu X^2 + L_\nu X^3, \tag{3.16}$$

where $X = J(J+1)$, G_ν is the effective vibrational energy, ν is the vibrational quantum number, J is the angular momentum quantum number and the other coefficients characterize the rotational energy E_R.

$$E_R = B_\nu X + H_\nu X^2 + L_\nu X^3. \tag{3.17}$$

The absorbed photon has the energy

$$h\nu_0 = E_j - E_i, \tag{3.18}$$

which does not incorporate any broadening parameters.

The transition from one state to another is induced through an electronic dipole transition and the strength can be described by the following equation [108],

$$S_{ij} = S_v \left(\frac{\nu_{ij}}{\nu_0}\right) L \left[1 - \exp(-\frac{hc\nu_{ij}}{k_B T})\right] \exp(-\frac{E_i}{k_B T}) \frac{F}{Q_R}. \tag{3.19}$$

See appendix A for a full explanation of the terms. In this chapter, it suffices to discuss the density of states Q_R and the population densities. These transitions can also be implemented by other processes such as magnetic dipole and electric quadrupole transitions, however these are substantially less favoured and the probabilities are insignificant in comparison.

The initial populations in both the upper and lower state can be modelled by a Boltzman distribution assuming thermal equilibrium. The temperature T, statistical weights and

angular momentum J will affect the system, with the latter two properties being a measure of the degeneracy. In general, the number density of atoms N_a populating a given state a with energy E_a is given by

$$N_a = \frac{N_{tot}}{Q_a}(2J_a + 1)\exp(-\frac{E_a}{k_B T}), \tag{3.20}$$

where N_{tot} is the total number of atoms per unit volume and Q_a is the partition function. The partition function is the sum over all possible states and is described by

$$Q_a = \sum_a (2J_a + 1)\exp(-\frac{E_a}{k_B T}). \tag{3.21}$$

Equation 3.18 calculates the position of the transitional lines and equation 3.19 provides the strength of each transition, provided the temperature is known.

3.4 Laser theory

A laser is a device that can generate and amplify light, where light is broadly defined as the radiation emitted from a range of amplifying media with wavelengths that include the infrared. In general terms a laser consists of several key components: a laser medium, a pumping device, and a suitable optical feedback process. The feedback is often provided by an optical cavity, and a simple setup is shown in figure 3.3 [104]. The laser medium can be in any state of matter. Lasers have been demonstrated using solid, liquid, gaseous, and plasma mediums. The production of the population inversion which is vital to laser operation depends upon the particular design, and the common methods include flash-lamps producing UV light, strong electric potential, optical pumping using other lasers, and driving current in the case of semiconductor lasers.

For a laser oscillator to work the round trip losses have to be exceeded by the round trip gain. If this occurs, then the signal intensity increases for each round trip of the cavity. A proportion of the power is then leaked from the cavity at the output mirror in a coherent,

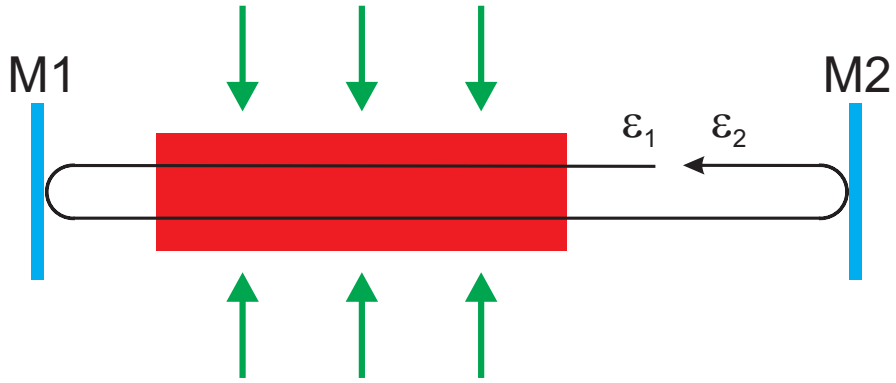

Figure 3.3: The basic components of a light amplification system are shown. Mirrors M1 and M2 form a cavity and the gain medium (red) amplifies the signal which starts as a result of spontaneous emission. The population inversion inside the gain medium is provided by some pumping technique. Shown here as green arrows, which can be optical, high voltage, or current based. ϵ_1 and ϵ_2 are the signal strength before and after a round trip respectively.

directional manner. If one mirror has reflectance R_1 and the other R_2, the laser medium has length L_m, and cavity length L, then the ratios of the signals before (ϵ_1) and after (ϵ_2) one round trip are, in a steady state, given by [3]

$$\frac{\epsilon_2}{\epsilon_1} \equiv R_1 R_2 \exp\left(2\alpha_m L - 2\kappa_c L - i2\omega L/c\right) \geq 1. \tag{3.22}$$

In equation 3.22, α_m represents the gain coefficient of the gain medium, κ_c signifies the total losses from the cavity, and the complex component is the round-trip phase condition.

The complex phase component must be equal to unity which implies that

$$\frac{2\omega L}{c} = q2\pi, \tag{3.23}$$

where q is an integer. In the linear cavity this phase condition gives rise to a standing wave and imposes a condition on the frequencies which can be produced by the cavity. These

[3]Here, L is the optical cavity length, which takes into consideration the refractive index of the different materials.

frequencies, $\omega_q = 2\pi\left(\frac{qc}{2L}\right)$, are the resonant frequencies of the cavity which are discrete and equally spaced. These frequencies are known as axial modes or longitudinal modes and give rise to the discrete frequency output of any laser cavity system.

3.4.1 Laser linewidth

As discussed earlier in this chapter the lineshape of the laser mode is one of the five parameters to describe the multimode laser. If $\Delta\nu_{mode} \ll \Delta\nu_{molecule}$ then the functional form of $\Delta\nu_{mode}$ will not be a critical parameter and any suitable approximation will suffice. Such an approximation can be found by using the resonance line broadening caused by energy loss from a passive cavity [104].

A passive cavity resonator contains an initial intensity I_0 of light within the cavity. After p round trips, the intensity $I\left(t_p\right)$ at time t will be given by

$$I\left(t_p\right) = \left(R_1 R_2 \left(1 - T_d\right)^2\right)^p I_0, \tag{3.24}$$

where R_1 and R_2 are the reflectivity of the two cavity mirrors, T_d is the round trip cavity loss due to diffraction. The time t and number of round trips p are related through $t_p = \frac{2pL}{c}$. Substituting this into equation 3.24 and assuming an exponential decay function of the form

$$\frac{I\left(t\right)}{I_0} = \exp\left(\frac{-t}{\tau}\right), \tag{3.25}$$

τ, the photon lifetime in the cavity turns out to be

$$\tau = \frac{-2L}{c\ln\left(R_1 R_2 \left(1 - T_d\right)^2\right)}. \tag{3.26}$$

Resonance line broadening is the result of energy loss from the resonator cavity. Given that the electric field amplitude is related to the square root of the intensity I, the plane wave solution of a propagating wave can be modified to include this exponential decay and is

written as

$$\mathbf{E}(t) = \mathbf{E}_0 \exp\left(\frac{-t}{2\tau} + i\omega t\right). \tag{3.27}$$

The frequency transmission function of a passive resonant cavity is found by taking the squared modulus of the Fourier transform of equation 3.27. The result is a Lorentzian profile, equation 3.28.

$$F(\omega - \omega_0) = \frac{1}{\pi} \frac{\gamma}{(\omega - \omega_0)^2 + \gamma^2}, \tag{3.28}$$

where $\gamma = \frac{1}{2\tau}$ is the HWHM of the Lorentzian lineshape. If gain medium is placed within the cavity then this lineshape is going to be amplified and the resulting function may be different than the passive case.

The power gain measured in dB has the same lineshape as the complex atomic lineshape susceptibility [104]. The gain profile of a laser medium can be mathematically described by the complex atomic susceptibility and is dependent on the population inversion. Some example gain curves are shown in figure 3.4 [109]. The lineshape in figure 3.4 is a logarithmic function, so if it takes the shape of a Lorentzian curve, which is the case for homogeneous media, then gain narrowing will occur. In the inhomogeneous case the gain curve can be approximated to be a constant across the laser mode. Gain narrowing does therefore not occur on the same scale but this is still an approximation. Hence the final laser mode profile should be Lorentzian-like, and given that its value is $\sim$10 MHz, which is significantly smaller than the molecular linewidth($\sim$ 1 GHz), then this approximation should be suitable. Using mirror reflectivities of 0.9999 and 0.98, cavity length of 5 mm and no diffraction loses, the HWHM of the unamplified transmission function from a passive resonator cavity is $\sim$ 50 MHz.

Following on from equation 3.25, the cavity quality factor Q can be introduced which is defined as

$$Q = 2\pi \frac{\text{stored energy}}{\text{energy loss per cycle}} \tag{3.29}$$

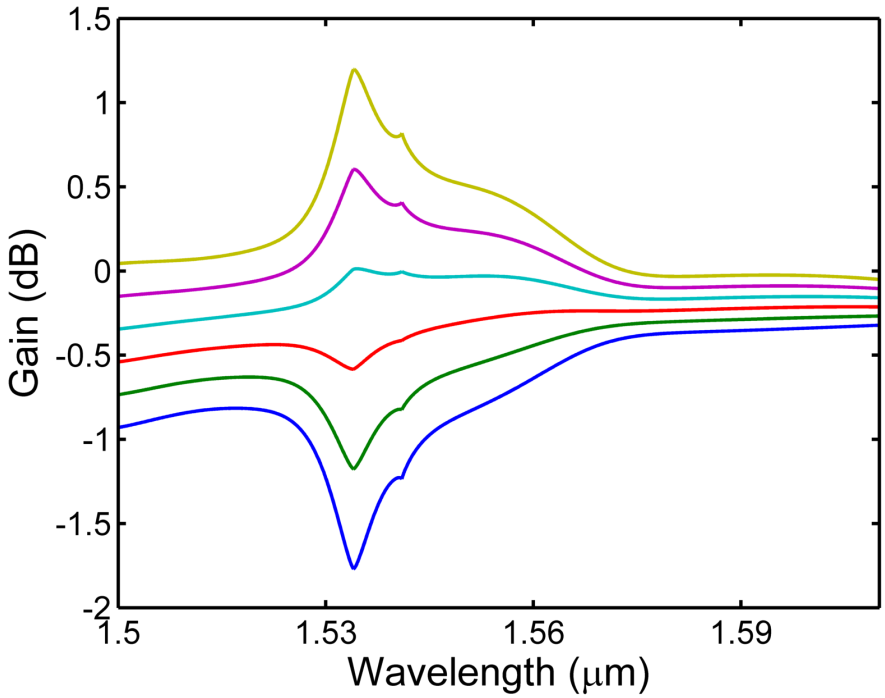

Figure 3.4: Figure shows a family of curves representing the cross-sectional gain of erbium-doped glass. Each different curve has a different population inversion. The blue line has no population inversion, green has 20%, red 40%, cyan 60%, purple 80%, gold 100%. Calculations were done on the assumption of 1 mm of laser gain medium in a 5 mm optical length cavity.

The energy stored in a cavity is $\chi h\nu$ where χ is the photon number and is proportional to the intensity I. The energy lost per cycle is given by $\frac{1}{\nu}\frac{\mathrm{d}\chi}{\mathrm{d}t}h\nu$. Using these two expressions and equation 3.25 leads to

$$Q = \frac{\nu}{\Delta\nu_c}, \tag{3.30}$$

where $\Delta\nu_c = 1/2\pi\tau$. This expression shows that the cavity Q factor is the ratio of the cavity resonance frequency ν and the cavity linewidth $\Delta\nu_c$.

3.5 Optics

3.5.1 Cavity stability

In general optical cavities are not made with planar mirrors. The stability of a cavity can be calculated from the geometry of the mirrors and the distance between them [110]. For a

cavity to be considered stable the output ray vector must be equal to the input ray vector multiplied by a constant factor. This can be represented in matrix format as

$$\begin{pmatrix} r_2 \\ \theta_2 \end{pmatrix} = \lambda \begin{pmatrix} r_1 \\ \theta_1 \end{pmatrix}, \tag{3.31}$$

where r and θ are the radial and angular coordinate of the light ray. The two cavity resonator mirrors are the equivalent of a series of lenses of focal length f separated by a distance d, which can be represented as the matrix operator M, given by

$$\mathrm{M} = \begin{pmatrix} 1 & d \\ -\frac{1}{f} & 1 - \frac{d}{f} \end{pmatrix}. \tag{3.32}$$

The eigenvalues of equation 3.32 give rise to the following two solutions.

$$\lambda = g \pm \sqrt{g^2 - 1} \text{ for } |g| > 1 \tag{3.33a}$$

$$\lambda = g \pm i\sqrt{1 - g^2} \text{ for } |g| < 1, \tag{3.33b}$$

where $g = 1 - \frac{d}{2f}$.

Equation 3.33a gives a λ value greater than one, thus resulting in an unstable optical cavity.

Equation 3.33b however, leads to a λ value less than one, which results in a stable cavity alignment which gives rise to the condition

$$\left| 1 - \frac{d}{2f} \right| < 1. \tag{3.34}$$

For an asymmetric cavity, with two mirrors of focal length f_1 and f_2, the criterion can be generalized to

$$0 < g_1 g_2 < 1, \tag{3.35}$$

with $g_1 = 1 - \frac{d}{2f_1}$ and $g_2 = 1 - \frac{d}{2f_2}$. For a curved mirror, $f_i = \frac{R_i}{2}$, which finally leads to

$$g_1 = 1 - \frac{d}{R_1} \tag{3.36a}$$

$$g_2 = 1 - \frac{d}{R_2} \tag{3.36b}$$

Equations 3.36 are the criteria for cavity stability. There are three special examples to consider

1. $g_1 = g_2 = 1$, which is plane parallel.

2. $g_1 = g_2 = 0$, which is symmetric confocal.

3. $g_1 = g_2 = -1$, which is symmetric concentric.

and these are elaborated on later in the chapter.

3.5.2 Gaussian optics

The output of a laser system can often be better described by Gaussian beams rather than plane waves. The intensity distribution decays away from the central axis (z) in all directions (x and y axes), and for the TEM_{00} modes, can be written as A^*A, where

$$A\left(x, y, z\right) = \exp\left(-i\left[P(z) + \frac{k(x^2 + y^2)}{2q(z)}\right]\right). \tag{3.37}$$

$P(z)$ is the phase factor, $k = 2\pi/\lambda$, and $q(z)$ is the complex radius of curvature of the wavefront. The complex radius of curvature is often written in terms of the phase front curvature $R(z)$ and its beam spot size w.

$$\frac{1}{q} = \frac{1}{R} - \frac{i\lambda}{\pi w^2} \tag{3.38}$$

The intensity pattern can then be represented as

$$I = A^* A = \exp\left(\frac{2r^2}{w^2}\right), \tag{3.39}$$

where $r^2 = x^2 + y^2$.

For any Gaussian beam the place at which the beam spot size is minimum is referred to as the beam waist and takes the value w_0. At the beam waist the phase front radius of curvature is infinite. Within the vicinity of the beam waist the wave fronts can be approximated as parallel and this region is known as the Rayleigh range z_R, which is defined as the displacement from the beam waist out to the point z_R such that the beam radius has increased by a factor of $\sqrt{2}$ or the area has doubled, and it is represented by equation 3.40.

$$z_R = \frac{\pi w_0^2}{\lambda} \tag{3.40}$$

For any value of z along the propagation axis from the beam waist, the beam diameter is given by

$$w^2(z) = w_0^2\left(1 + \left(\frac{z}{z_R}\right)^2\right). \tag{3.41}$$

For $z \ll z_R$, the beam diameter can be approximated to the original beam waist w_0 which results in planar wave fronts.

3.5.3 Cavity modes

Equations 3.36 are the cavity parameters which define the stability of the cavity. When applied to a Gaussian beam profile, assuming TEM_{00} mode only, the resonant modes of the cavity will have a Rayleigh range given by

$$z_R^2 = \frac{g_1 g_2 (1 - g_1 g_2)}{(g_1 + g_2 - 2 g_1 g_2)^2} d^2. \tag{3.42}$$

This leads to individual spot sizes on each cavity mirror of

$$w_1^2 = \frac{d\lambda}{\pi}\sqrt{\frac{g_2}{g_1\left(1-g_1g_2\right)}} \tag{3.43a}$$

$$w_2^2 = \frac{d\lambda}{\pi}\sqrt{\frac{g_1}{g_2\left(1-g_1g_2\right)}} \tag{3.43b}$$

and these values need to be much less than the radius of curvature of any cavity mirror in order to avoid diffraction losses ($T_d \sim 0$).

A genuinely planar cavity will be of little practical use as the beam will rapidly wander off the axis unless the mirrors are perfectly parallel. A polished piece of glass or crystal manufactured out of the gain medium is a potential design for such a laser.

A confocal cavity design is less sensitive to misalignment of either mirror and has, on average, the smallest spot size along the entire axis of the resonator.

A concentric cavity has the smallest spot possible out of the cavity designs, but also a sizeable spot on each of the cavity mirrors. This resonator is sensitive to mirror misalignment and is heavily prone to diffraction losses.

Phase shift treatment

Whereas in a plane wave approximation the free spectral range is given by

$$\Delta\nu = \frac{c}{2d}, \tag{3.44}$$

this is not the case for a Gaussian wave. The full treatment is complex, but in short, there is an extra phase shift of $\frac{\pi}{2}$ each time the wavefront goes from a far field to the focus. For non-TEM_{00} it is even more complex. However, this treatment can be avoided provided z (and therefore the cavity length) is not significantly larger than z_R.

3.6 Summary and conclusions

The theory of MUMAS has been explained and the importance of accurately knowing the laser parameters has been discussed. The impact of the mode spacing on the MUMAS fingerprint has been alluded to because it needs to be much larger than the molecular linewidth so that the measured signal is not too complex, but not so large as to prevent the laser from scanning effectively.

Due to MUMAS being a direct absorption technique the Beer-Lambert Law has been discussed in detail along with standard broadening mechanisms dependent on temperature and pressure, as these will be relevant to the simulation of the MUMAS spectra. Due to both homogeneous and inhomogeneous mechanisms having non-negligible contributions to the width of the absorption features, the Voigt profile was proposed as a suitable model.

The theory behind the absorption transition lines of the target gas species has been discussed with the importance of temperature highlighted. Laser theory of a resonator cavity has also been explained and a rudimentary model of the laser linewidth proposed, but provided that the linewidth itself is significantly smaller than the molecular linewidth, the exact form of this model was not important to the simulation.

Finally, Gaussian optical theory was introduced and its relevance to the cavity stability was discussed as well as its dependence upon the type of cavity used. The use of Gaussian beam optics as a way of deducing the beam or cavity waist is proposed as this will have influence upon the design of the laser and associated pumping optics. A brief discussion of Gaussian cavity modes was presented. The free spectral range of a Gaussian cavity is much more complex than the plane wave approximation, but provided that the cavity length is comparable to or less than the Rayleigh length, then the plane wave approximation of the cavity length can be used.

Chapter 4

Experimental apparatus and procedure

This chapter explores the design process of the multimode laser used to measure the carbon dioxide and carbon monoxide in exhaust gas. Firstly by examining the spectral overlap of the absorption lines and comparing it to available laser gain media. Next, different types of laser cavity are discussed and evaluated based upon their ability to produce smooth scanning of the laser modes. A laser design is then proposed and built with its characteristics (power, mode spacing, laser linewidth) being presented and evaluated near the end of the chapter.

The characterisation of any new system is crucial to its repeatable and stable operation. This process of understanding the new system starts during the design phase where ambitions are laid out and compared to what is achievable with current technology and available resources.

After construction of a prototype, analysis of the performance is necessary to optimize the parameters and suggest improvements for the next version of the setup. This chapter goes on to look at the design process of the laser system and then at the final characterisation of the laser including laser linewidth, scanning smoothness, centre frequency, and optimal mode spacing.

4.1 Laser design

4.1.1 Overlap of carbon monoxide and carbon dioxide lines

Carbon dioxide and carbon monoxide overlap in two spectral regions with any significant line strength: 1566 nm - 1622 nm and 4400 nm - 5150 nm. The latter region is in the mid infrared and can be accessed by quantum cascade lasers, inter-band cascade lasers or super-cooled lead-salt diodes. The detector technology in this region is somewhat lacking in comparison to the near infrared. Background noise is very high which makes sensitive detection problematic. The overlap in the NIR has inferior line strength, but the technology for the region is far more advanced, mainly because this is the telecommunications region. A summary of the spectral lines is displayed in figure 4.1. The reason for the difference in line strength, which

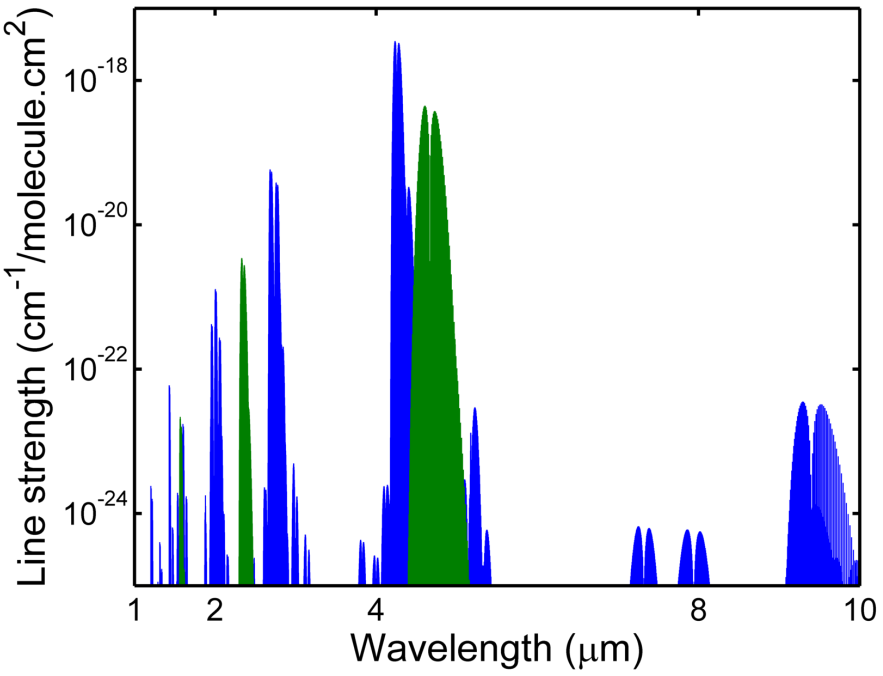

Figure 4.1: The transitions of carbon dioxide (blue) and carbon monoxide (green) are shown over the spectral range of 1 µm to 10 µm. There is a useable overlap around 1.5 µm and 4.8 µm.

can be several orders of magnitude, is due to the NIR transitions being overtones and the IR transitions fundamental. In equation 3.19, $S_{\nu_{ij}}$ contains the matrix element of the transition. This matrix element involves the dipole operator and the initial and final state wavefunctions. Overtones are weaker than fundamental transitions because the wavefunctions do not overlap

as much, thus the probability of a transition from an excited state to the next excited state on the harmonic oscillator ladder is reduced.

The NIR spectral overlap region is shown in figure 4.2.

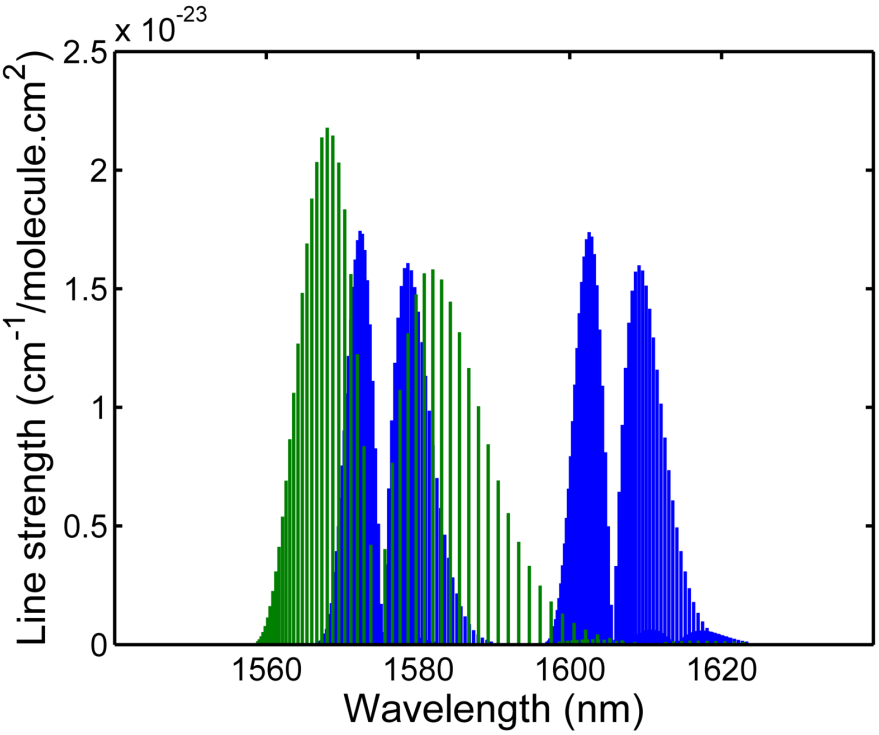

Figure 4.2: The transitions of carbon dioxide (blue) and carbon monoxide (green) are shown over the spectral range of 1550 nm to 1630 nm. For typical ratios found in exhaust gas, 1569 nm and 1586 nm are preferred such that both gases have similar signal strengths.

In typical engine exhaust gas the ratio of carbon dioxide to carbon monoxide is approximately 10:1 [111]. As such, the ratio of the line strengths should be the opposite of this as much as possible to give similar signal-to-noise ratios.

4.1.2 Laser gain medium

With a spectral region identified a suitable inhomogeneous gain medium must be chosen to coincide. Erbium:ytterbium doped phosphate glass is suitable as it is readily available in high quality production from numerous suppliers due to its common use in telecommunications. The Er^{3+} ions are the gain medium and the Yb^{3+} ions are used to efficiently pump the active ions by readily absorbing radiation around 976 nm and then transferring it over to the

Er^{3+} ions through collisions within the host material. The host material is phosphate glass as this exhibits chemical durability when compared to silicate glasses, and the particular type of glass (QX) can withstand high thermal loading and shock. The glass was produced by Kigre Inc., then cut and polished to size. The glass was cut and polished with a 10-5 scratch dig and $\frac{\lambda}{10}$ flatness to the surfaces. Overall 16 pieces of glass were produced. A summary of the laser glass used is given in table 4.1. The gain available from erbium doped

Table 4.1: Summary of properties of QX glass used in laser design.

QX laser glass	
Peak wavelength	1535 nm
Refractive index	1.532
Number density Er^{3+}	1.46×10^{20} ions/cc
Number density Yb^{3+}	$\sim 1.9 \times 10^{21}$ ions/cc
Scratch dig	10-5
Flatness	$\frac{\lambda}{10}$

glass is shown in figure 4.3 along with the spectral region in which the carbon monoxide and carbon dioxide lines overlap, given in red. The peak of the erbium gain curve will need to

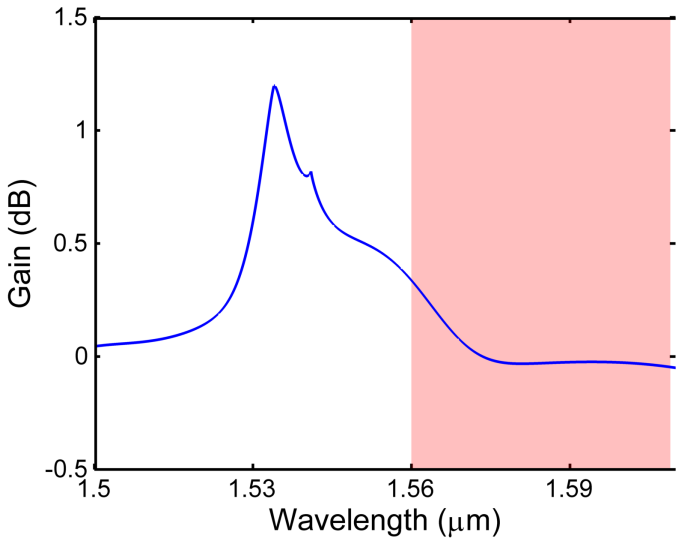

Figure 4.3: The spectral overlap of the erbium gain with CO/CO_2 spectral lines is shown in the shaded region. One problem is that the highlighted area does not contain the peak of the gain curve which is the preferred lasing wavelength (1534 nm). The gain will need to be suppressed at the shorter wavelengths if the spectral region for CO and CO_2 is to be accessed.

be suppressed if the laser is to operate at wavelengths higher than 1566 nm. This is done by utilising a custom mirror coating on one of the cavity mirrors which has low reflectivity

at shorter wavelengths and then rapidly tends to high reflectivity at 1566 nm. This coating, manufactured by Layertec Inc., was placed on the input coupler of the laser system. The reflectivity is displayed in figure 4.4.

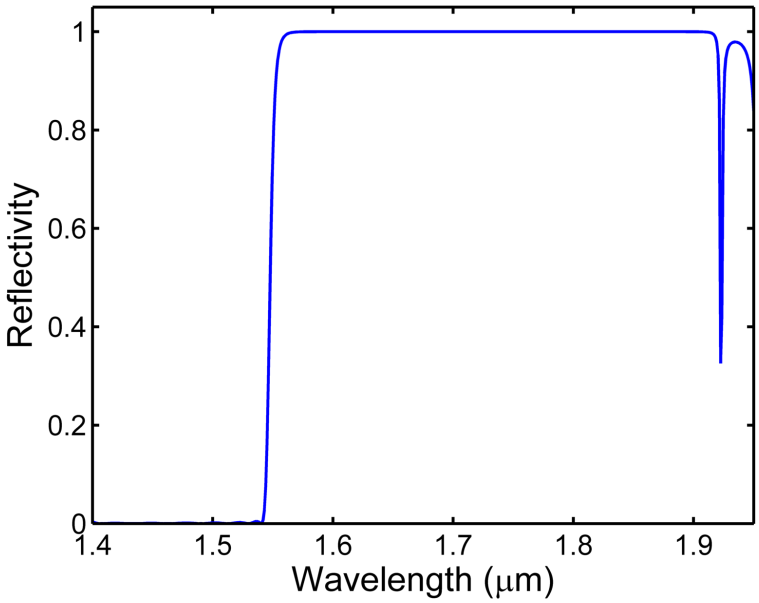

Figure 4.4: The reflectivity of the input coupler of the laser cavity is shown. The reflectivity is effectively unity when the wavelength reaches 1568 nm.

4.1.3 Cavity design

With any solid state laser, the method of tuning the operating wavelength(s) is to vary the cavity length. This can be done in several ways. Some proposed methods include variation of cavity temperature, pressure of gas within the cavity and through use of an actuator. The simplest and most controlled method is through actuation of the cavity, and a piezo-electric transducer (PZT) actuator ring from Noliac (NAC2124) was used for this purpose. The laser cavity must be rigid in design, flexible enough to allow adjustment of the cavity length, immune to cavity misalignment, and robust to withstand vibrations and other common forms of noise. Through trial of different cavity designs a barrel-style laser was produced with two components comprising the optical cavity. The cavity was planar/concave with an input coupler with radius of curvature of 25 mm and a planar output coupler. The output coupler was made of QX/Er glass in the shape of a truncated right angled prism with a

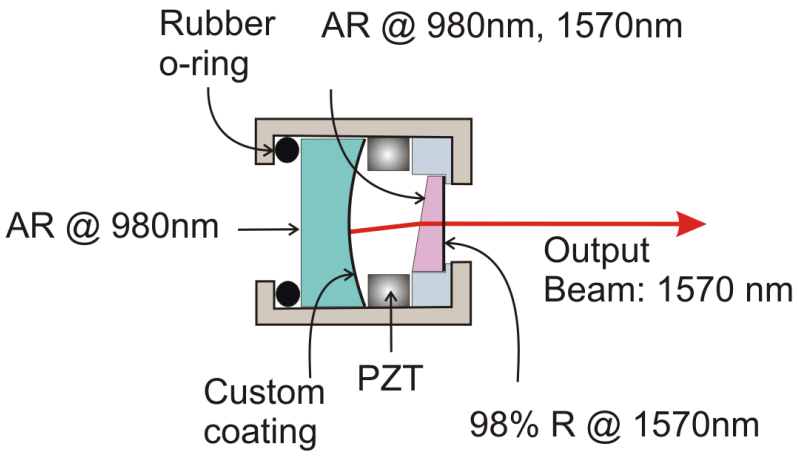

Figure 4.5: The laser cavity design is shown with the relevant optical coatings labelled in the diagram. The two components of the optical cavity are compressed within an aluminium barrel onto a rubber o-ring for stability. The piezo-electric transducer (PZT) expands and contracts when a high voltage (up to 200 V) is applied across it. The custom coating refers to figure 4.4.

7.6° angle on one of the planes. The wedged design is to remove any intra-cavity etalons which would interfere with the multimode lasing of the system. Similarly, feedback from any surface outside of the laser would result in unstable multimode operation and competition. To prevent this from happening an optical isolator utilising Faraday rotation is used to isolate the laser from the rest of the system. The output face was coated such that it was 98% reflective at 1570 nm. The inside angled face was anti-reflection (AR) coated for both 1570 nm and 980 nm to reduce losses. The input coupler was a half-inch BK7 substrate with a planar face and 25 mm radius of curvature concave face. The concave face was coated with the custom reflectivity coating shown in figure 4.4 which was also AR coated for 980 nm. The planar face was AR coated for 980 nm likewise. The cavity arrangement is shown in figure 4.5 along with the various coatings on each face. A CAD drawing of the laser cavity is shown in figure 4.6.

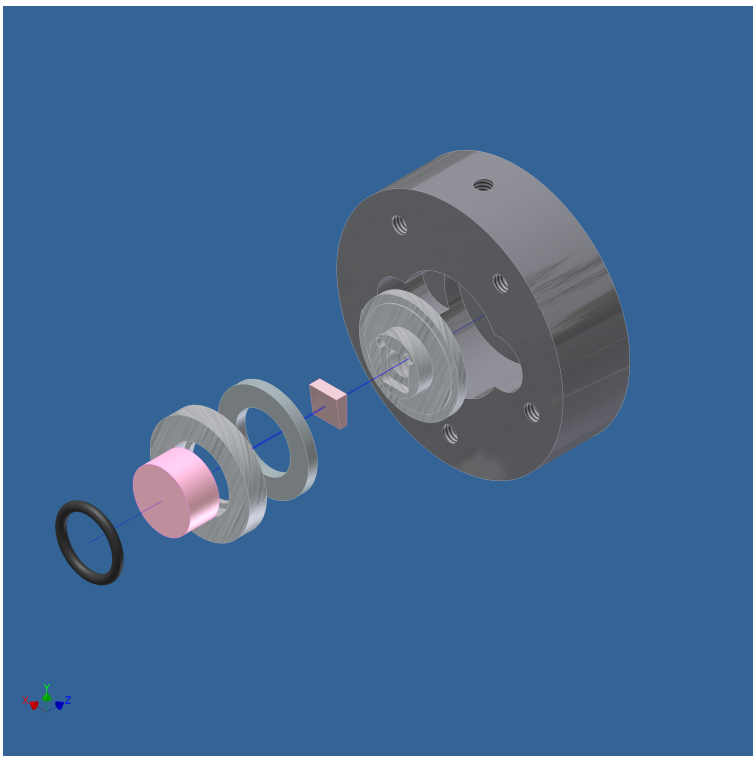

Figure 4.6: An explosion of the laser cavity design drawn using Autodesk Inventor®. The end cap which bolts onto the main housing has been left out for clarity. The two optics are represented in pink and the o-ring is black. The components are from left to right: o-ring, 25 mm radius of curvature substrate with custom coatings, aluminium holder, PZT, erbium wedge, aluminium holder, aluminium casing.

Cavity properties

With a planar($R = \infty$)/concave($R = 25\,\text{mm}$) cavity the stability values g, for a cavity length of 5 mm, are $g_1 = 1$ and $g_2 = 0.8$ respectively from equations 3.36a and 3.36b. This results in a Rayleigh range z_R of about 1 cm from equation 3.42. As this is larger than the cavity length, diffraction losses from the cavity are reduced and the cavity is insensitive to small misalignments.

The beam waist w_0 is 70 µm, which due to the shape of the cavity, is equal to the beam spot size on the planar mirror w_1 (equation 3.43a). The beam size on the other mirror is 79 µm from equation 3.43b.

4.1.4 Pumping optics

The laser is pumped using 976 nm radiation with a power of 1 W from an APC fibre-coupled diode laser (Roithner RLCO-980-1000-F). The pump light is focused into the laser using two aspheric lenses with a focal length of 50 mm such that the fibre core of diameter 100 µm is imaged 1:1. For efficient pumping of the resonant laser cavity, the two beam waists must efficiently overlap. As the pump light is incident through the input coupler as shown in figure 4.7, it must be placed at a slight angle to the perpendicular of the cavity.[1] The fibre is terminated with an angle polished cut to reduce feedback into the pump laser medium.

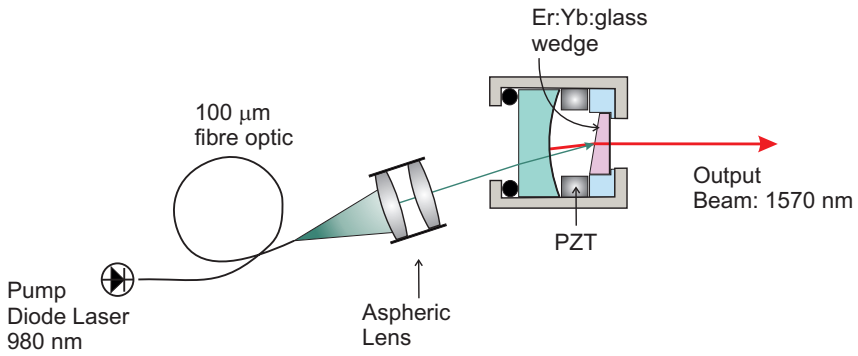

Figure 4.7: The setup of the multimode laser system complete with pump optics.

4.2 Laser performance and characteristics

The laser was optimized for smooth scanning which meant that power output was not maximal. However this is not crucial to the setup. The laser operated within the predicted spectrum and an example image of the mode structure is given in figure 4.8. The modes are centred at 1571 nm. The image was taken using a Bristol Instruments 721B spectrum analyser whilst the modes were static.

[1] This angle is overdramatized in the image for clarity.

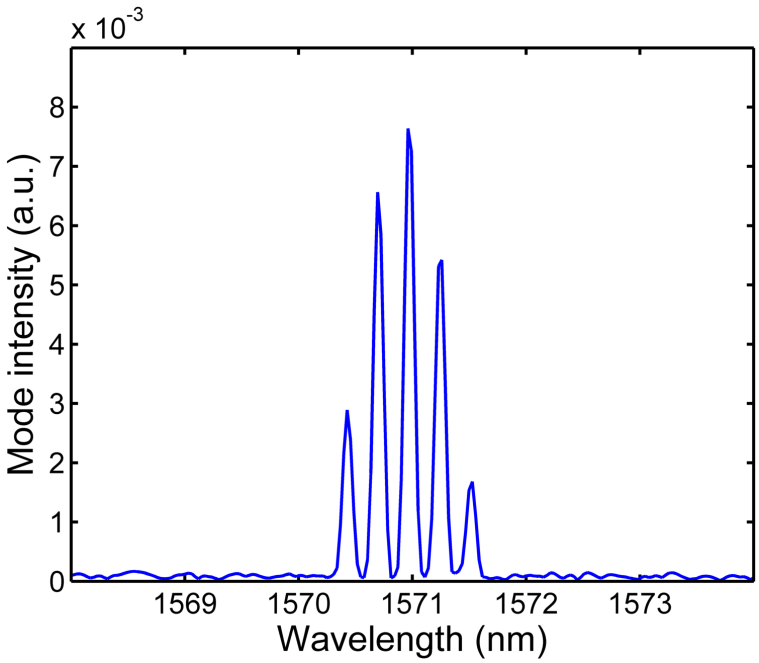

Figure 4.8: A spectrum of the laser modes produced by the erbium gain medium. The spectrum was taken whilst the PZT was static, but 6 modes can be in existence at any one time.

4.2.1 Laser linewidth

The line width of the strongest mode was estimated to be 5 MHz using a Thorlabs Fabry-Perot analyser SA200-12B. The data with a Lorentzian fit is shown in figure 4.9. The resolution of this instrument is 7.5 MHz, so this is only an estimate of the laser linewidth. Given that the typical width of an absorption feature it will be detecting will be of the order of a few gigaHertz, this number isn't overly critical[2].

[2]From fitting MUMAS spectra, a suitable linewidth value to use in the simulation is 8 MHz

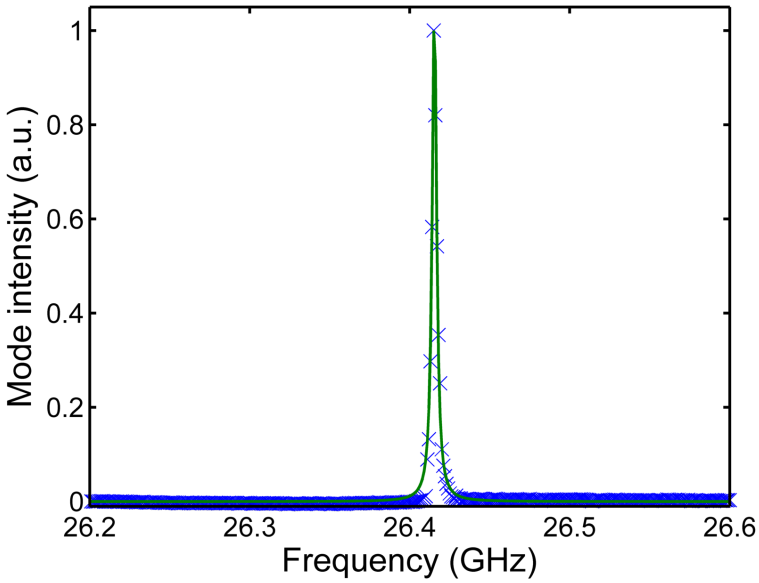

Figure 4.9: The data points (blue) from the Thorlabs Fabry-Pérot analyser are shown with a best fit Lorentzian curve (green). The FWHM of the fit is 3.3 MHz which is less than the quoted instrument resolution of 7.5 MHz. However this figure concludes that the laser linewidth has an upper limit of 7.5 MHz, which is sufficient for the MUMAS model. The true line shape measured is actually a convolution of the laser line shape and the instrument lineshape, but a Lorentzian fit is good and it supports the assumption of 8 MHz linewidth in our model. The data collected is a single shot measurement and it is not unreasonable to assume that the time-averaged linewidth may be broader.

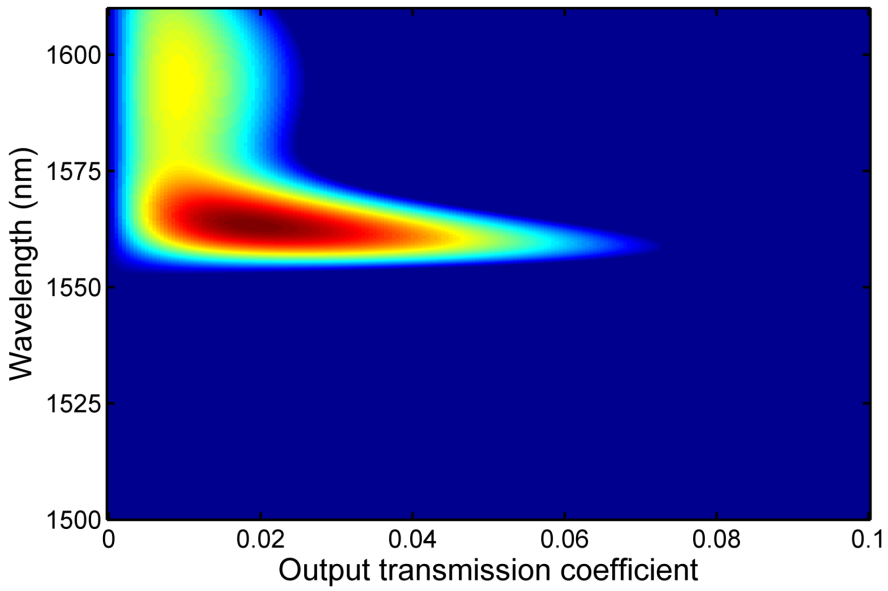

Figure 4.10: This false colour plot shows how the output power behaves as a function of the amount of light that leaks out of the cavity. The false colour has been assigned the 'jet' configuration with dark red being maximal and dark blue being minimal. The image shows the potential wavelength output of the laser system as a function of transmission coefficient (x-axis), and the Layertec mirror coefficient (y-axis). The output maximum is peaked around 1564 nm, however this model does not consider optical alignment or the error tolerance in the Layertec mirror coating.

4.2.2 Power output

The output power is determined by the reflectivity coefficients of the cavity elements as well as the pumping laser intensity. A theoretical map showing the normalized power output as a function of output coefficient and gain is shown in figure 4.10. This graph assumes that the reflectivity of the other mirror is close to 1 for the accepted wavelengths and zero elsewhere. The image shows a large dependency on the position of the edge of the input coupler but also confirms that an output loss of 2% would be optimal for output power.

Whilst output power is not an crucial factor, tens of milliwatts is desirable for ease of alignment and sensible detector limits. A power output of 22 mW was achieved with a pumping power of 580 mW which produced a laser mode packet that scanned smoothly when the cavity length was modulated.

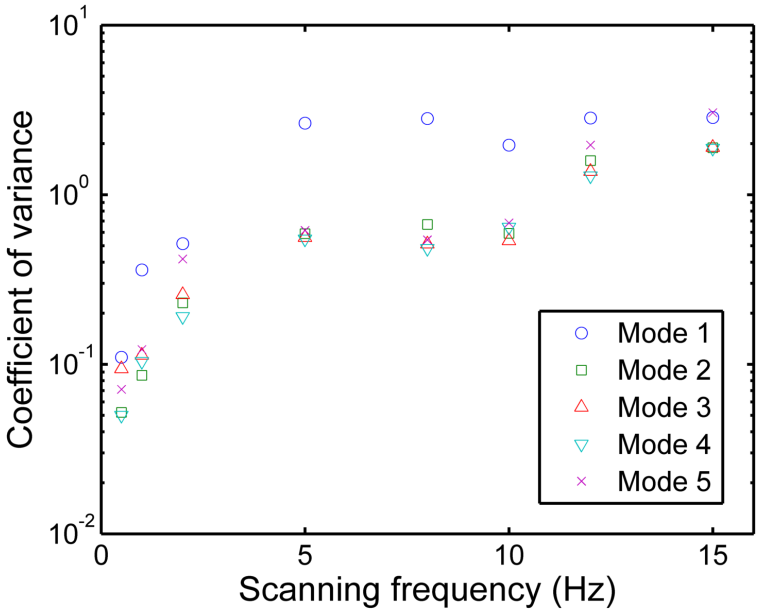

Figure 4.11: A measure of the mode tuning stability as a function of scanning frequency. By monitoring the coefficient of variance of 5 continuous modes during a scan, an arbitrary measure of their stability can be determined. The plot shows how scanning above 10 Hz does not produce a stable laser mode structure and between 5 Hz and 10 Hz little difference is demonstrated. The mode structure is most stable when below 3 Hz, so a scanning frequency of 2 Hz seems reasonable.

4.2.3 Scanning operation

The laser modes are tuned through the lengthening of the laser cavity by a piezo-electric transducer (PZT). This ceramic disk expands and relaxes through the application of an electric field and the response and behaviour of the actuator is vital to the performance of the MUMAS system. By monitoring five continuous modes as they scan under the envelope using the Czerny-Turner spectrometer, their stability can be plotted as a function of scanning frequency. Stability is measured by the coefficient of variance, which is the standard deviation divided by the mean. The results of which are shown in figure 4.11. It is believed that the scanning frequency limitation is caused by the PZT response to the applied electric field, possibly as a result of the electrodes being placed on opposite sides of the ring. A slow modulation results in improved mode stability however this must be balanced against practicality of the measurement time. It should be noted however that this frequency limitation is a result of the current laser design, not a fundamental property of MUMAS. If semiconductor-type lasers could be used then the mode scanning frequency could be in the kilohertz region.

By studying figure 4.11, it is deduced that the most appropriate scanning frequency for the PZT is 2 Hz. Scanning at frequencies larger than 10 Hz results in an unstable mode packet. It should be noted that the reason for the apparent offset of mode 1 compared to the others is that it has a weaker intensity.

The PZT responds nonlinearly to the application of the driving voltage and an example of this is shown in figure 4.12. The removal of this nonlinearity is discussed in section 5.1.2.

4.3 Mode spacing

One advantage of the laser design shown in figure 4.5 is that the cavity length can be modified by changing the depth of the metal component holding the laser gain medium. Three example mode spacings are shown in figure 4.13. The mode spacing frequencies are

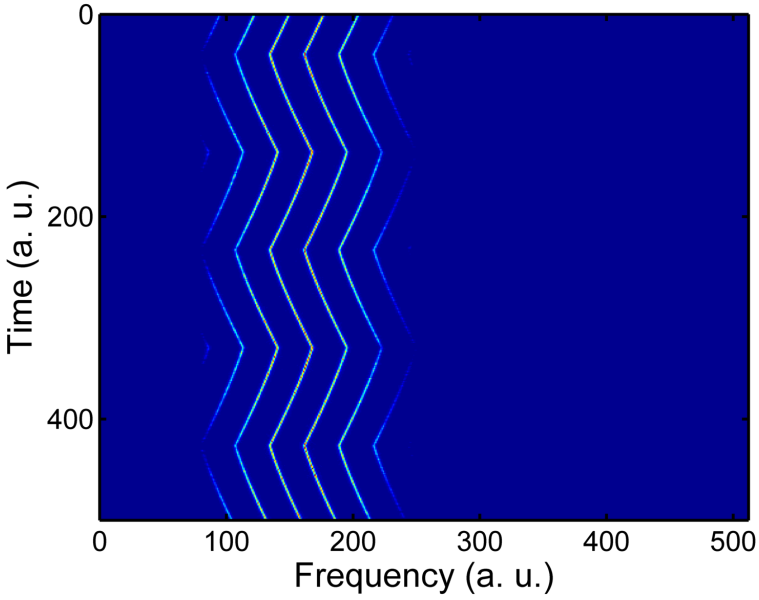

Figure 4.12: Time dependence of the mode frequencies during scanning measured using a CCD camera to record the spectrum on a 1 m spectrograph. The applied ramp is linear, however the laser modes respond with a slight curvature.

18.38 GHz, 28.80 GHz and 33.06 GHz. All of the examples cover a spectral region ∼200 GHz in size although their central wavelengths are slightly different. The shortest mode spacing is centred at 1565 nm whereas the other two are centred near 1570 nm

Optimal mode spacing

The optimal cavity length is dependent upon the species to be detected and the frequency of laser output. As discussed in chapter 3, there is a criterion for the mode spacing to be larger than the absorption molecular width of the detected species. But also, as discussed in the same chapter, the separation of adjacent absorption lines is approximately equal. This poses a problem whereby if the line spacing $\Delta\nu_{abs}$ is an integer multiple of the mode spacing,

$$\Delta\nu_{mode} = p\Delta\nu_{abs}, \tag{4.1}$$

then the individual absorption features will appear at the same place in the MUMAS fingerprint and only a single absorption dip will be seen. This is problematic because it produces ambiguities if the temperature is unknown as the contribution of each mode is unknown.

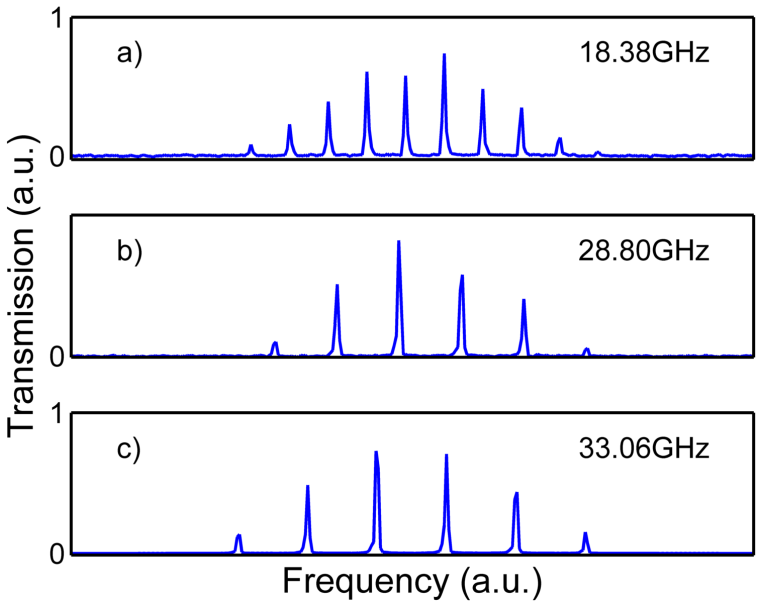

Figure 4.13: Three different examples of mode spacings achieved with different cavity lengths based on the versatile laser cavity design. Figure a) shows the shortest mode spacing which corresponds to an optical cavity length of 8.16 mm. Figures b) and c) of made spacing 28.80 GHz and 33.06 GHz correspond to 5.20 mm and 4.53 mm respectively.

Secondly, the robustness of any simulation fitting to this data is reduced because of the unknown contribution to the absorption signal from each laser mode.

The initial laser design fell foul of this problem and an example MUMAS trace is shown in figure 4.14. It can be seen that both the carbon monoxide absorption lines are contained within the same region of the fingerprint which was problematic for the fitting algorithm. By inserting a 600 µm shim into the cavity the mode spacing was reduced by 4.3 GHz and the new MUMAS fingerprint is shown in figure 4.15.

4.4 Final laser parameters

The fixed and final laser parameters are listed in table 4.2 along with the path length of the gas cell to be used which is equally a fixed parameter.

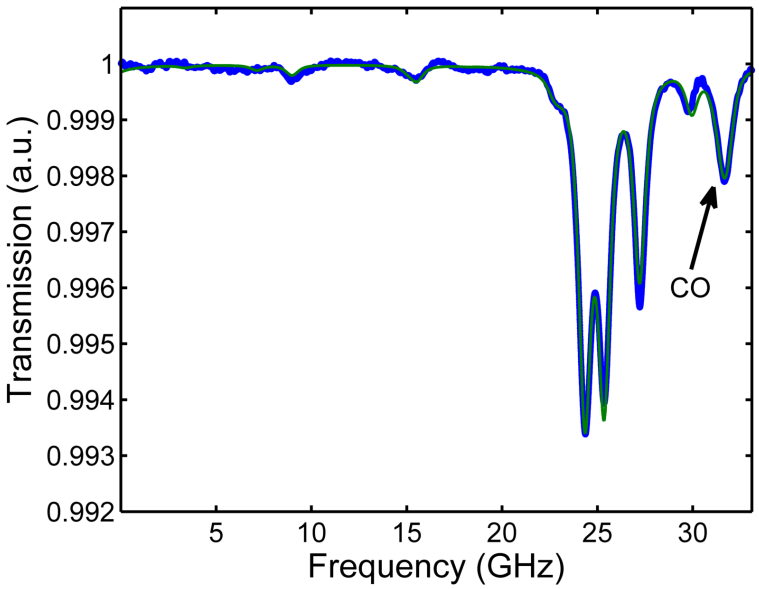

Figure 4.14: The MUMAS finger print with two carbon monoxide lines indicated as a single feature. Blue represents the data and green is the best fit simulation. It is also obvious that a large proportion of the MUMAS fingerprint does not contain absorption features. Whilst some baseline is desirable, this mode spacing is not an efficient use of the MUMAS spectrum available.

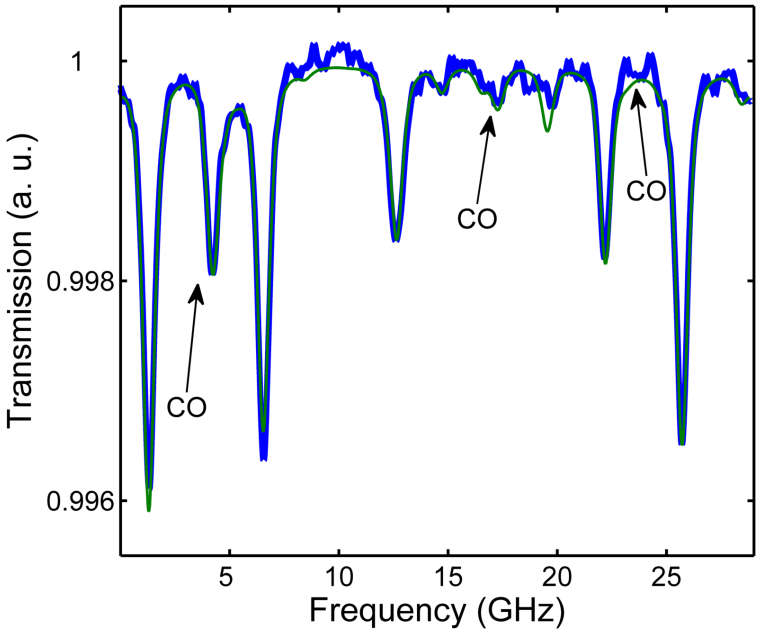

Figure 4.15: The MUMAS fingerprint with the three carbon monoxide lines indicated separately. Blue represents the data and green is the best fit simulation. The carbon monoxide line on the extreme right is labelled for completeness but is significantly weaker than the surrounding lines, as well as being dominated by a carbon dioxide line.

4.4.1 Initial experiment

With the laser parameters quantified, an experiment whereby the partial pressures of CO and CO_2 were to be determined was performed. A custom-order cylinder of gas supplied

variable	value
comb centre frequency ν_c	190 838.8 GHz
mode spacing $\Delta\nu_{space}$	28.8 GHz
mode line-width $\Delta\nu_{mode}$	8 MHz
FWHM of laser mode envelope $\Delta\nu_{FWHM}$	138 GHz
mode envelope threshold $\Delta\nu_{thresh}$	0.14
path length l	160 cm

Table 4.2: A list of the fixed experimental parameters that will be provided to the MUMAS modelling code, namely the laser characteristics and the path length.

by BOC designed to simulate typical (dry) exhaust gas was used, [111] hereby known as *calibration gas*. Its composition was as follows:

CO_2 14.02%

CO 3.52%

Hydrocarbons 1500 ppm

with the rest of the gas being composed of nitrogen.[3] The calibration gas was supplied to the gas cell in the setup described later in chapter 6. The total pressure of the calibration gas in the cell was 100.32 torr and it was allowed to settle to room temperature before data was recorded. A comprehensive guide to the experimental procedure and analysis can also be found in chapter 6 except that a baseline correction was not required for this experiment. A total of 100 spectra were recorded and the mean was calculated. The simulated MUMAS spectrum was fitted to the experimental data with the partial pressures of CO and CO_2 being the adjusted variables. This can be seen in figure 4.14. The fitting routine returned a CO/CO_2 ratio of 0.25191, which compared to the certified value of $0.25107 \pm 1.4\%$. The difference between the two values represents a 0.33% discrepancy from the certified value. The first demonstration of MUMAS in simultaneously determining the partial pressures of CO and CO_2 returned a ratio value that was within the stated error of the calibration gas being measured.

[3] As this experiment was carried out at room temperature, water vapour transitions are heavily suppressed and do not interfere with the absorption profile - therefore water vapour is not required in the calibration gas.

4.5 Summary and conclusions

The spectral overlap of carbon monoxide and carbon dioxide has been identified. A suitable design for a solid state Er^{3+}:Yb^{3+} phosphate glass laser has been proposed and built. The cavity design has been chosen to be planar/concave with the back face of the erbium glass wedge to be the exit coupler of the laser. This two-piece monolithic design was able to scan smoothly and is robust to misalignment. A custom edge coating from Layertec was used to manipulate the gain medium to operate at the desired frequency of 1571 nm, but even with the reduction in net round trip gain caused by this choice in reflectivity an output of $\sim$30 mW was achieved.

The high surface quality of the glass used to form the laser cavity allowed a narrow laser linewidth to be produced, which is substantially smaller than the absorption width of any of the typical features this laser would measure. The PZT, although advertised to be able to scan at much higher frequencies (up to 50 Hz for full MUMAS scan), performed poorly at frequencies higher than 10 Hz, so scanning was kept to a low rate to avoid this problem.

The idea of an optimal mode spacing was mentioned which points to the undesired situation of having a mode spacing which is an integer multiple of the absorption line spacing. Having experienced this with the first working design, an alteration by changing the cavity length was carried out and the results showed that the cavity length could be easily manipulated to give the desired MUMAS fingerprint. An initial experiment was also performed which demonstrated the ability of MUMAS to determine the ratio of CO and CO_2 from a certified mixture to be within the manufacturers stated precision.

Chapter 5

Data analysis and MUMAS simulation

The method of data capture and processing is described. The captured data is linearized using a reference spectrum from a a Fabry-Pérot interferometer, and software filtered to remove any residual high frequency noise that is left after division away of the background. The modelling code of the MUMAS simulation is described, as well as the fitting algorithm used to match the simulation to the processed data. Finally, a method for using a nonlinear least squares fitting algorithm is discussed that can find global minima within the designated variable space, provided certain conditions are met.

This chapter discusses how the data is captured, processed, analysed, and the type of fitting algorithms used in matching the simulation to the data. The simulation code is discussed in detail and there is an introduction to nonlinear fitting techniques, touching on their advantages and disadvantages.

A summary of the processes involved in data analysis, MUMAS simulation and the optimisation of fitting variables is shown as a flow chart in figure 5.1, where each stage is elaborated on later in the chapter.

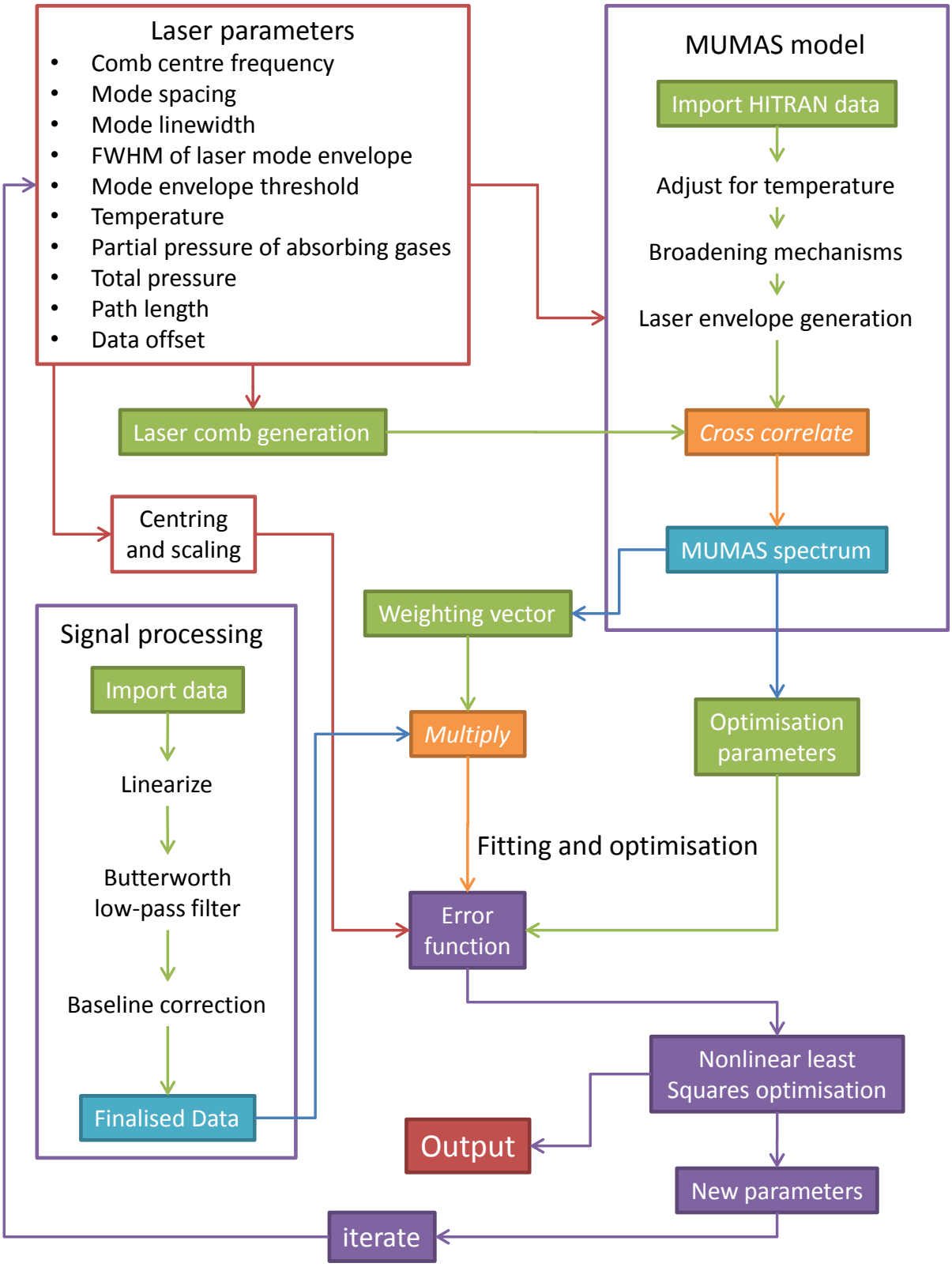

Figure 5.1: A flow chart summarizing the processes involved in data analysis, simulation of the MUMAS spectrum, and the optimization of simulation variables.

5.1 Signal processing

This section explains the processes by which the data were manipulated into a suitable form such that the analysis described in chapter 6 can be applied. The raw data were processed to remove high frequency noise, convert the time axis into a frequency axis (linearized), and remove power fluctuations.

5.1.1 Detector bandwidth

The laser intensity is detected by an InGaAs biased detector from Thorlabs - DET10C model - which generates an output photocurrent I_{out} when radiation between 800 µm to 1700 µm is incident upon the detector surface. This photocurrent is driven through a terminating, or load resistance, R_L, generating a voltage V_L, which is read and stored on a computer by an oscilloscope. The generated voltage, photocurrent and load resistance are related through

$$V_L = I_{out} \times R_L, \tag{5.1}$$

where the generated voltage must be less than the bias voltage of the detector. If V_L is greater than the reverse bias voltage then the detector is said to be saturated [112].

The detector bandwidth f_{BW} is a measure of the response in the frequency domain. A typical definition of the detector bandwidth is the frequency at which the electrical power spectrum drops to 50% of its value at DC. This places an upper limit on what frequencies can be confidently recorded by the oscilloscope and the value is dependent upon the load resistance and the diode capacitance C_j as described by the following equation [112]:

$$f_{BW} = \frac{1}{2\pi R_L C_j}. \tag{5.2}$$

The laser intensity incident on the detector is approximately 0.8 mW which easily causes saturation of the generated voltage V_L when the load resistance of the oscilloscope is used.

The linear response of the voltage V_L to the photocurrent I_{out} means that by lowering the load resistance, saturation of the detector can be avoided. The termination load R_L is therefore reduced by placing a 10 kΩ resistor in parallel to the 1 MΩ internal resistance of the oscilloscope. The voltage induced on this lower load resistance is now below the voltage bias limit thus avoiding detector saturation.

However, the detector bandwidth has been altered from 2.7 kHz ($R_L = 1\,\text{M}\Omega$, $C_j = 40\,\text{pF}$) to 270 kHz ($R_L = 10\,\text{k}\Omega$, $C_j = 40\,\text{pF}$). This increased bandwidth results in a significant noise increase on the detected signal and far exceeds the minimum bandwidth which is of the order 1 kHz[1]. To restore the detector bandwidth to a more sensible value, extra capacitance is place in series with the diode capacitance C_j. The inserted capacitance was 5150 pF which resulted in a bandwidth of just over 3 kHz. A bandwidth of 3 kHz is sufficient for the detection of MUMAS spectra at 2 Hz and is within the operating limitations of the detector used.

The final bandwidth of the system is comparable to the original value before the load resistance or capacitance were changed, thus ensuring that the detector will be operating within intended parameters.

The data are collected and stored in a `.mat` format on the computer hard disk for further analysis in MATLAB at a later time.

5.1.2 Linearization

The measurement recorded by the oscilloscope is in the time domain and the PZT does not respond in a linear fashion to the applied triangular ramp. This means that the detected MUMAS signal needs to be translated from a function of time to a function of frequency, by use of a calibration of the time scale in terms of frequency. This is done by use of a spectrum analyser, Thorlabs SA200-12B, which has a free spectral range of 1.5 GHz and a finesse of 494. The spectrum analyser is a Fabry-Perot etalon. As such, it has a continuous spectrum

[1]The MUMAS spectrum is collected at a frequency of 2 Hz and by measuring the rise time of a single peak, the required bandwidth can be estimated.

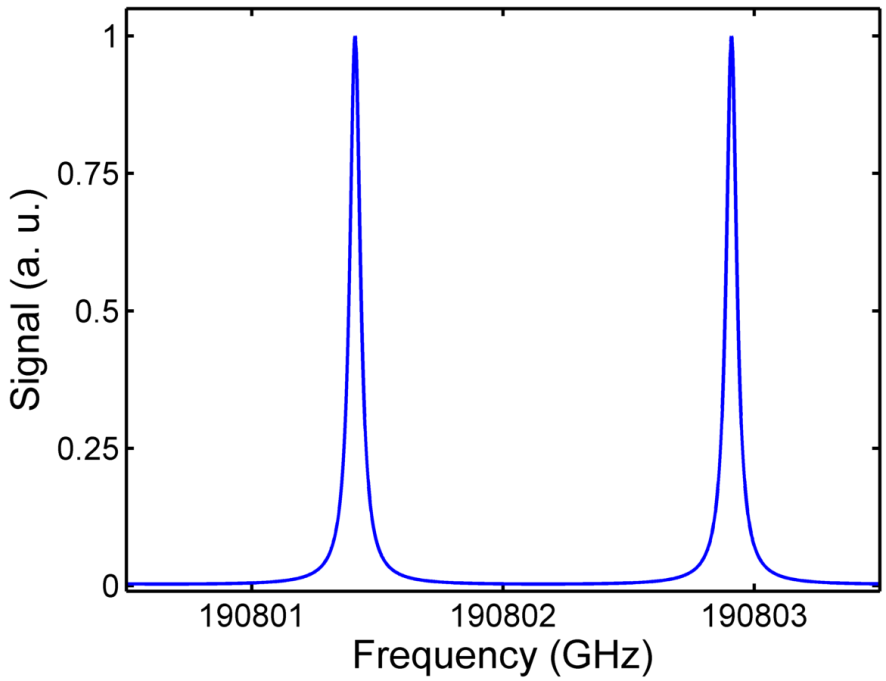

Figure 5.2: Transmission of a Fabry-Perot etalon with a free spectral range of 1.5 GHz between the two peaks. The finesse has been artificially reduced for clarity, as the fringes would be delta-like on this scale. The resolution of the Thorlabs Fabry-Perot etalon is 7.5 MHz.

of transmission modes, described by the Airy function

$$T = \frac{1}{1 + \Phi \sin \delta/2}, \tag{5.3}$$

where T is the transmittance function, Φ is the coefficient of finesse and is given by $\Phi = \frac{4R}{(1-R)^2}$, and $\delta = \frac{2\pi}{\lambda} 2nl \cos\theta$. R is the reflectance of each mirror surface in the etalon, assumed to be equal. The scanned laser modes are coupled into the cavity only when their frequency matches the boundary conditions of the etalon. This results in each mode being transmitted every time their frequency matches this condition in a repetitive pattern which has a FSR of 1.5 GHz. The transmission is given by a cross-correlation of the etalon Airy function (figure 5.2) and the laser mode function (figure 4.13), and is displayed in figure 5.3.

By selecting the peak of any repeated mode throughout the etalon transmission profile, a vector of points in time representing an equal spacing in frequency can be built up.

Through fitting a high-order polynomial through the locations of the selected peaks, a unique function is established which maps the progression in time of the measurement, to

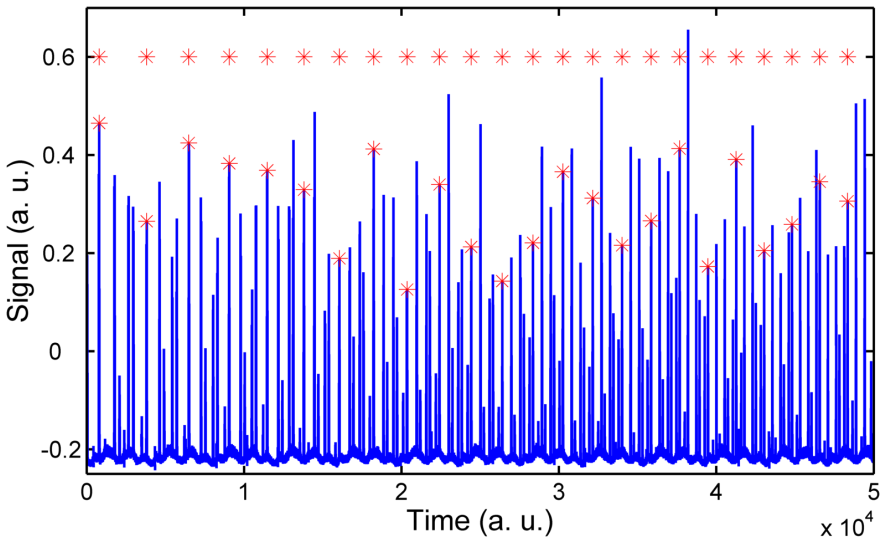

Figure 5.3: Transmission of a Fabry-Perot etalon with a free spectral range of 1.5 GHz over the distance of one mode spacing $\Delta\nu_{mode}$ when the laser is scanning. The repeating mode has been highlighted with a red asterisk, with the top row of red asterisks showing the nonlinearity of the PZT. The polynomial is fitted to this vector.

the frequency scanned by the modes.

5.1.3 Software filtering

After each detector measurement has been linearized, the signal transmitted by the gas cell is divided by the signal from the reference detector in order to eliminate any common fluctuations in output power. This often left a residual high frequency noise caused by the incomplete division of two lower frequency noises.

The linearized data was then subjected to a low-pass software filter using an infinite impulse response (IIR) Butterworth algorithm to generate the required coefficients. A Butterworth filter is low-pass response with a sloped cut-off but importantly has an equal response coefficient to all frequencies that it allows through - effectively a true step function. An example of a Butterworth filter response is shown in figure 5.4. This further removes any residual frequency noise left from the hardware low-pass filter and also compensates for any optical interference within the signal. Optical paths that encounter windows or reflective surfaces can result in interference from etalon fringes, caused by the reflection from two parallel surfaces which produces a wavelength dependent transmission. If the etalon fringes are

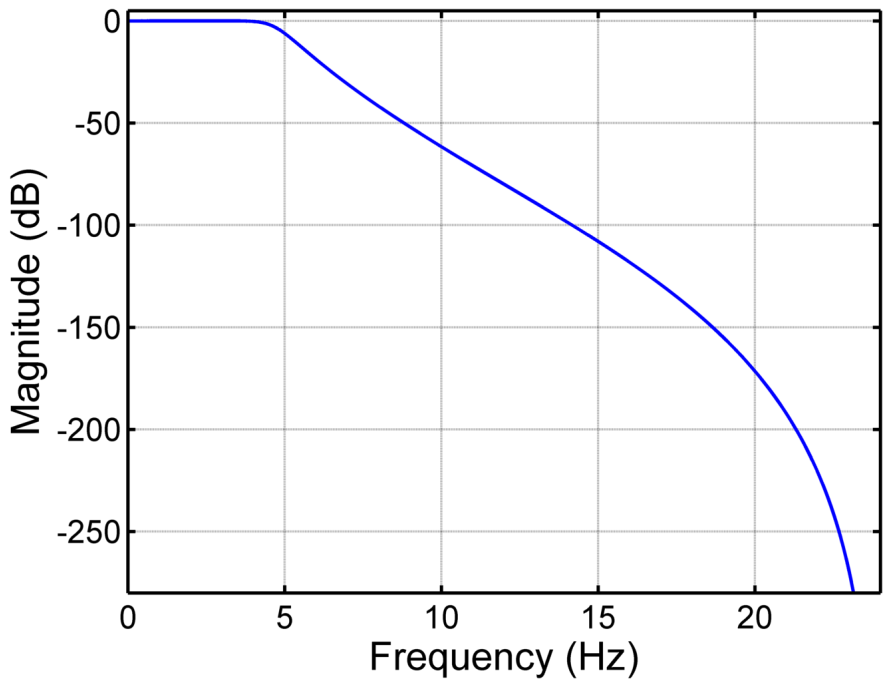

Figure 5.4: Frequency response of a Butterworth low-pass filter. The accepted frequencies all have the same weighting, and anything higher is suppressed in a logarithmic manner.

static in the MUMAS spectrum, then they can be eliminated by dividing the signal by the reference signal that contains the same etalon interference structure, however should their relative phase alter then the fringes will be amplified by the normalization process. This filter aims to reduce this effect and produce very reliable data with an improved signal to noise ratio.

5.2 Modelling the MUMAS signal

The simulated MUMAS spectrum is calculated directly using a theoretical model in MATLAB. There are two main parts to the coding: modelling the laser behaviour, and modelling the spectral response of the gas. These two predictions are then cross-correlated with each other to produce the required MUMAS fingerprint. Due to the very high resolution of the laser modes ($\sim$8 MHz), this process can be computationally and memory intensive. To reduce the computational expense approximations have been made where possible to reduce computation time and memory usage. Nevertheless, the simulation code has been worked into an efficient format which allows it to be effectively used as part of a fitting routine

which requires a new MUMAS spectrum to be calculated on each iteration as the algorithm determines the optimal parameters.

5.2.1 Simulation

The simulation code has to be provided with the variables shown in table 5.1. The first five

symbol	variable name
ν_c	comb centre frequency
$\Delta\nu_{space}$	mode spacing
$\Delta\nu_{mode}$	mode line-width
$\Delta\nu_{FWHM}$	FWHM of laser mode envelope
$\Delta\nu_{thresh}$	mode envelope threshold
T	gas temperature
P_i	partial pressure of constituent absorber i
P_T	total pressure
l	path length

Table 5.1: A list of variables that is fed into the simulation code which produces the desired MUMAS spectrum.

variables in table 5.1 are laser parameters, whilst the next three are specific to the sample gas. The final variable, path length l, is particular to the chosen setup.

Import spectral data

The first step in the modelling process is to import the relevant absorption transitions from the HITRAN 2008 database [103]. In some circumstances the HITEMP 2010 database [113] may be used instead.[2] `hitran_in.m` requires the input of ν_c and $\Delta\nu_{FWHM}$. $\Delta\nu_{FWHM}$ is used only as a guide as to how large the section extracted from the database should be. Details of the types of data contained within the HITRAN database are available in the literature. All spectral lines above a predetermined cut-off strength are imported in the frequency interval $\nu_c - 2.5 \times \Delta\nu_{FWHM} \rightarrow \nu_c + 2.5 \times \Delta\nu_{FWHM}$.

[2]The HITEMP 2010 database is specifically designed for combustion spectroscopy. This database contains many extra hot bands which only become significant to spectroscopy at considerably higher temperatures than the reference temperature of 296 K.

Adjust for temperature

Secondly, `hitran_temp.m` recalculates the transition strengths from their reference 296 K temperature to the input temperature T.

The strength of the transition ν_0 is dependent on the electronic dipole, relative populations of the initial and final state, and the density of states. This value is temperature dependent which presents a problem when trying to calculate such a complex variable. Many of the terms in equation 3.19 are independent of temperature, so these are all incorporated in the line intensity constant S_{ij}. The HITRAN 2008 [103] database contains the line intensity of many transitions at a reference temperature of 296 K, as well as self- and air-broadening parameters. By using this reference value and the temperature dependent term of equation 3.19, the line intensity at any temperature T, $S_{ij}(T)$, can be derived as follows [113]

$$S_{ij}(T) = S_{ij}(T_{ref})\frac{Q(T_{ref})}{Q(T)}\frac{\exp(-\frac{E_i}{k_B T})}{\exp(-\frac{E_i}{k_B T_{ref}})}\frac{\left[1-\exp(-\frac{hc\nu_{ij}}{k_B T})\right]}{\left[1-\exp(-\frac{hc\nu_{ij}}{k_B T_{ref}})\right]}. \tag{5.4}$$

The HITRAN database comes with a pre-calculated matrix which contains the partition sum for all of the isotopic species for a range of temperatures. Thus the new value was merely looked up in the data array. The density of states was calculated using the energy of the transition.

Hot bands

Almost all transitions at room temperature will have the initial state being the ground state. However, transitions are possible whereby the initial state is not the ground state, for example, a transition between two excited vibrational states. Normally, the initial populations of these states means that they are heavily suppressed and their line strengths are often excluded from molecular databases such as HITRAN. These databases are of substantial size and to include all hot band transitions as well would make them unwieldy.

In certain situations, such as combustion, the temperature of detectable gases can be high

enough that such states are substantially populated, thus the hot band transitions become significant. Their inclusion in theoretical databases is therefore needed if a true spectroscopic fingerprint is to be achieved. One such database which includes the hot band transitions is known as HITEMP [113], and includes thousands of extra lines for 5 combustion-relevant gases.[3] Temperatures need to be above ∼500 K for hot bands to start becoming significant.

Spectral broadening

The next step is take into account any broadening mechanisms that may be affecting the transitions or absorption lines. As both homogeneous and inhomogeneous mechanisms are operating a Voigt line profile is used, as discussed in section 3.15. `hitran_broad.m` generates area-normalized Voigt profiles and multiplies them by the relevant transition strength taken from the database. The Voigt line shape is computed using a numerical approximation taken from Abrarov et al [114]. `hitran_broad` uses the partial pressures of the absorbing gases P_i, the total pressure P_T, the temperature T and the path length l to calculate the expected broadening for each transition. The final step involves summing the contributions of all transitions in preparation for combining it with the modelled laser modes.

It should be noted that the HITRAN or HITEMP databases contain pressure broadening coefficients for two possible scenarios, which are:

1. Self-broadening, and

2. Air broadening.

Specific foreign gas broadening (such as water vapour on carbon dioxide) is not covered, however the foreign species having the highest concentration in the gases to be analysed will be nitrogen, which can be approximated as air. All other major contributors are either diatomic or triatomic in structure, so as a good approximation, all foreign gas broadening mechanisms will be treated as air-broadened in the simulation. [115, 116]

[3] Namely CO, CO_2, H_2O, NO, and OH.

Laser comb generation

`comb_gen` produces a sparse matrix that contains the laser modes for use in the simulation. A sparse matrix is used because it is an efficient way of storing data where most of the entries are zero. As the laser mode width is approximately 10,000 times narrower than the mode spacing, and each mode requires 10 points above the FWHM to be well defined, this leads to a data array which is too large to use in the simulation code. Thus a sparse matrix is used to eliminate the need to store all of those zeros. An example is shown in figure 5.5.

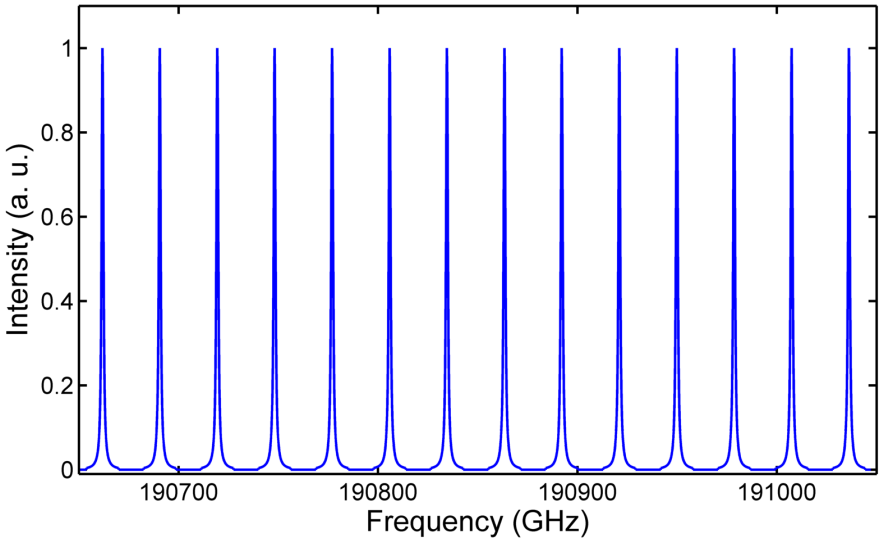

Figure 5.5: A generated laser comb with the line width largely exaggerated for visual effect. The modes are all of equal height, equally spaced, and are modelled by a Lorentzian function.

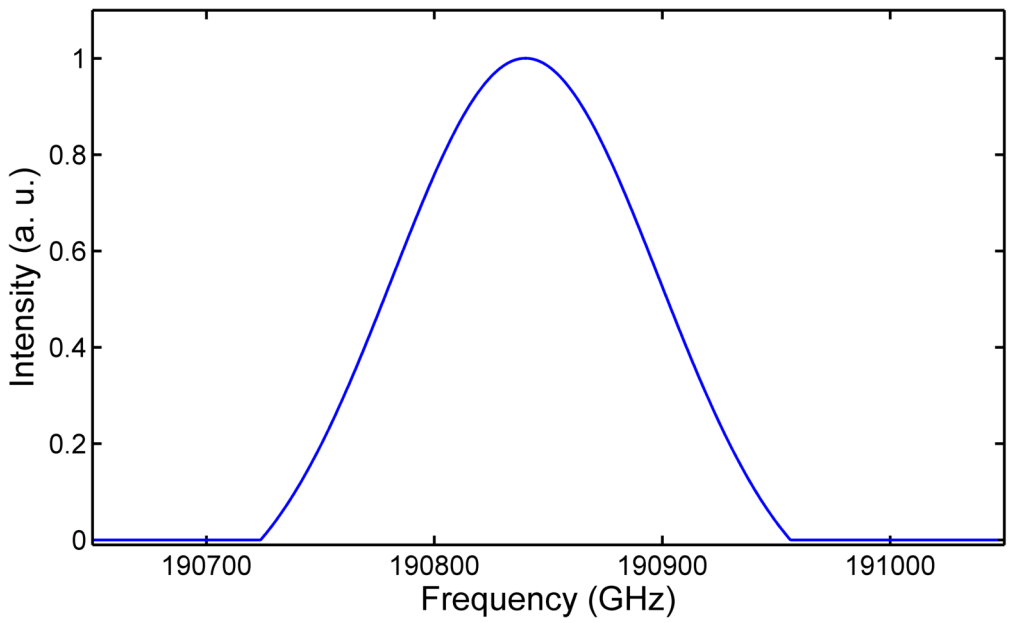

Figure 5.6: Empirical envelope function to describe laser mode intensity. One way of finding this function is to fit a simulation to a known gas sample with the two envelope parameters as fitting variables. Alternatively, the output spectrum from the Bristol Instruments wavemeter could be used, as shown in figure 4.8, to fit the envelope to the peak-height points of the static laser modes.

The laser modes are equally spaced by $\Delta\nu_s$ and have a line width $\Delta\nu_m$. The line profile is based upon a Lorentzian model, however because their line width (typically ∼MHz) is substantially smaller than the broadening of the spectral line (typically ∼GHz) then the exact functional form is not crucial. A Lorentzian curve is placed at $\Delta\nu_s$ intervals over the frequency range $\nu_c - 2.5 \times \Delta\nu_{FWHM} \rightarrow \nu_c + 2.5 \times \Delta\nu_{FWHM}$.

The laser comb is then multiplied by the envelope function which describes the relative intensities of the modes. An example of the envelope function is given in figure 5.6 and is calculated as follows.

The laser envelope is empirically modelled on a renormalized truncated Gaussian function. The envelope generation requires ν_c, $\Delta\nu_{FWHM}$ and $\Delta\nu_{thresh}$. It is calculated in the following manner. Firstly, the FWHM and ν_c is used to generate a unit-peak Gaussian curve G centred at ν_c

$$G = \exp\left(-\frac{(\nu - \nu_c)^2}{2\sigma^2}\right), \tag{5.5}$$

where $\sigma = \frac{\Delta\nu_{FWHM}}{2\sqrt{2\ln 2}}$. Next, the Gaussian curve is displaced vertically by $\Delta\nu_{thresh}$ such that

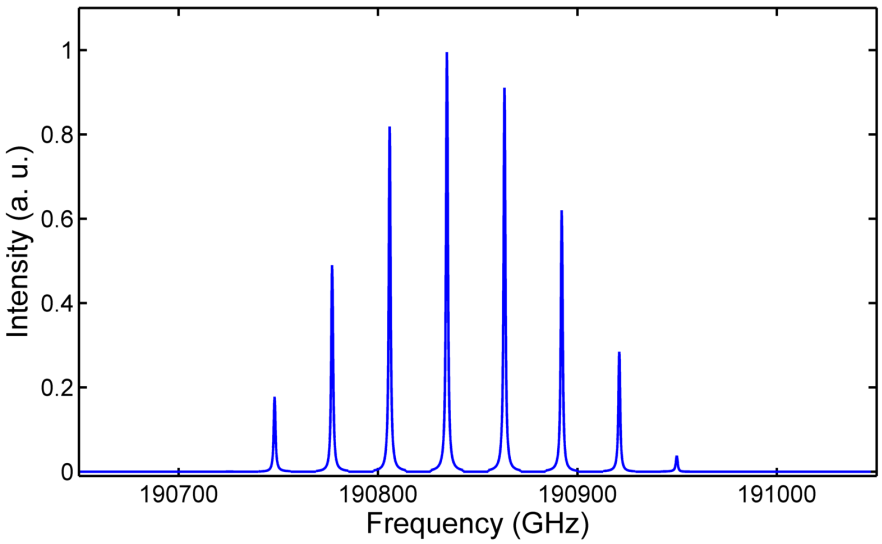

Figure 5.7: Figure showing the final modelled laser comb used in the MUMAS simulation. The mode intensity follows the envelope pattern during scanning of the laser.

$G' = G - \Delta\nu_{thresh}$, where $\Delta\nu_{thresh}$ is between 0 and 1. Any numerical value that is less than zero is forced to equal zero, and finally the envelope function is normalized to unit height. An example of the final simulated laser modes is given in figure 5.7.

Retrieval of MUMAS spectra

The MUMAS spectrum is then created by multiplying the predicted gas transmission profile produced using `hitran_broad` by the modelled laser comb at each point during which the laser modes are effectively scanned one mode spacing. In previous work[12, 13, 14] this was performed by creating a meshgrid of the laser modes. A meshgrid is a 2D matrix where each row represents the laser modes at an instant in time and progression down the rows represents the time axis. Thus the laser comb was element-wise multiplied by the gas transmission profile and each row summed to give a total transmission. The resulting vector is the MUMAS spectrum and to get higher resolution required a larger meshgrid. This was very memory intensive and it was not possible to implement the final calculation this way.

By using a cross-correlation and selecting out the relevant section of the outcome, the MUMAS spectrum could be created without running into memory issues. A cross-correlation of two discrete functions f and g is similar to a convolution and is represented mathematically

as

$$(f \star g)[n] = \sum_{m=-\infty}^{\infty} f^*[m]\, g[n+m]\,. \tag{5.6}$$

In the code, by multiplying the broadened gas transmission profiles by the laser envelope functions (f) and cross-correlating it with the comb of laser mode from `comb_gen` (g), and by selecting the right part of the resulting vector, the MUMAS spectrum is generated in high resolution in a very efficient manner, without the memory issues of the previous method.

The simulated MUMAS spectrum was then copied and added onto the end of the vector, thus giving a MUMAS spectrum which was repeated once. This step is done to avoid the need to know the precise starting point of the MUMAS spectrum relative to the data. The data is then cross-correlated across the repeated MUMAS spectrum which causes the location of the data within the simulation to be readily identified.

These steps are then repeated in tandem with a fitting algorithm which then finds the optimum parameters of the variables given to it.

5.3 Fitting the model to the data

With the generation of the MUMAS spectrum simulation, an algorithm or method is needed to optimize some or all of the input parameters such that the simulated spectrum matches the data. A nonlinear least squares algorithm built into MATLAB is used for this purpose. The algorithm must be provided with initial parameters as well as lower and upper bounds. Through use of centring and rescaling of these variables the error function can converge onto a minimum value which returns the optimum parameters for the data supplied.

5.3.1 Least squares vector

The reduction in the total least squares value requires that a residual vector be generated, which is the difference between the data and simulation at a given point, and is represented

by

$$r_t(\vec{x}) = M_t(\vec{x}) - d_t, \tag{5.7}$$

where $\vec{x} = [x_1, x_2 \dots x_n]$ denotes the variable parameters to be optimsied, to which the residual depends, t represents the indices over which the simulation and data are calculated, $M_t(\vec{x})$ is the MUMAS simulation, and d_t is the data. t runs over the length of the simulation and is represented by $[1, 2, 3, \dots m]$.

The general aim of the least squares is to minimize the following sum

$$\sum_{t=1}^{m} r_t^2(\vec{x}) = ||r(\vec{x})||^2, \tag{5.8}$$

where

$$r_t(\vec{x}) = \begin{bmatrix} r_1(x_1, x_2 \dots x_n) \\ r_2(x_1, x_2 \dots x_n) \\ \vdots \\ r_m(x_1, x_2 \dots x_n) \end{bmatrix} \tag{5.9}$$

is a set of m residuals over the index t with n different variables to optimse. In general, this sum can have global or local minima and the algorithm used to carry out this minimization process must be chosen carefully. The best algorithm choice will depend on how many parameters n are being optimized, the size of the space over which the calculation is being carried out, and how strong the nonlinearity is between the n variables.

Weighting

The least squares sum in equation 5.8 equally weights each index (data point) t, so every residual $r_t(\vec{x})$ has an equal effect on the final sum. To utilize better the data being processed, a suitable weighting factor can be applied to each residual before it is summed, thereby certain indices of t, subset t_s, will have a stronger affect on the computed error value which is fed back into the algorithm. The weight vector will be predetermined and will be of length m. A typical example is those data points which have a high signal-to-ratio have a stronger

weighting than those data points which exist near the noise limit.

5.3.2 Nonlinear least squares

Reducing the sum of residual squares or minimisation of a nonlinear problem can be solved using Newton's method which utilizes the first and second derivatives. It is therefore a necessary constraint that the function to be minimized has well-behaved first and second derivatives. The first and second order derivatives are represented by

$$\begin{aligned}\frac{\partial ||r(\vec{x})||^2}{\partial x_i} &= 2\sum_t^m r_t(\vec{x})\frac{\partial r_t(\vec{x})}{\partial x_i} \\ &= 2\sum_t^m r_t(\vec{x})\nabla r_t(\vec{x})\end{aligned} \tag{5.10}$$

and

$$\begin{aligned}\frac{\partial^2 ||r(\vec{x})||^2}{\partial x_i \partial x_j} &= 2\sum_t^m \left(\frac{\partial r_t(\vec{x})}{\partial x_i}\frac{\partial r_t(\vec{x})}{\partial x_j} + r_t(\vec{x})\frac{\partial^2 r_t(\vec{x})}{\partial x_i \partial x_j}\right) \\ &= 2\sum_t^m \left(\nabla r_t(\vec{x})\nabla r_t(\vec{x})^T + r_t(\vec{x})\nabla^2 r_t(\vec{x})\right)\end{aligned} \tag{5.11}$$

respectively. Here, ∇ is the differential gradient operator of the n variables and is represented by

$$\nabla = \left[\frac{\partial}{\partial x_1}, \frac{\partial}{\partial x_2}, \ldots \frac{\partial}{\partial x_n}\right]. \tag{5.12}$$

Newton's method

Newton's method is an iterative process for minimising a general 1D function f with a single real variable x. If f has a local extremum at x^* and is differentiable, it therefore follows that the first derivative of f must vanish at that point, i.e. [117]

$$f'(x) = 0. \tag{5.13}$$

To distinguish minima amongst the extrema found in f, the second derivative f'' is also needed.

In general this problem cannot be solved analytically, so an iterative process that generates a sequence of points $\left\{x^k\right\}$ and derivative values $\left\{f'\left(x^k\right)\right\}$ such that the latter sequence converges to zero is needed. Newton's method achieves this by using a guess x^k as the solution to equation 5.13, linearize f' around x^k, and solve for the point where the linear function vanishes, which is labeled x^{k+1}. This point is then used as the next guess. The equation that is being solved is given by

$$f'\left(x^k\right) + f''\left(x^k\right)\left(x - x^k\right) = 0, \tag{5.14}$$

and the solution is

$$x^{k+1} = x^k - \frac{f'\left(x^k\right)}{f''\left(x^k\right)}. \tag{5.15}$$

Extension to multiple variables

This method can be extended to a multiple variable problem where $\vec{x}$ contains n parameters to be optimized. The equation to be solved now becomes

$$\nabla f\left(x^*\right) = 0. \tag{5.16}$$

The real valued function f must be twice differentiable for Newton's method to apply. In addition to the gradient ∇f, the $n \times n$ Hessian matrix $\nabla^2 f$ (equation 5.11 but in 3 dimensions) is also required at every point. Just as before, ∇f is linearized about the guess x^k and then set the linear functions to zero. The final solution of x^{k+1} is given by

$$x^{k+1} = x^k - \frac{\nabla f\left(x^k\right)}{\nabla^2 f\left(x^k\right)}. \tag{5.17}$$

The Hessian matrix must be nonsingular for this equation to be solved.

For this equation to be solved, both the gradient and Hessian matrices have to be evalu-

ated at each index t, which, if done in full, can be a very computationally intensive process. For most algorithms, the Hessian matrix is approximated to increase computational speed, but that will not be discussed here.

Another way of looking at Newton's method is that it approximates the function f using a quadratic Taylor expansion about the guess point x^k. Finding the next guess of x^{k+1} is done by minimising this approximation.

Equations 5.10 and 5.11 contain the gradient $\nabla r_t(\vec{x})$ and Hessian matrix $\nabla^2 r_t(\vec{x})$. These can be explicitly written as

$$\nabla r_t(\vec{x}) = \begin{bmatrix} \frac{\partial r_1}{\partial x_1} & \frac{\partial r_1}{\partial x_2} & \cdots & \frac{\partial r_1}{\partial x_n} \\ \frac{\partial r_2}{\partial x_1} & \frac{\partial r_2}{\partial x_2} & \cdots & \frac{\partial r_2}{\partial x_n} \\ \vdots & \vdots & \ddots & \vdots \\ \frac{\partial r_m}{\partial x_1} & \frac{\partial r_m}{\partial x_2} & \cdots & \frac{\partial r_m}{\partial x_n} \end{bmatrix} \tag{5.18}$$

and

$$\nabla^2 r_t(\vec{x}) = \begin{bmatrix} \frac{\partial^2 r_t}{\partial x_1^2} & \frac{\partial^2 r_t}{\partial x_1 \partial x_2} & \cdots & \frac{\partial^2 r_t}{\partial x_1 \partial x_n} \\ \frac{\partial^2 r_t}{\partial x_2 \partial x_1} & \frac{\partial^2 r_t}{\partial x_2^2} & \cdots & \frac{\partial^2 r_t}{\partial x_2 \partial x_n} \\ \vdots & \vdots & \ddots & \vdots \\ \frac{\partial^2 r_t}{\partial x_n \partial x_1} & \frac{\partial^2 r_t}{\partial x_n \partial x_2} & \cdots & \frac{\partial^2 r_t}{\partial x_n^2} \end{bmatrix}. \tag{5.19}$$

In the gradient matrix each row indicates how each residual point varies with each fitting parameter, whilst each column represents how that residual point t varies across the spectrum. The gradient vector has $[m \times n]$ elements.

The Hessian matrix is square and contains second order partial derivatives and is an indicator of how the variables relate to one another. The off-diagonal elements indicate how non-orthonormal the variables are in the function f, and the more orthogonal the elements of $\vec{x}$ are, the easier it is for the fitting algorithm. The Hessian matrix has $[n \times n]$ elements. As such, if this matrix is to be computed in full, a computer will have to undertake $\left[m^2 \times n^3\right]$ calculations compared to $[m \times n]$ calculations for the gradient vector. The MATLAB code

approximates the Hessian matrix by using the method of finite differences.

5.3.3 Application to MUMAS model

Along with the MUMAS parameters listed in table 5.1, a vertical offset is also included. As mentioned in section 5.3, the orthogonality of the variables being passed to the nonlinear least squares fitting algorithm can have a strong impact on how successful the search for a global minimum is, assuming there is one to find. Some variables are relatively nonorthogonal, with some examples being (pressure and temperature), and (FWHM of laser mode envelope and mode envelope threshold). Another disadvantage of the the minimisation technique is the possibility of being stuck in a local minima, or being unable to differentiate between the global minimum and surrounding local minima.

One way to circumvent this is to do exhaustive searches of the variable space - i.e. computing the square residual of each possibility of the input variables. This may be a very expensive and time consuming way to find the optimum solution, but it can give a much clearer picture of how the over-riding function f behaves according to the input variables.

It was found that once the laser parameters were determined, and the temperature and total pressure fixed, then the partial pressures of the constituents gases could be readily determined using a nonlinear least squares search algorithm, as they are largely orthogonal.

The laser parameters were found by use of a combination of methods. The output from the Bristol Instruments spectrum analyser gave an indication of centre frequency, mode spacing, FWHM of laser mode envelope, and mode envelope threshold. To determine them more accurately exhaustive searches were made using data taken utilizing gas mixtures of known composition and temperature. The use of an expensive wavemeter is therefore not essential for the MUMAS technique as the required parameters can be found using a calibration gas. By constraining the variables between upper and lower bounds, known false minima can be excluded from the operational space over which the algorithm is working. This also highlights the importance of choosing sensible starting values for the fit. Some examples

of the exhaustive search are shown in figures 5.8, 5.9 and 5.10. Figure 5.8 shows how local minima could hinder the minimisation process, figure 5.9 demonstrates how the FWHM of laser mode envelope and mode envelope threshold are nonorthogonal, and figure 5.10 demonstrates that the partial pressures of the constituent gases are orthogonal.

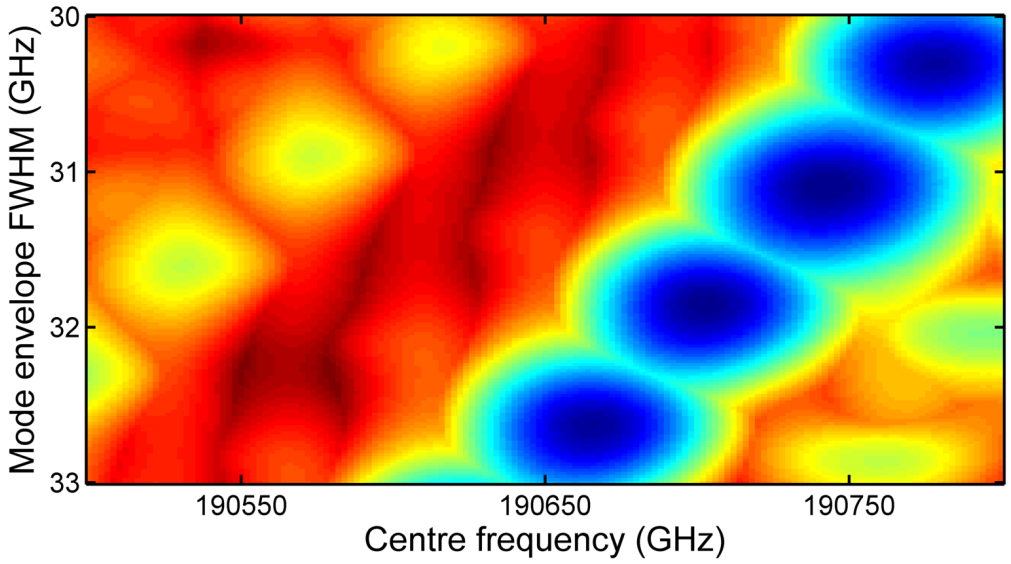

Figure 5.8: An example of the global numerical space covered by the 2 variables shown on the axes. The blue/black regions show where the sum of the square of the residuals is lowest, and it can be clearly seen that there are multiple local minima. By using approximations to these variables from other means such as the Bristol Instruments spectrum analyser, lower and upper bounds on the centre frequency and mode envelope FWHM are supplied, which restricts the computational space of the algorithm.

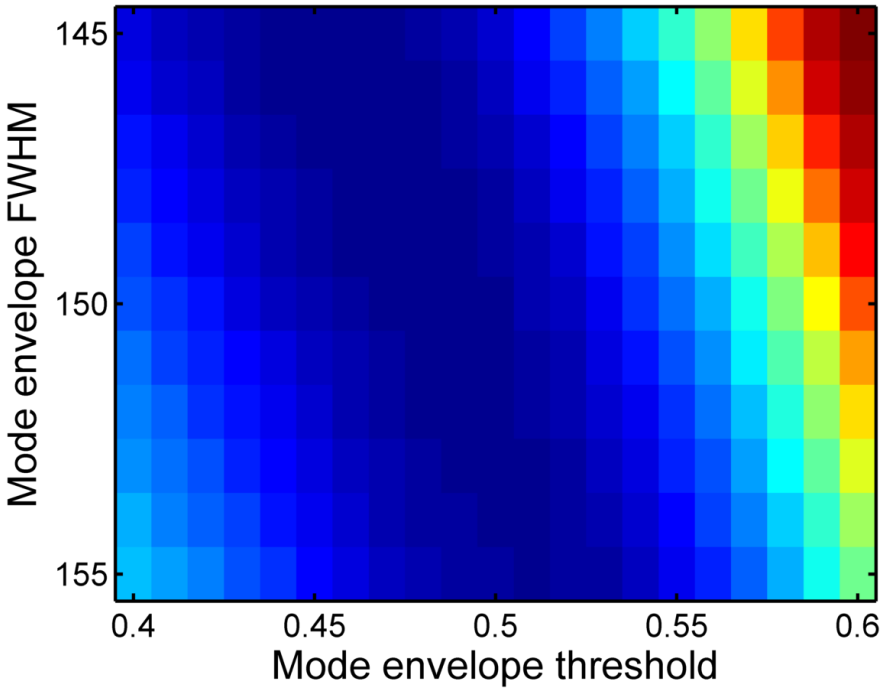

Figure 5.9: An example of two nonorthogonal variables which would be very difficult to optimize. Fitting data from different gas mixtures allowed these laser parameters to be fixed. Blue shows the best-fit area.

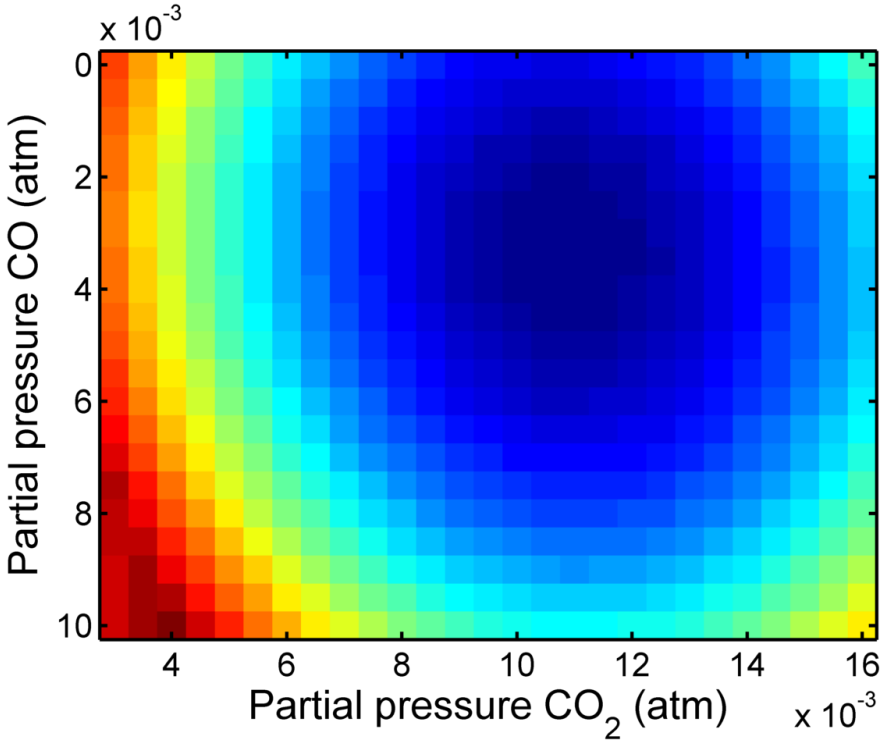

Figure 5.10: This figure shows that the partial pressure of constituent gases are orthogonal variables, as demonstrated by the circular pattern. This shows that a nonlinear least squares fitting routine will have a high probability of successfully minimising the function. Blue shows the best-fit area.

Algorithm

The algorithm used in the fitting routine is the `lsqnonlin` routine that is regularly installed in MATLAB. This algorithm utilizes a nonlinear least squares approach using a Newton-style method similar to that described in section 5.3.2. The user can also input upper and lower bound constraints for the variable space, thus avoiding local false minima.

The absolute magnitude of the MUMAS variables can vary by a factor of 10,000 or more. This can hinder the progression of the iterative guesses x^k as one variable can have a much more dominant affect on the residuals than another. To prevent this, the variables $\vec{x}$ can be centred and scaled. This operation sees the variable x_i, within its lower and upper bounds linearly transformed to a new variable with modulus one and unit contribution to the gradient matrix. This allows the steps made in each variable to be roughly equal and as such prevent one parameter dominating the routine.

5.4 Summary and conclusions

The signal processing that transforms the data into a usable form has been discussed in the first part of the chapter. The correct choice of terminator that produces a sensible voltage as well as removing unwanted high frequency noise has been described. A high finesse Fabry-Pérot etalon was used to linearize the data which was necessary to compensates for the nonlinear response of the PZT to the applied electric ramp. By indexing the same mode along the Fabry-Pérot transmission spectrum a polynomial, relating time to frequency, was evaluated. Finally, after division of the background, a software low-pass filter was used to remove any further residual high frequency noise that had survived.

The second part of the chapter described the code which simulated the MUMAS spectrum. The HITRAN database was used to import the spectral information about the absorption lines being probed, and the HITEMP database was also discussed as being the preferred choice if the temperature was high enough. With the use of a numerical approximation to

a Voigt profile, a theoretical absorption spectrum was generated from the HITRAN data in an efficient way. The laser mode spectrum was modelled with a Lorentzian function for the laser modes and a truncated unit-normalized Gaussian as the mode-packet envelope. The use of sparse matrices reduced the necessary memory needed to make such a calculation. The MUMAS spectrum was then generated using the inbuilt cross-correlation function of MATLAB, which resulted in an efficient simulation code.

Finally, the fitting routine and necessary algorithms were described. Newton's method for minimization was briefly described and the necessary conditions of using a function with a well-behaved second order derivative were explained. The use of a weighting vector was mentioned and some computational difficulties involving the Hessian matrix were discussed. Namely, that if the Hessian matrix was to be calculated in full, it would involve a large number of calculations which is why most efficient algorithms favour orthonormal variables or use numerical approximations for the matrix. The use of the inbuilt `lsqnonlin` function in MATLAB was used to find the optimal fitting variables, and it worked well for determining the partial pressures of the target gas mixture.

Chapter 6

MUMAS and its application to engine exhaust gas monitoring

The application of a MUMAS laser system to in-situ simultaneous detection of carbon monoxide and carbon dioxide is described in this chapter. The role of carbon monoxide in nature and industry is summarized and its use as an efficiency monitor for combustion engines is briefly discussed. A MUMAS laser system is setup to monitor the exhaust gases from a spark ignition (SI) engine, which have been dried, cooled and reduced in pressure. The exhaust gases are also monitored with a 4-gas analyser for comparison. The relative performance of the two systems is compared and the potential use of the MUMAS system as a real-time exhaust diagnostic tool is discussed. Potential improvements to the MUMAS system conclude the chapter, as does an extrapolated evaluation of the same system being applied to exhaust gas at atmospheric pressure.

Real-time monitoring of gas species produced by industrial processes is a useful tool in decreasing costs and potentially increasing product quality. A simple, low-cost and robust system would be required. A monitoring system utilizing MUMAS has the potential to fulfil these requirements due to its large spectral coverage, a single laser with a single detector keeping costs low, and high precision. The real-time simultaneous detection of CO and CO_2 is of particular interest due to its importance in monitoring the efficiency of combustion processes. The determination of CO and CO_2 from exhaust gas will be used as a test case for demonstrating the application of MUMAS to multiple species detection of a pair

of industrially-relevant gases. Secondary, should the sensitivity of the MUMAS system be sufficient, the aim is to produce a sensor for the active control of a SI engine.

Exhaust gas from SI engines are primarily a mixture of the following gases

1. carbon dioxide (CO_2)
2. water vapour (H_2O)
3. carbon monoxide (CO)
4. oxygen (O_2)
5. oxides of nitrogen (NO_x)
6. unburnt hydrocarbons (HC)
7. carbon (soot)

The precise composition is dependent upon the operating conditions such as initial air/fuel ratio, fuel composition and temperature. This is not an exhaustive list. For complete combustion the simplified reaction takes the following format

$$CH_4 + 2\,O_2 \longrightarrow 2\,H_2O + CO_2. \tag{6.1}$$

If the mixture is too rich then incomplete combustion will occur resulting in

$$2\,CH_4 + 3\,O_2 \longrightarrow 4\,H_2O + 2\,CO. \tag{6.2}$$

For an equivalent amount of fuel, both produce the same amount of water; however carbon monoxide is produced when the combustion is incomplete which occurs when there is not enough oxygen present. This carbon monoxide can undergo a further reaction to be finally converted to carbon dioxide with additional oxygen, thereby finally releasing all of its energy,

$$2\,CO + O_2 \longrightarrow 2\,CO_2. \tag{6.3}$$

6.1 Carbon monoxide

Carbon monoxide consists of one carbon atom tripled bonded to an oxygen atom and is found naturally in nature. It is a byproduct of some regular animal metabolisms as well as being produced naturally in the troposphere and being expelled from volcanoes and forest fires. Carbon monoxide is also a byproduct of incomplete combustion from human industrial processes and as such is an important molecule to monitor.

6.1.1 Carbon monoxide as an indicator of inefficiency

In a typical engine cycle, if carbon monoxide has been produced, then it will not have the opportunity to undergo the reaction in equation 6.3 in the cylinder, and so will be passed to the catalytic converter. A significant proportion of the potential energy available during combustion goes unused as described by equation 6.2, so carbon monoxide can be utilized as an indicator of an inefficient combustion process. Furthermore, the catalytic converter can only cope with certain levels of the waste products it is designed to remove, so if the engine system is not monitored, then the catalytic converter would soon become poisoned and dangerous emissions could build up and/or be emitted. If CO levels were to reach 12.5% in air (at atmospheric pressure) and an ignition source were available, such as residual heat, then an explosion could be the result [118].

Monitoring of CO levels is key for two reasons, primarily efficiency of fuel, but secondly as a safety measure against a major accident. With the price of oil being high, attention has shifted to making efficient use of current systems as well as their impact on the environment. So there is clearly a strong case for the in-situ monitoring of CO and other exhaust gases to ensure that the engine operates at top efficiency, environmental impact is reduced to a minimum, and potential accidents are avoided.

Carbon monoxide and carbon dioxide ratios in the atmosphere can provide information as to the origin of the gases. One of the larger contributors is the burning of fossil fuels and studies have been carried out in an attempt to map this across particular geographical

regions. [119, 120] These atmospheric sensors use a variety of techniques including differential non-dispersive infrared method (NDIR) which can detect both CO and CO_2 [119], CRDS to detect CO_2, and vacuum UV-resonance fluorescence to detect CO [120].

6.1.2 Carbon monoxide as a toxic gas

Carbon monoxide is an odourless, colourless, tasteless, and initially non-irritating gas which if found in concentrations greater than 100 ppm is considered dangerous to human health. Carbon monoxide is readily absorbed through the lungs and combines with haemoglobin to form carboxyhaemoglobin (COHb). The affinity of this compound is 210 times stronger than oxyhaemoglobin and carbon monoxide poisoning results due to a lack of oxygen being made available from the blood stream to the essential organs. The symptoms of carbon monoxide poisoning are very hard to detect, and even in low concentrations, carbon monoxide is still dangerous as it lingers in the blood stream with a half-life of 300 minutes in normal air. A treatment for carbon monoxide poisoning is to administer pure oxygen to the patient, which reduces the half-life to 90 minutes [121].

Table 6.1: List of symptoms of CO poisoning depending on exposure concentration.

CO concentration	COHb level	Signs and symptoms
35 ppm	$< 10\%$	Headache and dizziness within 6 to 8 hours of constant exposure
100 ppm	$> 10\%$	Slight headache in 2 to 3 hours
200 ppm	20%	Slight headache within 2 to 3 hours; loss of judgment
400 ppm	25%	Frontal headache within 1 to 2 hours
800 ppm	30%	Dizziness, nausea, and convulsions within 45 min; insensible within 2 hours
1600 ppm	40%	Headache, tachycardia, dizziness, and nausea within 20 minutes; death in less than 2 hours
3200 ppm	50%	Headache, dizziness, and nausea in 5 to 10 minutes; death within 30 minutes
6400 ppm	60%	Headache and dizziness in 1 to 2 minutes; convulsions, respiratory arrest and death in less than 20 minutes
12 800 ppm	$> 70\%$	Death in less than 3 minutes

Carbon monoxide is often only dangerous in enclosed and unventilated spaces such as garages, kitchens and basements. Faulty equipment or poor handling is often to blame for its production. Exposure can originate from incomplete combustion of engines, stoves, generators, lanterns and gas ranges or by burning charcoal and wood. Chronic carbon monoxide exposure, which is low level exposure over a long period of time, can come from tobacco smoke, engine exhaust (e.g. being stuck in traffic), and occupational sources (paint stripper, steel plants).

6.1.3 Explosive carbon monoxide

Very few studies have been done on the explosion limits of CO with O_2. A mixture of 12.5% carbon monoxide in air at one atmosphere is explosive, however due to the flow nature of exhausts; this scenario is unlikely to occur. Also, to produce CO in such high quantities from a SI engine would require a mixture that is so rich it would not readily combust. An explosive situation is only ever likely to occur in a confined space such as a basement or flue where a large generator is positioned and the carbon monoxide can build up over time. Carbon monoxide has an atomic mass that is very similar to air (28 compared to 28.8), which means that it will neither settle nor rise and as such will diffuse quite freely within a building. A situation posing considerable risk of CO explosion is in coal-fired power stations. Incomplete combustion of coal is a perennial hazard and excess levels of CO can build up quickly in exhaust flues. A situation like this could be a possible future application of a control system based on CO/CO_2 monitoring.

6.1.4 Current sensors

Most SI engines (especially in cars) contain one or several lambda sensors, that monitor the amount of oxygen in the exhaust gas relative to the outside air. (Elaborate modern-day lambda sensors now measure multiple gases listed earlier in the chapter by combining different circuits into a single unit.) The lambda sensors sit at various points along the

exhaust line. One will often sit before the catalytic converter and another one will be placed after. All of the sensors will be connected to the central processing computer which provides a closed feedback loop for controlling the air/fuel mixture and thus efficiency. Whilst the catalytic converter can remove harmful exhaust gases, it can only do so much before it becomes poisoned and needs to be replaced at a high cost for the motorist. With this in mind, the first lambda sensor serves to protect the catalytic converter from over-working. That said, these lambda sensors only operate correctly when they are at their designated operating temperature. This temperature can be as high as 700 °C, which if left to residual engine heat to achieve, could take many minutes resulting in engine damage and catalytic converter degradation. To combat this, the sensors can be fitted with an electric heater which is powered by the car battery, which can produce the operating temperature within 15 s. The response time of these lambda sensors is in the region of 30 ms once at operating temperature. [6, 122]

The vehicle excise duty[1] levied on a passenger vehicle is determined by its carbon dioxide emissions, as measured on a standardized drive cycle. A drive cycle test is composed of many sections which seek to emulate the day-to-day usage of a vehicle, combining a mixture of urban and open-road usage conditions. Emissions are monitored from the moment the engine is started, and a significant fraction of overall pollutants are emitted at this early stage, as the emissions monitoring and management systems can take up to 15 seconds to reach operating temperature. During this warm-up phase the engine runs without feedback, which can cause undesirable deviation from programmed behaviour, e.g. as the vehicle ages. The adoption of a novel sensor type which is ready instantly could improve these early emissions, by ensuring the engine runs just rich enough to aid the heating of emissions management systems without creating excess pollutants.

During services and routine checks, multi-gas analysers are used to determine the exhaust emissions and see if they comply with the legislation. One such example is the *Sykes Pickavant 324200SP* which can determine CO_2, CO, O_2 and HC to class 1 accuracy. A

[1] Also known as road tax, a large differentiator at time of vehicle purchase and therefore of great importance to automotive manufacturers.

measure of carbon monoxide and carbon dioxide percentage is output every 2 seconds with a readout resolution of 0.01 and 0.1 respectively. The accuracy of the 4-gas analyser is stated to be +/- 5% of the read value.

6.2 MUMAS comparison

Carbon monoxide and carbon dioxide are two inter-related gas species whose concentrations need to be monitored. As such, in-situ detection of these two species would be a suitable test case to determine if MUMAS is a suitable method in a control-type scenario. To that end, an experiment was devised to simultaneously measure the exhaust gas emissions from a combustion engine using the MUMAS technique and the Pickavant 324200SP 4-gas analyser. The aim of the experiment was to primarily establish that the MUMAS technique could reproduce the ratio of the carbon monoxide and carbon dioxide released in the exhaust gas as determined by the gas analyser. A second goal was to estimate a time response of the measurement that was practical but precise, and a final aim was to retrieve individual gas concentrations from the MUMAS spectrum.

6.2.1 Experimental setup and procedure

The MUMAS laser system was set up on a 36×18 inch optical table in the room adjacent to the engine system. During initial trials exhaust gas from a single cylinder optical access engine was used due to an already built-in data acquisition system and the large degree of control of the combustion conditions. However, two main issues came with this approach.

1 By utilizing exhaust gas straight from the engine the moisture condensed inside the needle valve and caused the gas cell pressure to be unstable.

2 The seals on the optical engine would sometimes fail and the experiment had to be aborted.

To solve the latter issue the engine type was switched to a 1.3 litre 4-cylinder petrol turbo-charged Smart engine. The experimental setup could not be placed as close to the engine due the engines confinement within the small room, however less than 10m of tubing was used to feed the exhaust gas into the cell.

To solve the first problem a rudimentary filter system was placed directly in the exhaust line close to the engine. The hot gas was fed into a copper coil tube which in turn was connected to a line filter and both components sat in an ice bath. The hot gases were cooled in the copper pipe and the water condensed out. This condensed water was then captured in the line filter and the mostly dry gas was allowed into the gas cell.

The setup is shown in figure 6.1.

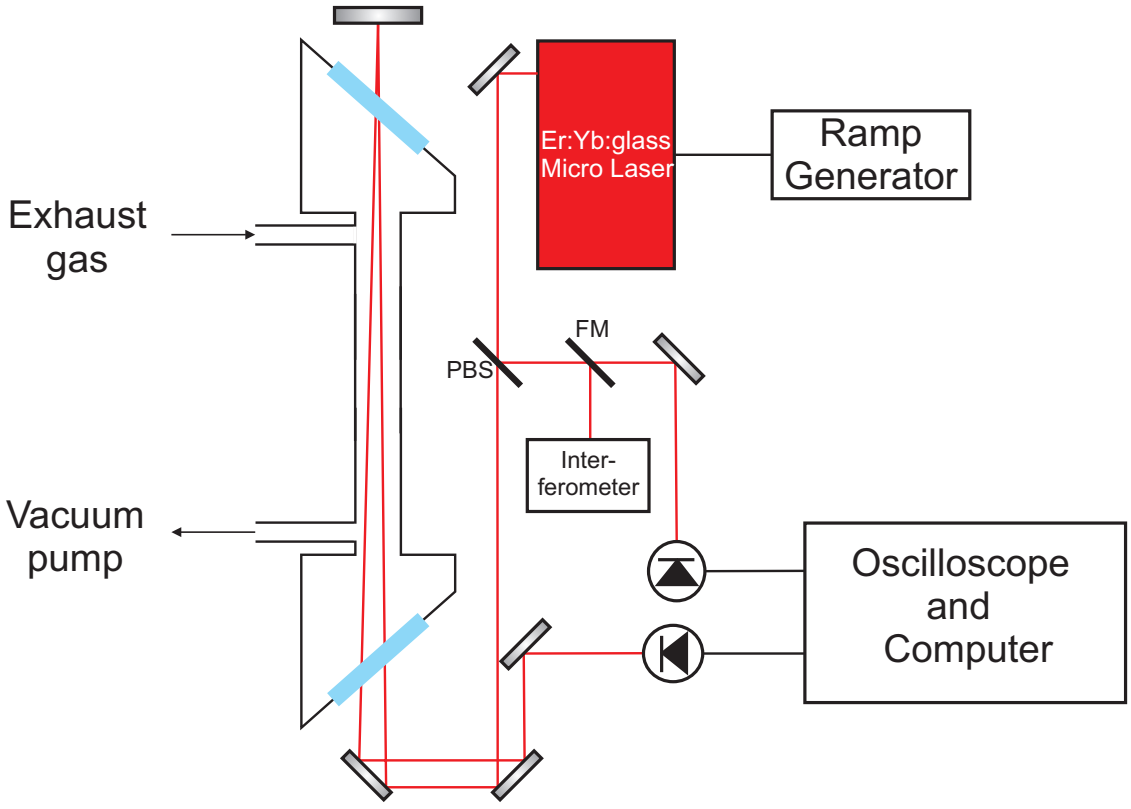

Figure 6.1: The experimental setup used to measure the exhaust gases from the Smart engine. The laser beam is split using a Thorlabs BP545B3 pellicle beam splitter (PBS), which sends one portion of the beam to a reference detector, and the other part is double-passed through an 80 cm cell with angled windows. Both detectors are connected to a Handy Scope HS4 which records the traces on a computer hard drive. The detectors used are Thorlabs DET10C/M, and flip mirror (FM) is installed that can direct the reference beam into an interferometer (Thorlabs SA200-12B) which is used to linearize the response of the PZT.

Given that the detectors were being easily saturated, a fraction of the laser output ($\sim$ 8%) is used for spectroscopy by utilizing the reflection off a quartz wedge. This beam is then divided by a Thorlabs BP545B3 pellicle beam splitter, which sends part of the signal to the reference detector, and the remainder is double passed through the gas cell and collected on a further detector. Both detectors are Thorlabs DET10C/M semiconductor InGaAs. In the reference signal arm, a flip mirror can be brought in to redirect the beam towards the interferometer. This is a very high finesse (F = 494) Thorlabs SA200-12B with a FSR of 1.5GHz. The output of the interferometer allows the nonlinearity of the PZT response to be removed by utilizing the consistent FSR interval between modes. The data is collected and stored through a Handy Scope HS4 oscilloscope.

The fuel used in the experiments was custom-made with a relatively low RON rating. The fuel was premixed with air, and port-injected into the cylinder. The engine was typically run at 1900rpm with fuel/air mixture lambda ratios between 0.78 and 1.10. The pressure in the gas cell was controlled using needle valves to give about 0.1 atmospheres.

Procedure

The laser system was left to warm up overnight before testing began thus allowing the system to be as stable as possible. During the night, a thermocouple was left in the laser box to check if the temperature varied. This experiment provided evidence that the temperature inside the laser setup was stable to within 0.5 K.

A reference measurement of the gas cell containing an inert buffer gas is required to remove the background and any mismatch in laser power falling on the two detectors. Under operating conditions the engine drives a dynamometer to remove the energy generated by combustion. This can also be driven in reverse, whereby the cylinders are turned over by the dynamometer. This operation is used to provide the reference measurement as atmospheric air contains negligible amounts of the target species.

The engine was then engaged and the fuel/mixture ratio determined using the control

computer to vary the injector duration. After allowing a few minutes for the engine and exhaust gas flow to stabilize, MUMAS data was captured at a rate of 2Hz for 5 minutes at each fuel mixture setting, resulting in 600 individual measurements. In total six different air/fuel mixing ratios were used which had the following lambda values: 1.10, 1.01, 0.98, 0.96, 0.92, 0.90. The reference measurements were only recorded for 60 seconds.

6.3 Analysis

6.3.1 Baseline correction

Prior to analysis, each measurement was linearized, filtered and cut to size as discussed in chapter 5. With this data, a process involving an active baseline correction and weighted fit was used to get the optimal amount of information out of each measurement. The aim of the analysis was to evaluate the repeatability and sensitivity of MUMAS when used in an industrial application. Each measurement was fitted using the MUMAS simulation with a least-squares algorithm as described in chapter 5, with the partial pressures of carbon monoxide and carbon dioxide, along with a generic offset being the only variables.

After each measurement was processed the baseline was often not flat which resulted in a skewed analysis due to the least-squares method. To overcome this, regions of low signal-to-noise ratio were identified by computing a best fit to the entire data set (600 averages) to retrieve the signal and the residual of that fit to provide the noise. All data points with a predicted signal-to-noise less than one are earmarked for the baseline correction algorithm. An example of this selection process is shown in figure 6.2.

These located indices are used to fit a 3rd order polynomial through the identified points (shown in red) in both the simulated (figure 6.3) and measurement data sets (figure 6.4).

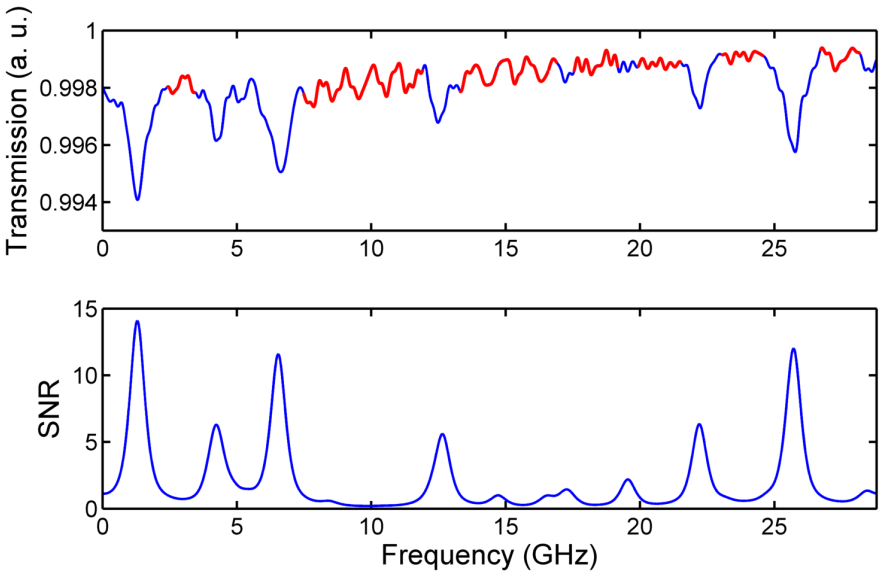

Figure 6.2: The upper figure shows the original data with a sloping baseline. Highlighted in red are the points calculated to have a signal-to-noise ratio less than one. By fitting a cubic polynomial through the red data points, the baseline slope is determined, which could then be subsequently be removed. The lower figure shows the SNR at each point in the data. The signal is derived from a simulation fitted to the mean of 600 spectra, and the noise being the standard deviation of the residuals from the mean of the 600 spectra and the fitted simulation.

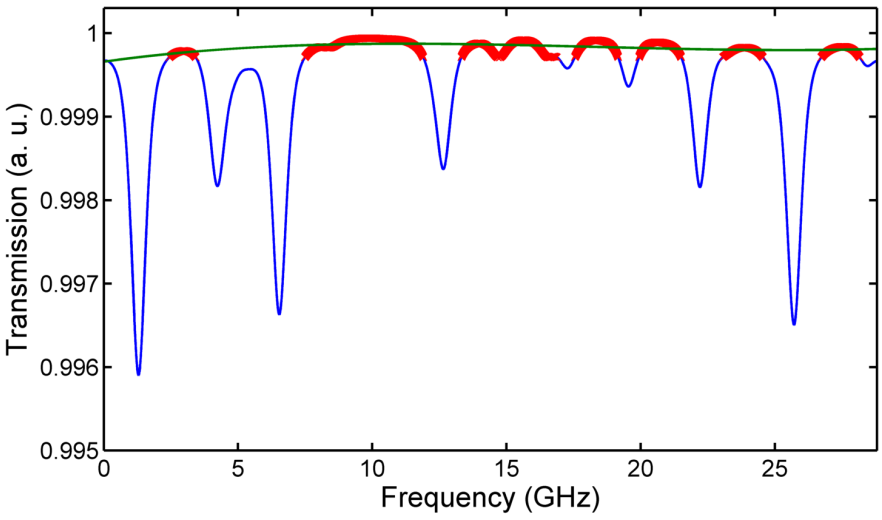

Figure 6.3: The baseline from the simulated MUMAS spectrum is shown in green from plotting a 3rd order polynomial through the red points, which have a SNR less than one. This is the baseline of the data, and as such is combined with the polynomial from figure 6.4 as described in equation 6.4.

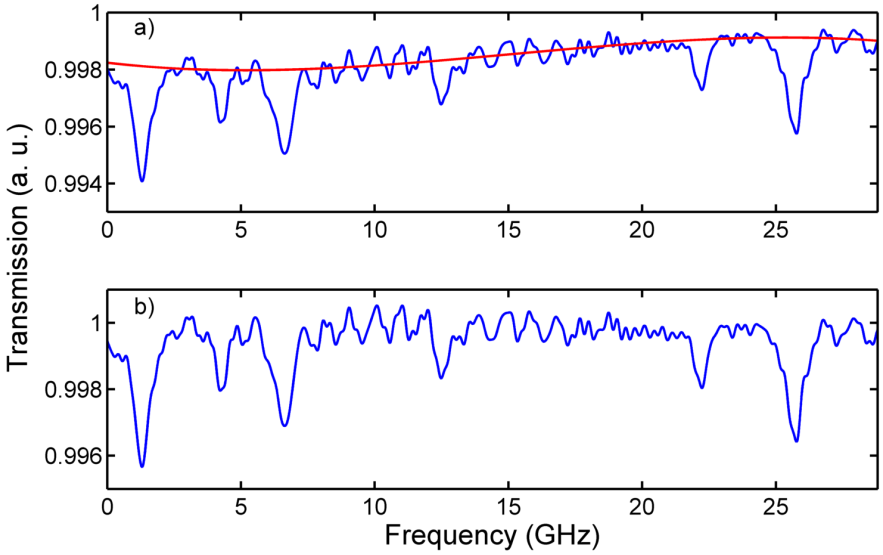

Figure 6.4: Figure a) shows the original data in blue with the baseline best-fit baseline polynomial in red, resulting from a fit using the points in red highlighted in figure 6.2. Figure b) shows the baseline corrected data, which is more robust to the fitting algorithm.

Through use of the equation

$$\text{Correction polynomial} = \frac{\text{Polynomial from simulation}}{\text{Polynomial from data}}, \tag{6.4}$$

any nonlinearity left in the data after the background has been divided away is effectively removed upon multiplication between the correction polynomial and the data. The measurement shown in figure 6.4b) is the finished product.

6.3.2 Averaging of measurement

Random noise fluctuations on the measurement are one of the limitations during the analysis. To try to understand how much of an effect these random fluctuations have on the analysis, the original data set of 600 measurements was converted into other data sets each with a different number of averages. For example if every 2 samples were averaged, then 300 measurements would be available. The advantage of this is the reduction of random noise; however the disadvantage is the reduced temporal resolution. An example of better measurement quality as the number of averages increases is shown in figure 6.5.

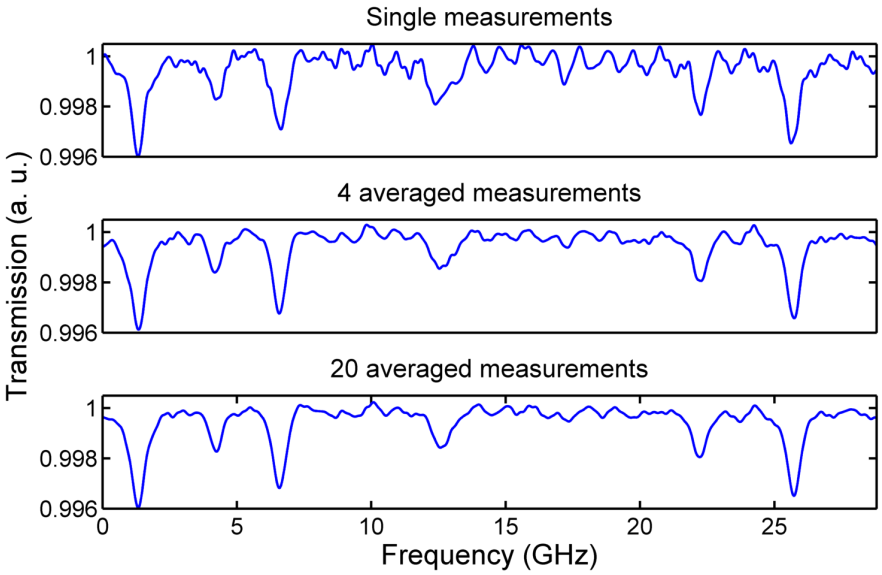

Figure 6.5: Three different MUMAS measurements are shown whereby each figure contains a different number of samples. The upper figure is a single shot; the middle figure is an average of four samples; and the lower figure is an average of twenty. It can be clearly seen that an improvement in the noise levels is seen from a single shot to 4 samples, not so much improvement from 4 to 20.

To get a fuller understanding of the effect of averaging and to try to quantify how the standard deviation of the fitted partial pressures altered, 11 different sample sizes were used; these were 1, 2, 3, 4, 5, 8, 10, 12, 15, 18, 20 samples. The standard deviations produced by each averaging process for each engine condition are shown in figure 6.6. The vertical spread in standard deviations between the different engine conditions is not fully understood. The standard deviation may depend on the quantity of gas being measured, especially in the case of carbon monoxide due to its small contribution. Secondly, the engine stability will contribute to such spread. When the engine is being run with rich mixtures, the torque and gas flow were more unstable and this could be a probable cause. Another likely cause is the laser system not being consistent over the hour-long period during which the data was collected. The behaviour of a multimode laser is difficult to quantify, thus the average of all of the engine modes will be used to get a general error for the MUMAS system.

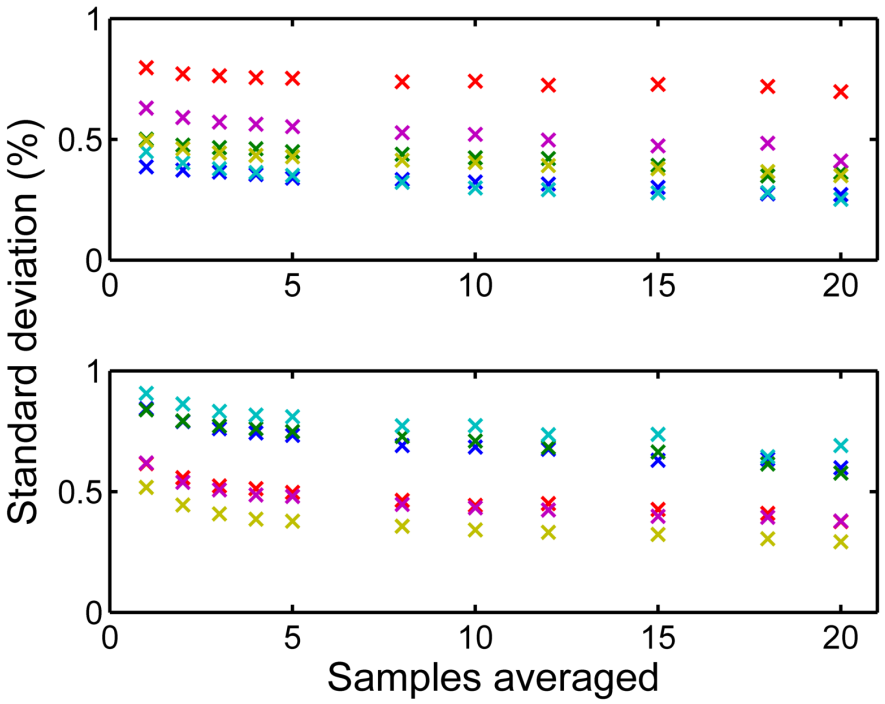

Figure 6.6: Graph showing how the standard deviation is affected by the number of samples used. The upper graph shows carbon monoxide, while the lower graph shows carbon dioxide. The x-axis on both indicates the number of samples averaged to make a single data point. Blue : $\lambda = 1.10$, Green : $\lambda = 1.01$, Red : $\lambda = 0.98$, Cyan : $\lambda = 0.96$, Purple : $\lambda = 0.92$, Gold : $\lambda = 0.90$

6.3.3 Error analysis

The accuracy of a group of measurements can be represented by the standard error on the mean, which can be calculated using the following equation

$$\hat{\sigma} = \frac{\sigma}{\sqrt{N}} \tag{6.5}$$

where N is the number of measurements taken and σ is the standard deviation of the population. Each data set was taken for 5 minutes, so 600 data points are available per engine mode. The initial time resolution is therefore 0.5 seconds.

It is clear from figure 6.6 that the decrease in standard deviation by increasing the number of samples in the averaging process does not follow a $\frac{1}{\sqrt{N}}$ relationship suggesting that the experimental conditions are changing. By using the average of the standard deviation of all 600 measurements from each of the 6 engine conditions, values of $\sigma_{CO_2} = 0.54$ and $\sigma_{CO} = 0.72$

are obtained for carbon monoxide and carbon dioxide respectively. So by taking these σ values as estimates to the population standard deviation, by acquiring 10 measurements the standard error on the mean will be 0.17 for CO and 0.23 for CO_2, with a temporal resolution of 5 seconds. If the downward part of the ramp could be used, as discussed later in the chapter, then this standard error could be achieved within 2.5 seconds. With a linear ramp input used to drive the PZT during one time period the MUMAS fingerprint will be generated twice - once during the upward part of the ramp and once during the downward part of the ramp. The MUMAS fingerprint generated on the downward part of the ramp is a reflection of the one generated on the up ramp.

By looking at a histogram distributions of the partial gas pressures fitted to the data, the shape is broadly Gaussian which supports the use of a normal distribution to calculate any errors. Some examples are shown in figure 6.7.

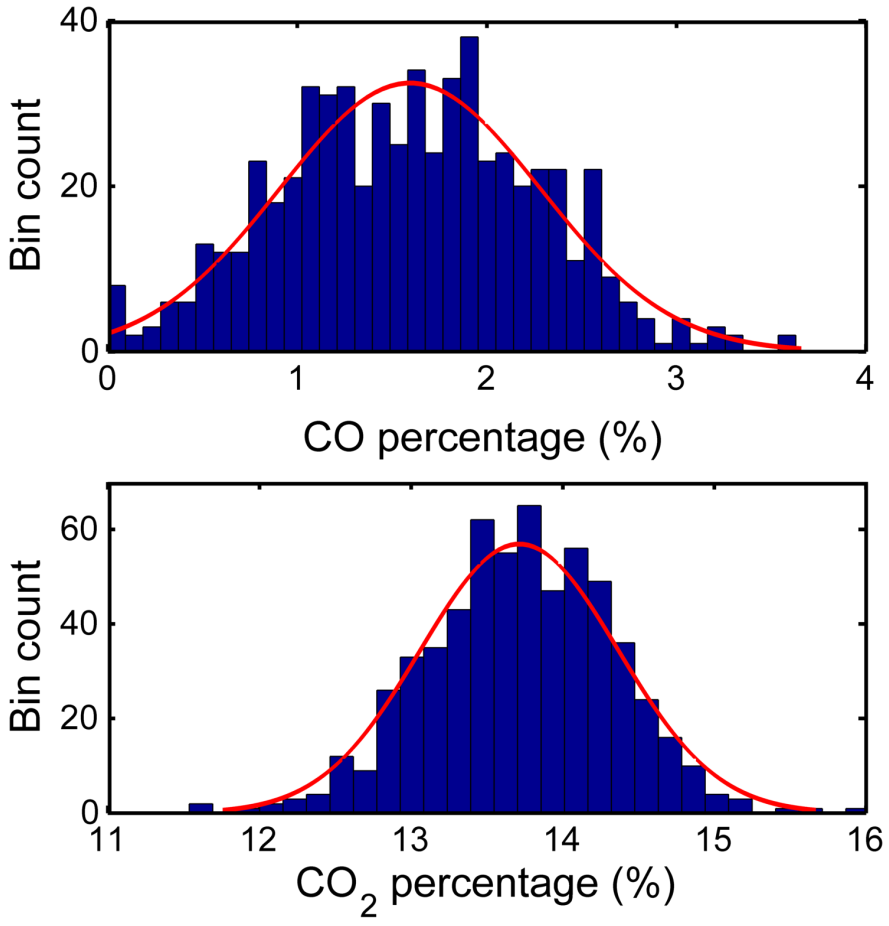

Figure 6.7: Histograms of carbon monoxide (top) and carbon dioxide (bottom) from one engine condition. A Gaussian curve fits very well to both histograms, indicating that a normal distribution is a good approximation of the error.

6.3.4 Weighted fitting

The measurements taken contain a wide range of signal-to-noise ratios as high as 16 but some well below 1. In a regular least-squares algorithm each data point has equal weighting in arriving at the optimum solution. In this analysis, a weighting based on the signal-to-noise ratio will be used to benefit the regions of strong signal and reduce the impact of noise fluctuations on the fitting.

To achieve this a weighting vector was composed in a similar manner to the baseline correction. An estimate of the best fit was obtained to identify the signal and a noise value was gained from the data. Typically, the standard deviation of a region of no absorption features could be used, however another way or arriving at the same number is a more general fashion is to calculate the standard deviation of the residuals from a best fit. An example of a weighting vector is shown in the lower graph of figure 6.2.

The sum of squares was then found by multiplying the square of the residuals by the weighting vector and then summing. The algorithm then reduced this sum as normal.

6.4 Results

By processing data from all 6 engine conditions which ranged from lean to very rich, a comparison could be built up of the performance of the MUMAS system compared with that of the Pickavant 324200SP 4-gas analyser. The gas analyser makes a measurement every 2 seconds and has a read out resolution of 0.1 for carbon dioxide and 0.01 for carbon monoxide. The accuracy according to the manufacturer is 5%.

Firstly, the ratio of carbon monoxide to carbon dioxide is examined as measured by both systems and the results are displayed in figure 6.8.

The error bars displayed on the MUMAS data in figure 6.8 are derived using the method discussed previously. The error bars on the gas analyser are given by the standard deviation of the sample of measurement if it is larger than the readout resolution. In many cases,

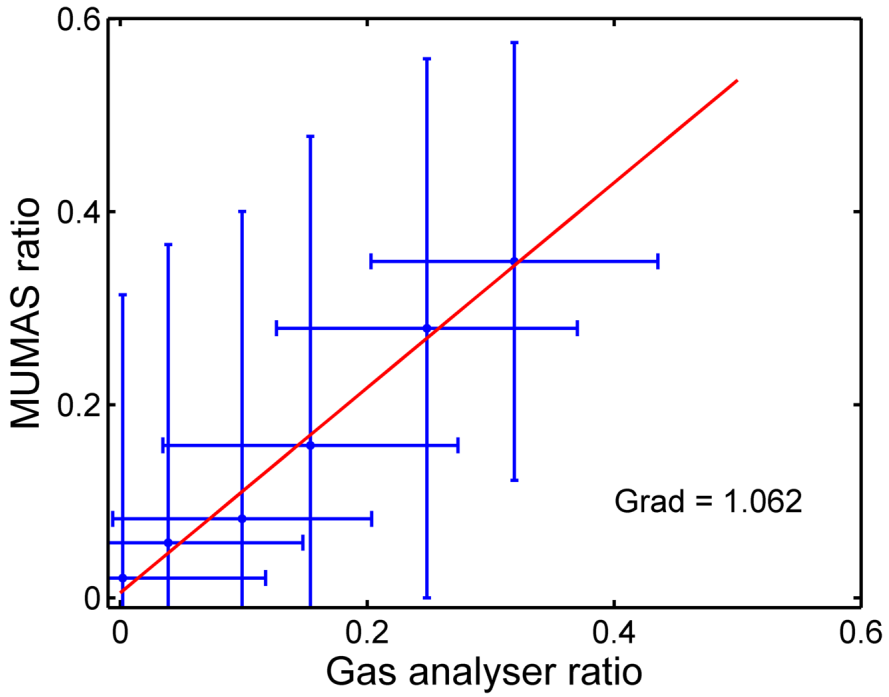

Figure 6.8: This figure shows the CO/CO_2 ratio as measured by MUMAS and the 4-gas analyser. The slope of this curve is 1.062, suggesting a strong correlation between the two systems. The error bars on both axes are the summation in quadrature of the separate CO and CO_2 errors.

especially with the carbon dioxide, the standard deviation is not a suitable number due to the static number output. In these cases, the readout resolution has been used.

To better understand how the MUMAS technique copes with the smaller amounts of carbon monoxide, the plotted ratio should be inverted to give carbon dioxide/carbon monoxide ratio. This will give an indication of the detection limit of MUMAS and the interval in which the result is most reliable. Plotting the ratio in this manner is also sensible in general due to the dominating influence the small amounts of carbon monoxide have on the overall ratio number. The carbon dioxide to carbon monoxide ratio is shown in figure 6.9.

The deviation of the data from the red line of gradient 1 shows that the sensitivity limit of MUMAS is not as low as that of the gas analyser in the current setup. When the absolute carbon monoxide level drops below 0.5% of a total pressure of approximately 0.1 atmospheres, the signal in the MUMAS trace starts to become hidden in the noise and the standard deviation become comparable to the mean, hence the drop away from the red line in figure 6.9. This limitation with the current laser design is partly caused by the relatively

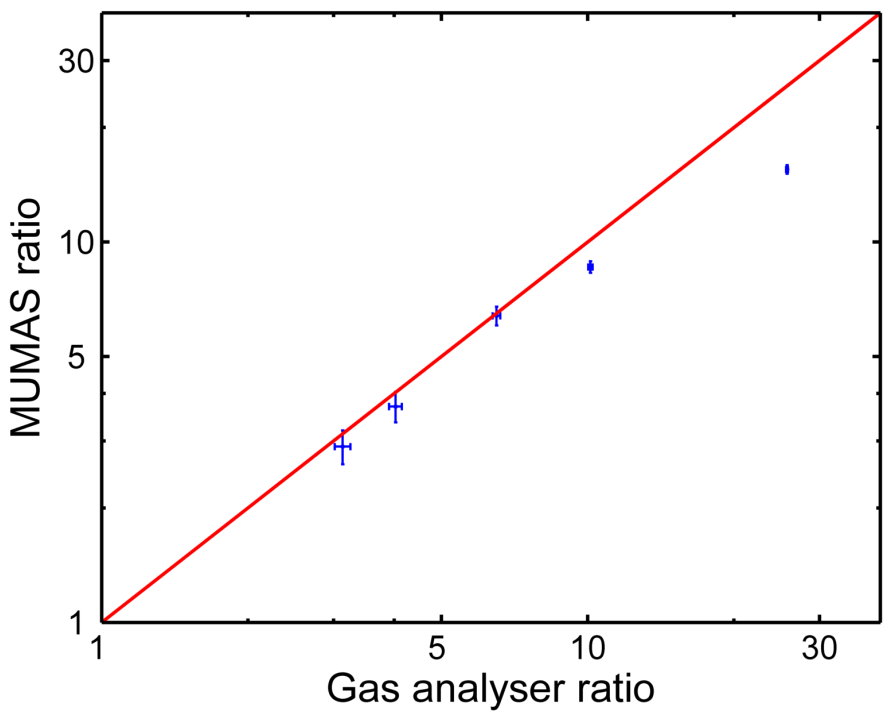

Figure 6.9: Ratio of carbon dioxide to carbon monoxide is shown. Deviation from the equality line shown in red is an indication that the sensitivity of the MUMAS technique is not as good as that of the gas analyser when the amount of carbon monoxide tends to zero. The trends starts to wander away from the red line when the carbon monoxide level gets below 0.5%.

weak absorption line strengths that are being probed and also mode fluctuations associated with laser operation. Other works have achieved better sensitivity using distributed feedback lasers in the same spectral region [11, 21, 123], achieving sensitivities between 171 ppm to 400 ppm using a variety of techniques, meaning that the best sensitivity this region can offer is only an order of magnitude greater than what is currently being achieved. By studying the peak carbon monoxide absorption feature in the MUMAS spectra, a signal-to-noise ratio plot was constructed indicating the smallest detectable amount when SNR=1. This is shown in figure 6.10.

The smallest detectable amount of carbon monoxide is found to be 0.113 torr, which equates to 1486 ppm. The calculation was performed using a measurement which used the average of 600 samples.

A further note to make is that the sensitivity quoted in the literature is derived from experiments which utilize signal-to-noise ratio enhancement techniques, most notably wave-

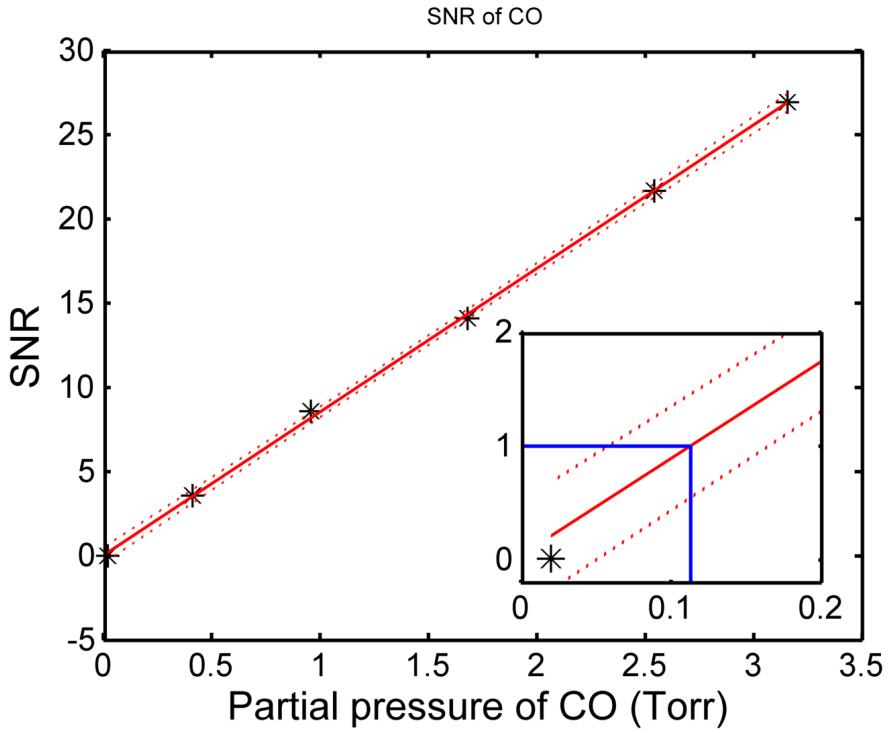

Figure 6.10: Signal to noise ratio versus partial pressure of carbon monoxide in the exhaust gas. The inset shows the point at which SNR=1, indicated by blue line, and this corresponds to a partial pressure of 0.113 torr.

length modulation spectroscopy. MUMAS has been shown to benefit from WMS as well as cavity enhanced absorption spectroscopy [91]. Using a 760 nm diode laser, a SNR improvement of 4 was demonstrated using both WMS and CEAS, whilst a 3.2 SNR improvement was found using $2f$ WMS only. Extrapolating this improvement onto the MUMAS laser system would result in sensitivity in the region of 400 ppm.

MUMAS at atmospheric pressure

By assuming the same noise level when exhaust gas at one atmosphere is sampled, a simulated SNR plot can be calculated that gives the minimum detectable value of carbon monoxide, which is 0.715 torr and this equates to a 941 ppm sensitivity for CO, as seen in figure 6.11. Again assuming a similar SNR enhancement can be achieved using atmospheric exhaust gas, then the minimum detectable amount of carbon monoxide could be 235 ppm which is equivalent to the literature values for the given line strengths.

The carbon dioxide lines are of a comparable strength to the carbon monoxide, so an

approximately equal sensitivity can be applied to that as well. A repeat of this analysis has not been performed because the amount of carbon dioxide in exhaust gases should not approach zero if the engine is operating correctly. An example MUMAS fingerprint of

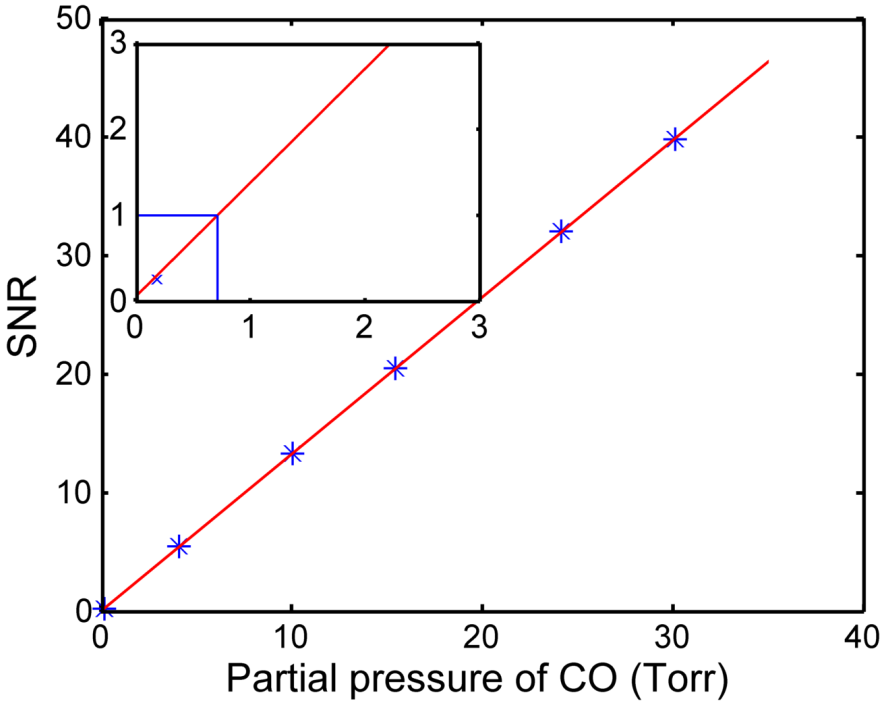

Figure 6.11: Signal-to-noise ratio of a simulated MUMAS fingerprint using the same laser parameters but with 1 atmosphere of exhaust gas. The same percentages are used to derive the partial pressure of carbon monoxide. The point at which the SNR goes to 1, the partial pressure is found to be 0.715 torr.

exhaust gas at 1 atmosphere is shown in figure 6.12.

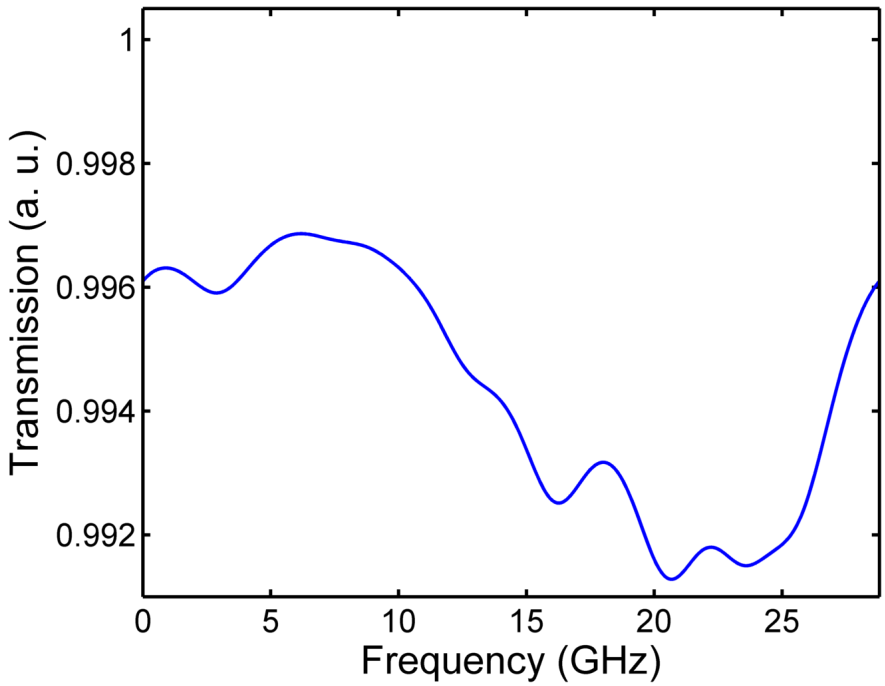

Figure 6.12: MUMAS fingerprint of exhaust gas at 1 atmosphere. The pressure broadening has heavily reduced the resolution of the measurement; however the peak signal has doubled. This results in better ppm sensitivity but at the loss of resolution and unique features within the scan.

6.4.1 Individual gases

As has just been demonstrated, individual gas species concentration can be extracted from the MUMAS spectra by fitting a simulated spectrum to the data, allowing the technique to potentially provide feedback based on specific gas species and not just a ratio. The individual plots for carbon dioxide and carbon monoxide are shown in figure 6.13.

The gradient of the carbon monoxide and carbon dioxide best fit lines are 1.016 and 1.232 respectively. The outliers on the CO_2 graph are excluded from the fit, and the cause of their presence is not fully understood. One potential theory is mechanical instabilities of the system are causing the baseline to alter during the measurement time and this will be more noticeable in the carbon dioxide partial pressure as it is present over a larger portion of the MUMAS spectrum than carbon monoxide. The carbon dioxide curve is also disadvantaged by the small dynamic range that was available from the engine settings. The carbon monoxide graph shows good agreement with all points and has a strong confidence limit.

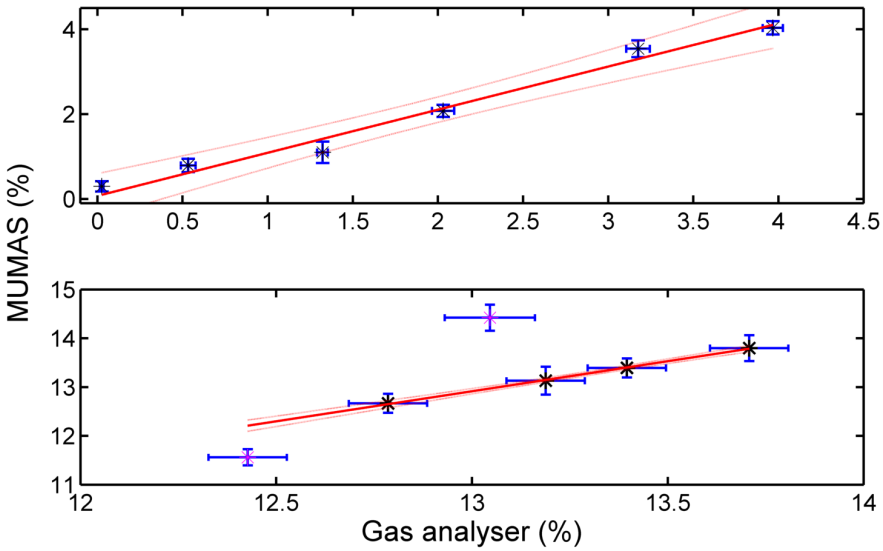

Figure 6.13: Individual gas fits for the 6 different engine settings, with carbon monoxide at the top and carbon dioxide at the bottom. The red line is the best linear fit and the dashed red line is the 95% confidence interval. The magenta markers are outliers which have been ignored when determining the best fit line. All axes are percentages. For carbon monoxide, the gradient is 1.016, and for carbon dioxide it is 1.232.

Figure 6.14 shows a time series of how the gas analyser and the MUMAS system compare over the 5 minute measurement.

6.5 Improvements

6.5.1 Computational limitation

The MUMAS laser scanning is driven by a triangular ramp of frequency 2Hz, where each part of the ramp produces a single scan of the laser modes. This results in 2 MUMAS traces per time period of the ramp one up and one down ramp. The Handyscope stores the data in a temporary buffer before transfer to the computer hard disk and this process takes about 15 ms to achieve. The current set up captures data for ∼300 ms, which include the up ramp, but ignores the down ramp, leaving 185 ms of dead time. So if the data capture rate is to improve to a frequency comparable with engine turn over, then a new data acquisition method will be needed.

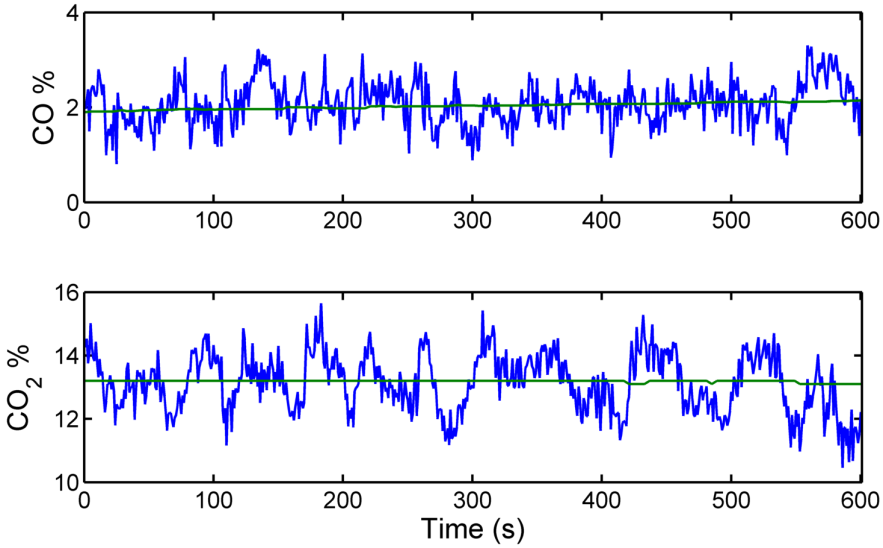

Figure 6.14: A time series of the gas analyser and MUMAS system over the 5 minute experiment. The green line is the gas analyser, whilst the blue line is the MUMAS fit at each measurement. The MUMAS system takes a measurement at a rate of 2 Hz, whilst the gas analyser outputs a reading at 0.5 Hz

6.5.2 Improvement of data capture

One improvement that can be made is the inclusion of the down ramp in the analysis. In the current acquisition, the up ramp and 10% of the down ramp is captured before the information is stored to the computer hard drive. If the computational limitations were overcome and the data transfer time would not result in a trigger being missed, then both traces could be captured. This would improve the temporal resolution of the MUMAS system, as well as getting the maximum out of the potential data available.

6.5.3 Construction improvements

An identified problem with the current data, which could explain the carbon dioxide outliers seen in figure 6.13, is the instability of the laser mode envelope. The laser is set up and aligned with a Czerny-Turner 1 m spectrometer using an Andor InGAS camera viewing the laser modes to judge whether the modes are scanning under a smooth, reproducible envelope. Adjustments are made such that the laser modes scan smoothly underneath a defined envelope function, an example of which is shown in figure 6.15.

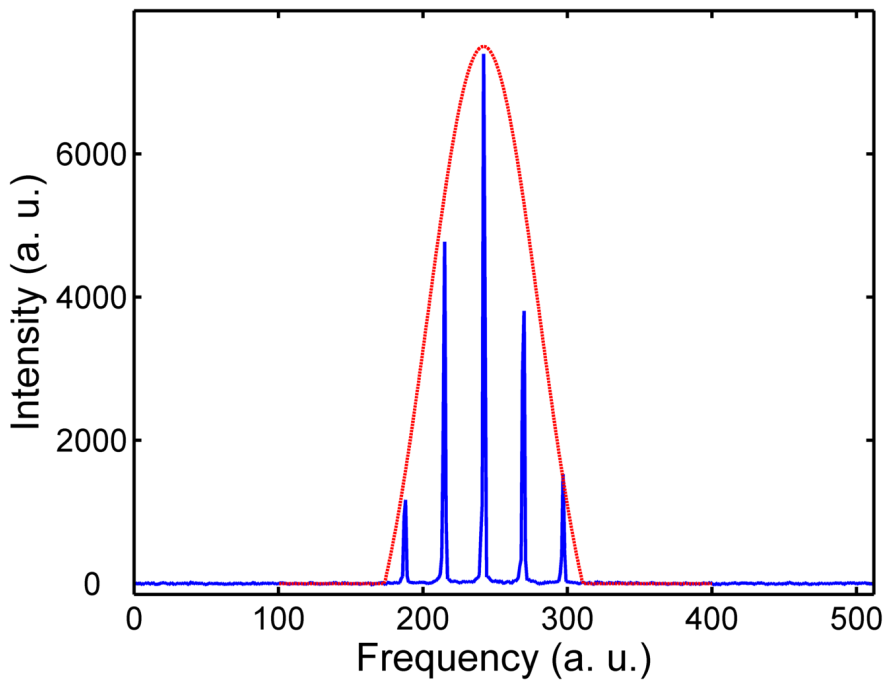

Figure 6.15: The laser modes scan under the envelope function (red dashed line) when the cavity length is altered by the PZT. In this example, the modes are following the simulated truncated Gaussian envelope model very well.

How well the laser modes follow this envelope during the scan is important so that the model correctly identify the power loss ratio for each absorption encountered. An example trace of a set of laser modes following a different envelope is shown in figure 6.16.

In its current form, the laser system is in two main parts - the laser cavity is self-contained within an aluminium housing, and the pumping optics are mounted in an independent XYZ stage. The next stage in development would be to combine these two parts into one machined block of invar[2] metal chosen because of its extremely small thermal expansion coefficient. Another advantage would be a size reduction in the focusing optics used to guide the pump laser light. By integrating the pumping optics into a fibre terminator the pumping system can be drastically reduced in size. Furthermore, if machining tolerances of around 10 µm are obtainable, then the entire system could be designed in a CAD graphics package to permanently fix together with no degrees of freedom. However, this would require further understanding of the feedback processes involved in the design and how that would affect the multimode output of the laser. Also, the change in production methods must be balanced

[2]invar is an alloy of nickel (36%) and iron 64%.

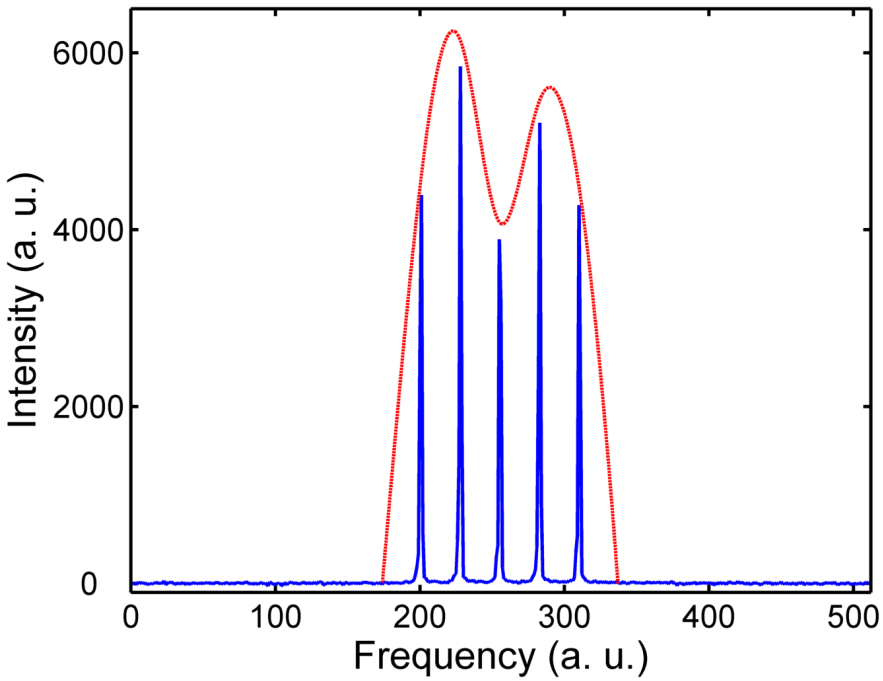

Figure 6.16: An instantaneous example of the laser mode envelope becoming unstable during the scanning of the modes. This instability could be the reason for sub-optimum performance of the MUMAS laser system, and a plan to remove this revolves around the integration of the pumping optics and laser cavity into one solid piece.

off against the total unit cost of a device.

6.5.4 Experimental methods improvements

Optical interference fringes caused by accidental etalons in the experimental setup are a constant limitation of many direct absorption spectroscopy setups. Suppression of these fringes leads to increased signal-to-noise ratio and better experimental performance. Even by taking great care with window angles, wedged optics and deliberately misaligned elements, interfering etalons can easily be created without the user knowing, causing an increase in the apparent noise level on the measurement.

Optical fringes reduction in diode laser absorption spectroscopy have been demonstrated by mechanically vibrating one of the lenses in the system [124]. By changing the spatial position of this lens, the angle between the propagating laser beam and the optical axis is dithered. This angular modulation causes any etalon interference fringes to average out over the measurement period, which can result in a reduction of fringe-induced false absorption

by 40 dB [124].

6.6 Summary and conclusions

The monitoring of carbon monoxide and carbon dioxide is an important tool in optimizing combustion inside a spark ignition engine and protecting the catalytic converter from poisoning. Multimode absorption spectroscopy has been demonstrated as a potential tool for monitoring such emission gases. By building a multimode laser system centred at 1571 nm, where both carbon monoxide and carbon dioxide overtone absorption lines existed, simultaneous detection has been performed. The MUMAS technique has been shown to be able to detect in-situ the CO/CO_2 ratio with good agreement with the 4-gas analyser producing a slope of 1.062, with a measurement repetition rate of 2 Hz. Through comparison of the CO_2/CO ratio from the two systems it was found that the MUMAS ratio disagreed with the 4-gas analyser when the CO content dropped below 0.5%.

By using a characterized value of the standard deviation from 600 samples, a reasonable compromise between temporal resolution and precision was achieved. By taking 10 samples, the standard error on the mean percentage was found to be 0.17 and 0.23 for carbon monoxide and carbon dioxide respectively. This could be achieved in a time of 5 s, which could be reduced to 2.5 s, if faster data collection was available, with no changes to the experimental setup. This is not an inherent limitation of MUMAS however, as using a faster scan rate or different laser e.g. QCL could give a very high rep rate (in the kHz region) and faster response times.

The carbon monoxide concentration is the dominant factor in this ratio calculation because it tends to zero as the engine conditions tend to stoichiometry. So by examining the signal-to-noise ratio of the largest carbon monoxide feature in the MUMAS spectrum, a minimum detectable amount was inferred. This was found to be 0.113 torr in a total pressure of about 85 torr, which equated to 1486 ppm. When this was extrapolated up to 1 atmosphere background pressure, the minimum detectable amount of CO was 0.715 torr, which

was equivalent to 941 ppm. The signal recorded at one atmosphere doubled in size, however the increased broadening mechanisms caused the MUMAS spectrum to become less distinct and the high resolution potential of the laser system was lost. The resolution of the current laser system was less than 8 MHz.

Individual gas concentration were calculated with reasonable confidence from the MUMAS data, allowing particular gases to be directly monitored. The gradients of the best fit linear curves were 1.016 and 1.232 for carbon monoxide and carbon dioxide respectively. The strong confidence limits on these fits is encouraging, however the 2 residuals excluded from the carbon dioxide were worrying, as is the slight deviation from unity. Instability of the mode structure under the modelled envelope function was cited as causing this discrepancy, however the narrow dynamic range of carbon dioxide values taken from the different engine modes made this hard to determine. Should stronger absorption lines be probed by using MIR radiation from a source such as a QCL then the detection limit could be nearer parts per billion.

By extrapolating previous work on signal-to-noise ratio enhancement techniques on MUMAS, an improvement of 3 or 4 could be expected if cavity enhancement and wavelength modulation spectroscopy were both applied to the current laser system. However, the application of WMS to a PZT could prove to be a more difficult challenge than current modulation of a diode laser. However, if this enhancement were to be successful, then the sensitivity of MUMAS in this spectral region would be comparable to other work in the literature, which seemed to be limited near 171 ppm. This detection limit is likely caused by the line strength of the overtones being probed.

The current laser design needs to be improved to make the body more resistant to vibration. This could be done by combining the pumping optics and laser cavity into a single metal body, with the pumping optics integrated into the fibre termination. Not only would this improve the robustness of the system, it would also make it smaller. Implementation of etalon reduction by angularly modulating the laser beam with respect to the optical axis could result in a decrease in the number of fringe-induced false absorption signals and poten-

tially reduce the noise considerably. This could be done by spatially varying the collimation lens in the system. Finally, improvements to data capturing and making use of the down ramp as well as the up from the function generator would halve the time response with no effort needed in changing the laser system design.

A report on this work has been submitted for publication [125].

Chapter 7

Sensitivity enhancement

The application of wavelength modulation spectroscopy (WMS) to MUMAS using the solid-state laser described in chapter 6 to enhance the sensitivity is discussed and tested on a gas of comparable composition. Several calibration-free WMS schemes are proposed and their suitability for MUMAS using a solid-state laser as opposed to a diode laser is assessed. Finally, the signal-to-noise ratio as a function of modulation depth is determined for the first harmonic demodulation and is compared to the SNR of direct absorption in a 16 m *multi-pass gas cell.*

It has already been demonstrated that sensitivity enhancement can be applied to MUMAS with 2f-WMS-CEAS seeing the largest improvement [91]. However, this was performed only using a FP multimode diode laser with the high frequency modulation required for WMS being applied to the driving current. Current modulation is not possible with the Er:Yb laser and so the wavelength has to be modulated using cavity length modulation by the PZT or ceramic actuator. The PZT responds nonlinearly to the applied voltage which is an issue for WMS. The technique relies on the orthogonal nature of the frequency modulation applied to the laser mode(s) and a reference signal. The nonlinear response of the PZT to the reference signal results in a frequency modulation which is not singular in value, and thus the theory described below in section 7.1.1 is not applicable. This chapter explores the initial application of WMS to the solid state laser and determines if the technique is feasible with the current setup.

7.1 Wavelength modulation spectroscopy

Wavelength modulation spectroscopy (WMS) is a sensitivity enhancement technique that can reduce the noise on a measured signal when compared to a direct absorption technique, thus increasing the signal-to-noise ratio on the data collected. This is in contrast to the cavity enhancement techniques which aim to improve the measured signal by increasing the effective absorption path length. WMS works by utilizing lock-in phase detection with reference to a high frequency signal (f_w) that is applied to the laser setup and also supplied to the lock-in amplifier. WMS can commonly lead to a factor of 3-4 improvement in signal-to-noise ratio [91, 126]. Traditionally WMS has been implemented by utilizing a lock-in amplifier which meant that it was impractical to use as a transportable sensor device due to its bulk. However WMS can now be carried out purely by using analytical software (such as MATLAB or Labview) which has reduced the size of the device.

In WMS the wavelength of light, propagating through the gas to be measured and being scanned across the spectral region of interest at a frequency f_0, is modulated at some frequency, f_w, at a certain amplitude, ν_a. When applying WMS to TDLAS there are a number of conditions which need to be met which include:

1. $f_w >> f_0$, with f_w typically being 1-100 kHz

2. ν_a is comparable to or less than the linewidth of a typical spectral absorption feature

This additional modulation results in the instantaneous output frequency of the laser being described by:

$$\nu(t) = \nu_c + \nu_a \cos(2\pi f_w t), \tag{7.1}$$

where ν_c is the centre line frequency [127]. If ν_c is scanned at frequency f_0 across a single absorption feature then the absorbance signal would look like the signal shown in figure 7.1a, in comparison to a direct absorption signal shown in figure 7.1b.

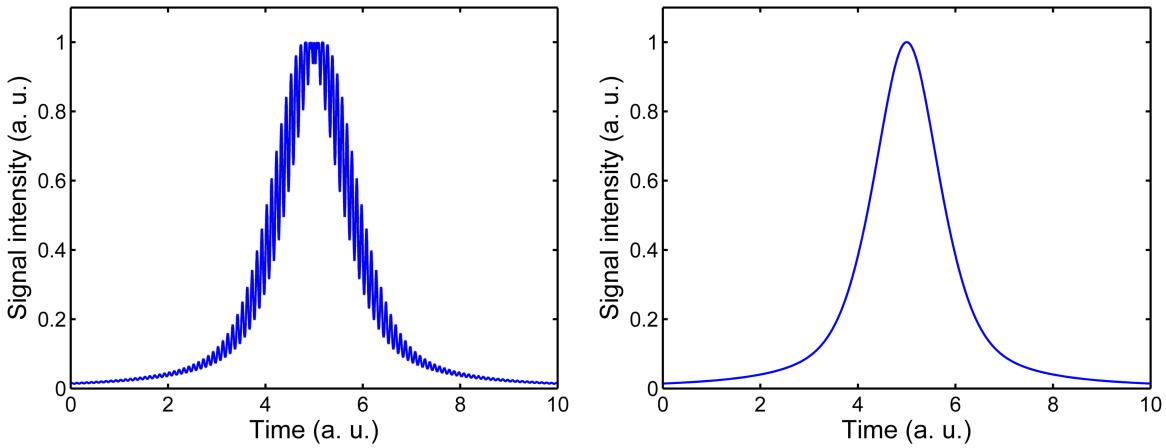

(a) High frequency modulation applied. (b) No modulation applied.

Figure 7.1: These two figures show the absorption profile when a high frequency modulation is applied, a), and with no modulation, b). Figure a) shows how the lineshape of the transition is altered as the laser frequency only is rapidly modulated during the slow scan across the spectral region. This ideal scenario assumes that the laser power is not modulated along with the instantaneous frequency.

7.1.1 Lock-in amplifier

The transmitted laser signal is passed into a lock-in amplifier along with the fast modulation signal (frequency f_w and amplitude ν_a). A typical lock-in amplifier will perform several tasks, however only three of them are crucial to the WMS process: ac coupling of the passed signal, multiplication of the passed signal with the fast modulation, and a low-pass filter. A flow chart of how these processes can be utilized in a typical lock-in amplifier is shown in figure 7.2 [127, 128].

The detected signal is ac-coupled into the lock-in amplifier to remove any DC component of the signal. An optional step at this point is to use linear notch filters to remove the first and second harmonics of the mains frequency 50 Hz. The next step is to multiply the filtered signal (of amplitude V_{exp}, frequency f_w and phase ϕ_{exp}) by a reference signal of frequency f_L, amplitude V_L and phase ϕ_L, which can be passed to or generated by the lock-in amplifier. This results in the following composite signal

$$V_{tot} = V_{exp}\cos(2\pi f_w t + \phi_{exp})V_L\cos(2\pi f_L t + \phi_L), \tag{7.2}$$

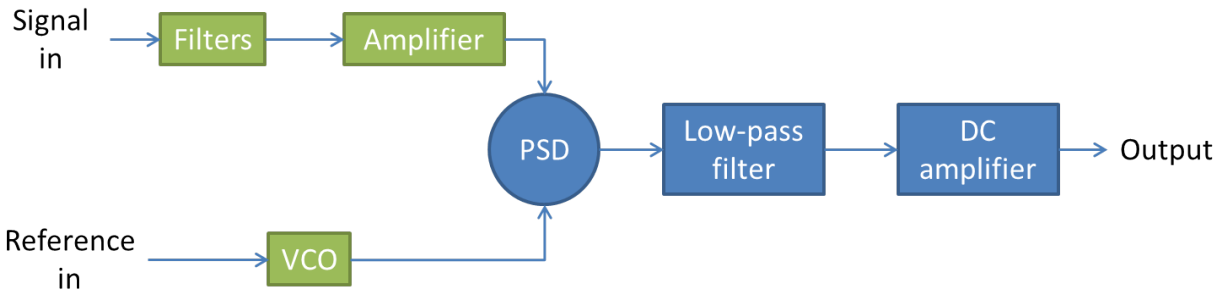

Figure 7.2: A flow chart displaying some of the common functions of a lock-in amplifier. The measured signal is ac-coupled to remove any DC component, before passing through an optional line filter. These line filters usually filter out the mains frequency and its 2nd harmonic. The next stage is to amplify this signal and then pass it to the phase sensitive detector (PSD). The voltage controlled oscillator (VCO) is normally an internal circuit that generates the modulation signal (frequency f_L, amplitude V_L and phase ϕ_L) where all three parameters can be set by the user. References can also be passed to the VCO and it will instead duplicate the given signal and again pass it to the PSD. The phase sensitive detector is, in its simplest terms, a multiplier circuit that performs the task detailed in equation 7.3. A low-pass filter then removes the non-DC components of the signal within a certain bandwidth, typically $0.5 \times f_w$. Finally a further DC amplifier can be used to boost the final output signal intensity [128].

which can be rewritten using the product rule as

$$V_{tot} = \frac{1}{2} V_{exp} V_L \left[\cos\left(2\pi(f_w - f_L)t + \phi_{exp} + \phi_L\right) + \cos\left(2\pi(f_w + f_L)t + \phi_{exp} - \phi_L\right)\right]. \quad (7.3)$$

There are now two frequency components to this composite signal - namely the sum $f_w + f_L$ and the difference $f_w - f_L$. If f_L is chosen such that it equals f_w then equation 7.3 will reduce to

$$V_{tot} = \frac{1}{2} V_{exp} V_L \left[\cos\left(\phi_{exp} + \phi_L\right) + \cos\left(4\pi f_w t + \phi_{exp} - \phi_L\right)\right]. \quad (7.4)$$

The final step is to pass this signal through a low-pass filter of bandwidth $\Delta f < 0.5 f_w$. This removes the high frequency component(s) and leaves only the DC component

$$V_{tot} = \frac{1}{2} V_{exp} V_L \cos\left(\phi_{exp} + \phi_L\right) \quad (7.5)$$

This is phase sensitive detection as the amplitude of V_{tot} is dependent on the relative phase between the reference frequency and the amplitude modulation of the laser wavelength. Any noise contributions to the original signal are removed by the low-pass filter as only frequencies

close to f_w are moved to DC and kept. The size of the modulation signal V_L is known and can be easily removed. The final signal is now proportional to $\cos\theta$ where $\theta = \phi_L + \phi_{exp}$. It is also useful to find the signal which is proportional to $\sin\theta$ as this is the quadrature component of the lock-in signal. Both these signals are often represented by

$$X = V_{exp}\cos\theta \tag{7.6}$$

$$Y = V_{exp}\sin\theta, \tag{7.7}$$

allowing the original signal to be inferred through

$$R = V_{exp} = \sqrt{X^2 + Y^2}. \tag{7.8}$$

So provided both X and Y can be calculated or measured, the desired signal V_{exp} can be found without the need for knowing the relative phase θ.

7.1.2 Harmonic selection and modulation depth

Demodulation can be performed at any harmonic n of the applied modulation frequency f_w, however for higher harmonics the signal intensity diminishes. The advantage of using higher harmonics is that more baseline components are removed, i.e. $n = 2$ removes a linear baseline, $n = 3$ removes any quadratic and linear baseline components and so on. Further advantages of using the even harmonics are that they have their peak value at the centre of the resonance absorption, whereas for the odd harmonic it is zero. The general form of the n^{th} harmonic can be written as [127]

$$\chi_n = \frac{(2 - \delta_{n0})}{\tau}\int_0^{\tau} F\left(\nu\left(t\right)\right)\cos\left(2n\pi f t\right), \tag{7.9}$$

where F is the functional form of the line shape and $\nu\left(t\right)$ is taken from equation 7.1.

Comparative examples of the first and second harmonic demodulation are shown in fig-

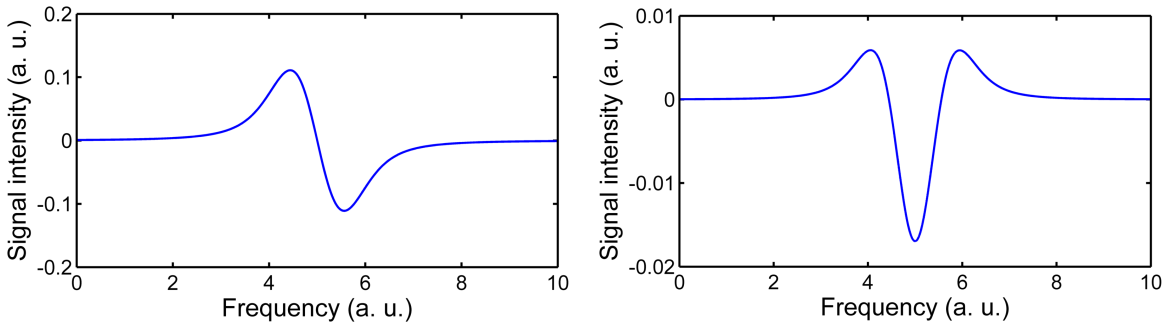

(a) First harmonic. (b) Second harmonic.

Figure 7.3: The first and second harmonic demodulation using WMS. The signal intensity decreases as the harmonic n increases, however the noise level decreases at a more rapid rate. The modulation amplitude ν_a must be optimized for each harmonic and gas conditions to achieve peak signal height.

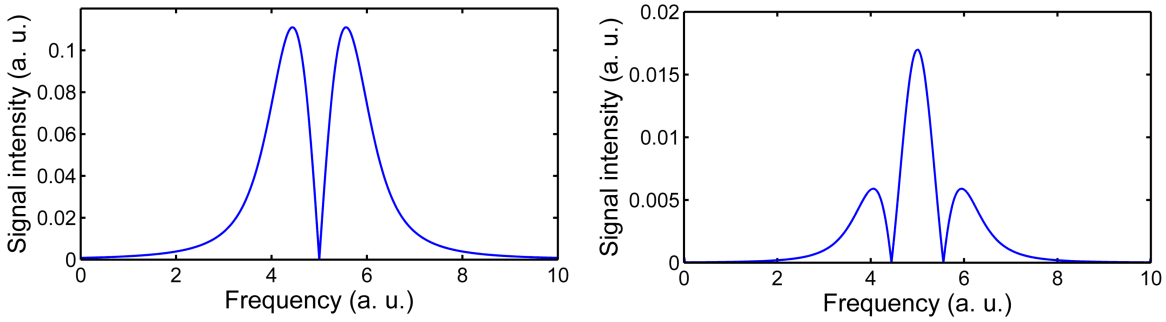

(a) First harmonic. (b) Second harmonic.

Figure 7.4: Phase independent first and second harmonic signals.

ures 7.3a and 7.3b respectively. The signal intensities are similar to the n^{th} derivative of the direct absorption signal, hence the $1f$ trace has one root, $2f$ trace has two roots and so on. These signals are commonly represented as the X component which is produced by the lock-in amplifier, but to achieve the maximum potential signal θ is required to be zero. This is done by adjusting the lock-in phase ϕ_L to be equal to the negative of ϕ_{exp}. This phase value is dependent upon the demodulation harmonic n. Some lock-in amplifiers will also produce the corresponding Y signal which ideally will contain only noise. Through use of equation 7.8 both the X and Y channels can be used to reproduce the original signal which negates the need for optimizing the phase for each harmonic. The phase-independent signals for the equivalent first and second harmonics are shown in figures 7.4a and 7.4b respectively.

A useful parameter to define in WMS is the modulation depth b, which is given by the ratio of the modulation amplitude ν_a and the HWHM of the absorption feature being

measured $\Delta\nu$

$$b = \frac{\nu_a}{\Delta\nu}. \tag{7.10}$$

For conventional applications of WMS the selection of this parameter determines which theoretical model is applicable and the peak signal retrieved from the lock-in amplifier. Finally, for a specific modulation depth b, the WMS setup must be calibrated such that the detected signal can be converted into a concentration. The calibration requires the initial knowledge of the modulation depth, the total pressure of the gas to be sampled, the temperature, and the path length.

One of the simplest executions of WMS is in the differential limit where $b \ll 1$. In this instance, the amplitudes of the output harmonics, n, are proportional to the respective n^{th} derivatives of the absorption lineshape [129]. A typical lineshape to use would be a Voigt profile as defined in section 3.2.1 which takes into account several broadening mechanisms. Any calibration of this setup would require a simple family of curves of peak signal height versus known gas concentration, where each curve is typically labeled with a specific total pressure and temperature.[1]

However, the optimal amplitude of the WMS signal is not found within the differential limit of $b \ll 1$. For $n = 1$ and $n = 2$, the optimum modulation depth is approximately 2.2 [130] so in the search for improved signal-to-noise ratios larger modulation depths are needed and this requires different theories to be used, but all still require a calibration to be performed. As the optimum modulation amplitude is proportional to the HWHM of the absorption feature being probed, different pressure conditions will require a different ν_a value which implies that the pressure must be known to optimize the WMS signal. An increase of temperature similarly results in the modulation amplitude being increased to retain the maximum peak signal intensity. When b is optimized for each harmonic, the signal at line centre decreases in the ratio of $1 : 0.68 : 0.36 : 0.24 : 0.18$ as one switches from direct $: 2f : 4f : 6f : 8f$ detection. The noise level decreases more rapidly as previously mentioned

[1]For any given experiment the path length is unlikely to change so a family of curves accounting for different l is not needed.

in the ratio: 1 : 0.01 : 0.001 : <0.001 [131].

For low-pressure studies an $n = 2$ demodulation with optimal modulation depth will have negligible background, whereas for $n = 2$ at high pressures, with optimal depth modulation, may have a large background baseline [131]. In this case it it necessary to use a higher harmonic to further reduce the background level of the signal. Furthermore, the need to know the total pressure of the gas being sampled limits this form of WMS in its application to harsh environments and industrial processes, hence a method which is calibration-free is desired for such applications.

7.1.3 Calibration-free techniques

One of the main drawbacks of WMS is the requirement of a calibration between the signal intensity and the amount of gas being detected. This can be in the form of a previous experiment with known concentrations or by measuring a cell of known gas concentration, at known temperature and pressure, simultaneously with detection of the unknown gas. Several schemes have been proposed and demonstrated which offer a calibration-free alternative and as such make WMS a versatile technique that can be applied in-situ and potentially in harsh environments. Some common schemes will be briefly outlined in this chapter, and their applicability to MUMAS with the laser system described in chapter 4 will be discussed.

Phasor decomposition method

The phasor decomposition method (PDM) is a technique that utilizes the inherent phase shift between the frequency modulation and the laser power modulation to separate the residual amplitude modulation (RAM) and the derivative signals at the first harmonic [129, 101]. Provided the optical depth is small such that the detected harmonic signal is linearly proportional to the number of absorbing molecules present in the laser beam, then a simple Taylor expansion will yield a calibration-free model. The number of terms kept from the Taylor expansion is dependent upon the modulation depth, but this technique has been

demonstrated with modulation depths up to 0.75 [129]. This method is absolute and can yield information on the linewidth, pressure and concentration of target species. It is also advantageous at high temperatures and is potentially suitable for industrial applications.

In the initial paper by Duffin [101], the modulation frequency f_w was chosen such that the phase between the frequency modulation and the laser power modulation was $\pi/2$. This allowed the entire RAM signal to be projected on the measurement axis X, as described in section 7.1.1. The required modulation frequency was 1.25 MHz which was very high and could be problematic to achieve for some lasers, as well as requiring high bandwidth detectors.

A followup paper by the same group [129] gave a more general approach which allowed the RAM signal to be derived for any phase value between the frequency modulation and the laser power modulation. By recording the Y channel as well as the X, the full RAM signal can be derived from both of these channels on a point-by-point basis. The phase between the frequency modulation and the laser power modulation can be derived from these two channels as well, however if the measured $1f$ signal is asymmetric then this becomes very difficult and it is necessary to determine this beforehand via an independent method.

Quantitative WMS

A paper by Henningsen [132] describes a novel calibration-free method which uses the $2f$ demodulation harmonic to empirically find three functions which can be used to determine the pressure and concentration of the target gas species provided the line strengths are known. The three functions cover the apparent width of the second harmonic profile, the peak height above the baseline, and the peak dip below the baseline. All three functions have the modulation depth b as the only variable. This method is primarily suited to extended cavity diode lasers or any laser which exhibits no power modulation when scanned. An application to DFB lasers is proposed by including a linear correction term, even so the best results are found with extended-cavity diode lasers. This method has a better than 10% accuracy over a wide range of modulation depths $0.1 < b < 10$ and is comparatively simple

to execute.

However this method is currently restricted to spectra containing an isolated absorption feature as any overlap of absorption profiles will cause distortions of the line shape, which are not accounted for in the model. So in principle this method could be used for enhancing MUMAS provided the absorption transmissions in the MUMAS spectrum are isolated and not congested. However, this is not the case for the current application to simultaneous CO and CO_2 detection.

$1f$ normalization

For laser sources which have synchronous modulation of the frequency and intensity there exists another calibration-free method for extracting direct information concerning the pressure and concentration of target gas species. By normalizing a higher harmonic profile, usually $n = 2$ by the $n = 1$ profile, any variations caused by changes in laser intensity, partial blocking of the beam path, and vibrating optics, can be removed [133]. This method was originally proposed by Li [134] and is ideally suited to harsh environments as by combining the specific scanning characteristics of the probe laser, spectral data from HITRAN, with this technique, all calibration factors are eliminated. This method has the added benefit of not being dependent upon the lock-in phase as it can utilize the phase-independent equation shown in equation 7.8 and is used by Sun et al [135].

Typically the $n = 2$ profile is used and the success of removing all of the desired noise sources is dependent upon the gas pressure and experimental setup. Background effects on the $2f$ signal can arise from several sources, with three prominent ones being [126]

1. Etalon effects
2. Nonlinear intensity modulation effects on the laser
3. Absorption by gases outside the measurement volume.

Etalon effects arise from interference between optical planes in the experimental setup and

can be avoided through the angling of optical faces and non-normal incidence through windows. Nonlinear intensity modulation effects are caused by the response of the laser to an applied modulation, and provided that they are reproducible, can be subtracted away. Absorption by gases outside the measurement volume (such as atmospheric water vapour when detecting water in combustion engines) can be reduced by purging the beam path with a non-absorbing buffer gas such as nitrogen or argon.

For high pressure monitoring, harmonics greater than $n = 2$ may be required to remove any background signals. In the work of Sun et al [135] up to the 6^{th} harmonic normalized by the $n = 1$ harmonic is described and applied to high pressure carbon monoxide detection, up to 20 atm.

To remove the background sources listed above a measurement of a purged cell is needed. The final signal can then be represented by the following equation [126]

$$\frac{2f}{1f} = \left\{ \left[\left(\frac{X_{2f}}{R_{1f}} \right)_{\text{raw}} - \left(\frac{X_{2f}}{R_{1f}} \right)_{\text{BG}} \right]^2 + \left[\left(\frac{Y_{2f}}{R_{1f}} \right)_{\text{raw}} - \left(\frac{Y_{2f}}{R_{1f}} \right)_{\text{BG}} \right]^2 \right\}^{1/2}, \tag{7.11}$$

where X_{2f} and Y_{2f} refer to the $2f$ signals as described in section 7.1.1, R_{1f} refers to the magnitude of the $1f$ total signal, *raw* refers to the WMS signal when an absorbing gas species is present, and BG refers to the background measurement when a non-absorbing gas is present in the measuring cell.

Again, this method is only applicable to small absorbances but is robust to harsh environments and as such has been practically demonstrated as a suitable method for in-cylinder measurements of pressure and temperature of water vapour [135, 136, 137].

This calibration-free technique of $1f$-normalized $2f$ demodulation has the advantage of being able to be performed using software only and removes the need for a bulky lock-in amplifier. By recording the raw signal from the detector and passing it directly to a computer both harmonic profiles can be derived.

7.2 Application to MUMAS

Of the three calibration-free techniques outlined in section 7.1.3, two of them (phasor decomposition method and $1f$ normalization) take advantage of the laser intensity fluctuating with the same frequency as the applied fast modulation f_w. To see if they are applicable to the PZT modulated laser used in this thesis this dependency must be demonstrated.

7.2.1 Power modulation

To assist in the determination of whether the laser power output modulates coherently with any applied cavity modulation, the slow ramp used to tune the laser comb one mode spacing was examined. Initially, a simulation was performed using the laser comb model described in section 5.2 whereby the laser power was inferred by the sum of the integral of the laser modes under the envelope. Through scanning one mode spacing, the ideal normalized power output variation is shown in figure 7.5. From this simulation, if the laser modes follow the

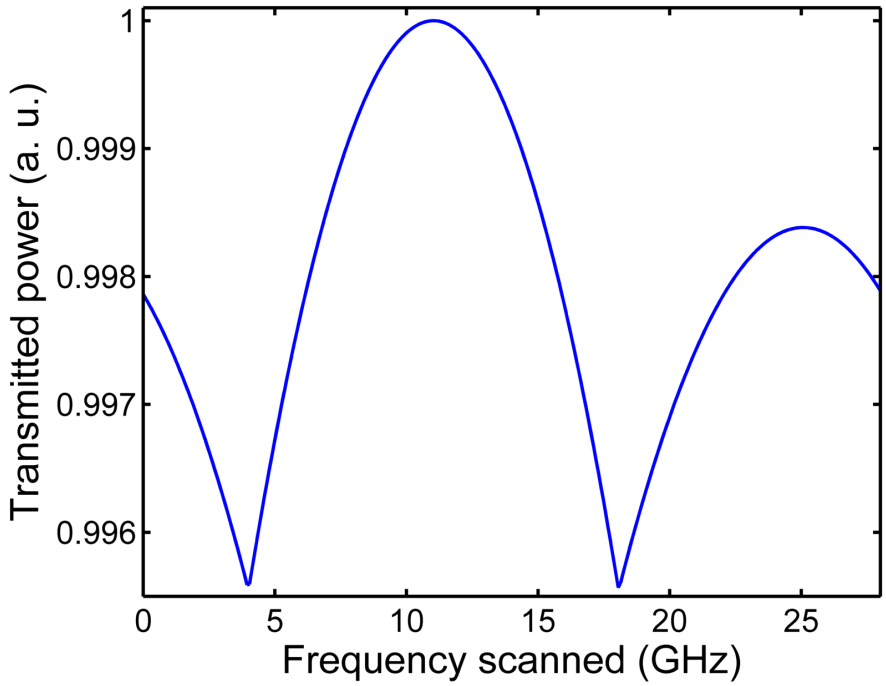

Figure 7.5: Figure showing the normalized power variation as the solid-state laser is scanned one complete mode spacing. The peak power output variation is 0.44% and it clearly has a nonlinear relationship to the frequency scanned. The power variation displayed is for the up ramp only, but if the down ramp was included as well, then the figure would just be mirrored as the modes are retracing their steps.

profile of the envelope function, then the output power variation during the scan will not be constant. However, the peak power variation is 0.44% so therefore to first approximation, it can be assumed that the power output from the solid state laser is constant with respect to frequency.

The power output was recorded at a slow scan frequency of 2 Hz and averaged 20 times to give the signal shown in figure 7.6. The average power fluctuation shown in figure 7.6 is

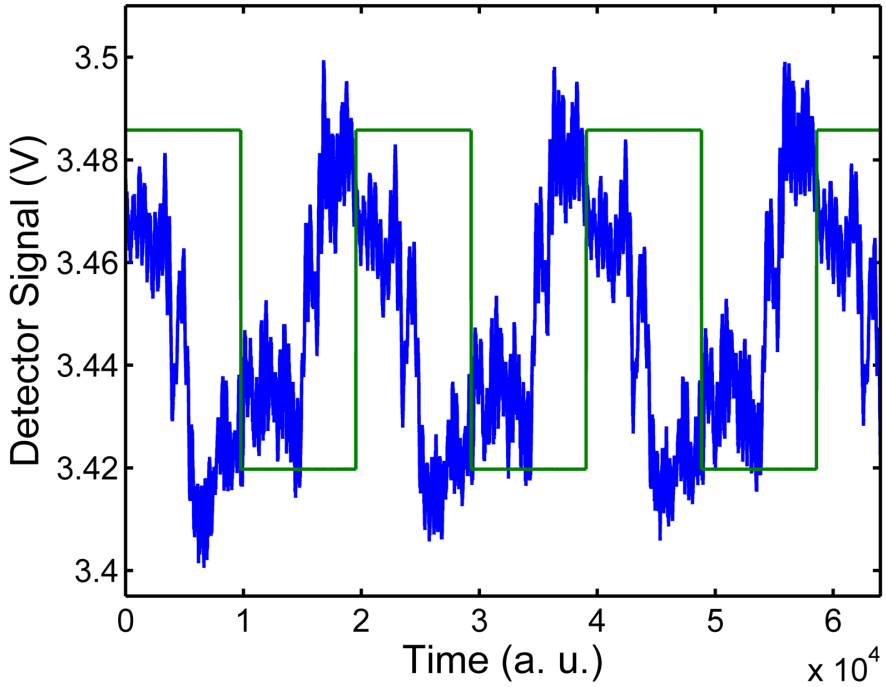

Figure 7.6: The blue trace shows the transmitted laser power and the green TTL line is superimposed for reference of the turning points of the slow ramp scan. A triangular ramp is used to scan the ceramic actuator.

1.74%, which is higher than the simulated value of 0.44%, but still allows the approximation of constant power output should it be used. The pattern of the blue trace seems to follow a triangular pattern with respect to the green TTL trace, however the phase shift between the two plots is much larger than the known lag and in the wrong direction. From observations of the linearisation plots discussed in chapter 5, the detector signal lags behind the TTL pulse by a very small margin. Here the detector signal is in front of the TTL pulse, and by a significant proportion of the ramp width.

A further consideration can explain the absence of any linear amplitude modulation. On the lower frequency side of the laser mode envelope, if there exists a laser mode which is

scanning with an increase in power, there will also exist a laser mode on the high frequency side of the mode envelope which is decreasing in power. The two power variations will largely cancel out, leaving an ideal net power fluctuation as seen in figure 7.5.

By examining the detected signal when a fast ramp is applied it is clear that there is some amplitude modulation on the trace. The upper plot of figure 7.7 shows this as the detected signal has an apparently large noise superimposed on it. By calculating the original R_{1f} harmonic profile, explained by equation 7.8, shown in the lower plot of figure 7.7, the almost zero value indicates that this amplitude modulation is just noise.

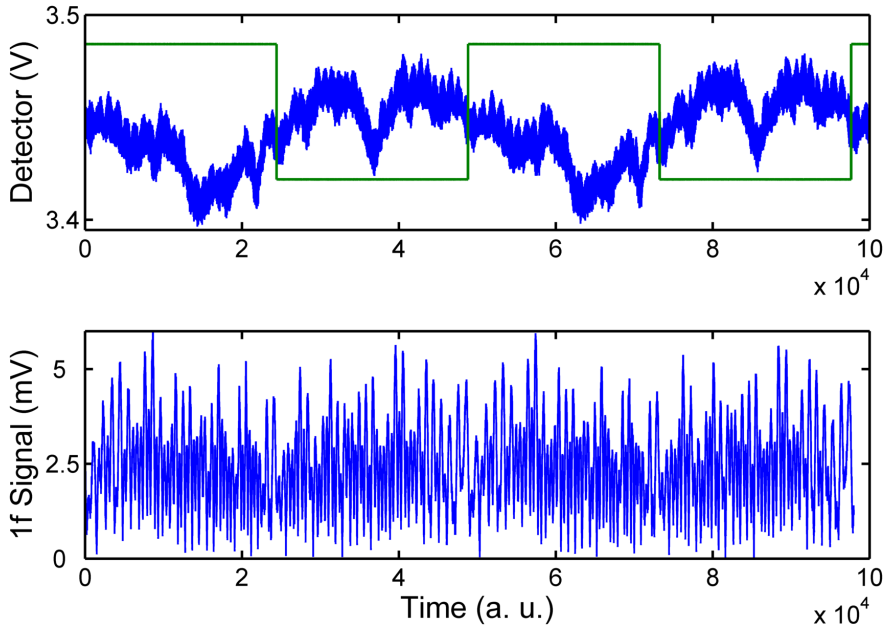

Figure 7.7: The upper figure shows the detected power output of the solid-state laser in blue, with the TTL pulse in green to highlight the repetitive unit. It is clear from the thickness of the blue plot that the fast modulation causes the power output to modulate. However by examining the original signal R of the $1f$ demodulation, shown in the lower figure, it is clear that this power modulation is not coherent with the frequency modulation as there is no appreciable offset present.

From this it can be concluded that the power output from the solid state laser used extensively in the thesis is not synchronous with any frequency modulation applied to it.

7.2.2 Quantitive WMS

The quantitative approach to calibration-free wavelength modulation spectroscopy described by Henningsen [132] requires data from a spectroscopic database, such as HITRAN, ideally a power-stable laser source, and a spectrally isolated transition, to allow the empirical formulae to be derived. The solid-state laser used in this thesis appears to satisfy the laser requirements given that there is no correlation between frequency modulation and power fluctuations. The latter restriction however, would normally rule out its application to MUMAS analysis, given that it would be a very rare occurrence for all of the detected spectral lines to be isolated.

7.2.3 WMS-MUMAS experiment

Having ruled that some of the most common calibration-free WMS techniques are not applicable to MUMAS which utilizes a solid-state laser as described in this thesis, a standard approach to WMS which does use a calibration could still be achieved.

The laser system from chapter 4 is utilized in a simple TDLAS-like setup as described in section 2.3.1. The laser beam is passed through a multi-pass cell with 16 m of path length. The gas cell is filled with 12.46 torr of carbon monoxide and 64.10 torr of nitrogen, which gives a total pressure of 76.56 torr.

To confidently determine the signal-to-noise ratio of nf profiles using the MUMAS laser, an isolated transition is needed. Carbon monoxide is chosen because its transitions are very widely spaced and do not overlap in the MUMAS fingerprint. Given that near 1571 nm carbon monoxide and carbon dioxide have similar transition strengths, the gas mixture of 16% CO within a total pressure of 0.1 atm will produce absorptions of a comparable depth to the exhaust gases monitored in chapter 6.

In this experiment, the high frequency wavelength modulation (applied on top of the slow wavelength scan used for the MUMAS) is generated by the lock-in amplifier (Stanford Research Systems SR830 DSP) and then amplified by a Thorlabs MDT693A open-loop PZT

controller. The chosen value for f_w is 1.5 kHz, as this is a compromise on potential noise elimination and the maximum Voltage ramp being applied to the PZT. Due to the design of the driver which has an internal capacitance of 47 nF and internal resistance of 150 Ω, for frequencies well below 10 kHz, a large portion of the voltage is dumped across the internal impedance. This limits the modulation amplitude to 10 V peak-to-peak, which equates to ∼3 GHz which should be sufficient for total pressures below one atmosphere. This fast ramp voltage is mixed with the slow ramp used to scan the laser modes a single mode spacing and both are applied across the PZT. The detected signal is then passed to the lock-in amplifier and the demodulated signal is output to the Handy Scope HS4 where 32 averages are recorded.

The signal and noise values are derived from the original signal R which is recovered from the X and Y channels as per equation 7.8. The noise is taken as the standard deviation about a portion of the R signal with no known transitions. The signal is derived from difference between the peak value and the mean of the noise level about which the standard deviation is calculated. This is shown schematically in figure 7.8.

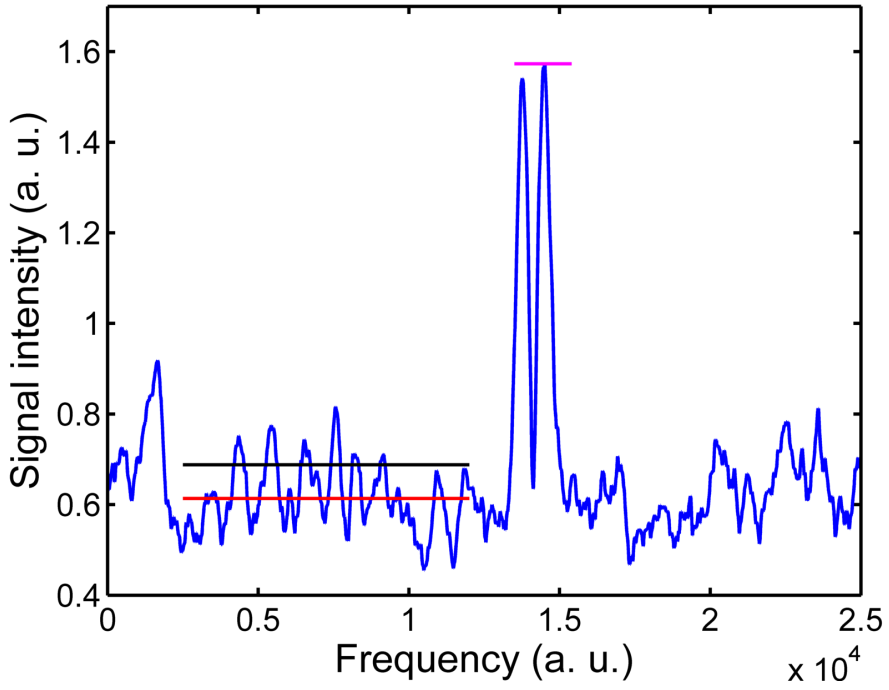

Figure 7.8: Graph showing how the signal and noise are derived from the $1f$ profile. The signal is given by the distance between the peak height (magenta line) and the mean of the baseline (red line). The noise is calculated as the standard deviation about this mean baseline value, shown by the distance between the black line and the red baseline.

By determining the SNR for different modulation depths, the optimum set of parameters can be found for a particular set of gas conditions. The gas conditions explained above equate to a total HWHM broadening of 0.22 GHz; knowledge of this value is needed in order to know the required modulation depth. The plot of SNR as a function of modulation depth is shown in figure 7.9. By fitting a cubic polynomial to the data points an estimate of the

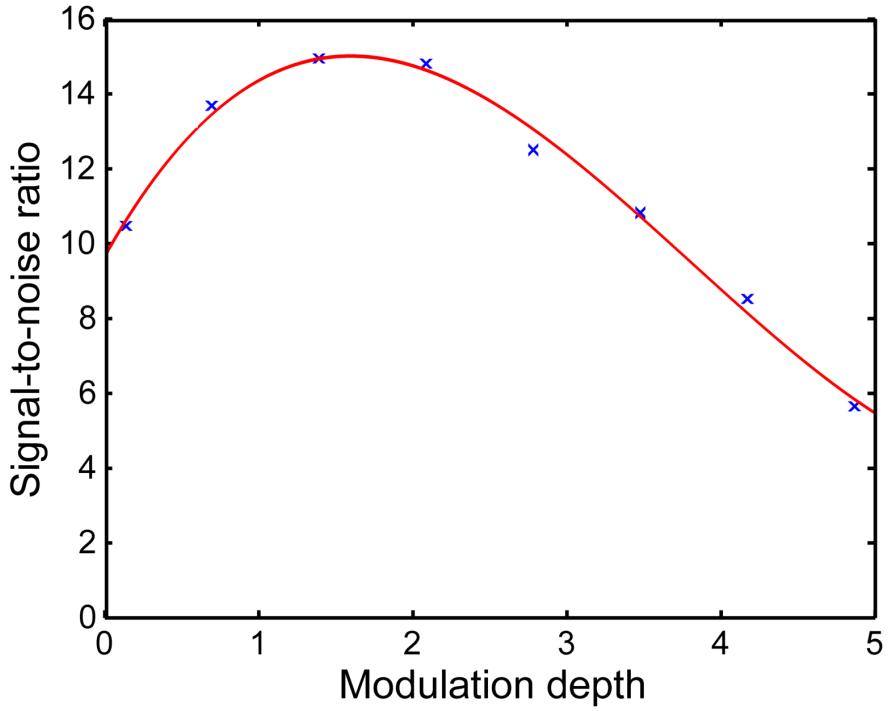

Figure 7.9: The SNR as a function of modulation depth is shown with the blue data points. The red line is a best-fit quadratic which was used to determine the peak signal-to-noise ratio. This was found to be 15.01 at a modulation depth of 1.59.

peak signal-to-noise ratio could be found. This was determined to be 15.01 at a modulation depth of 1.59.

The direct MUMAS signal which was taken using the same gas mixture yielded a SNR ratio of 64.4.

It is clear from the evidence that WMS does not improve the SNR ratio of the MUMAS signals obtained using the solid-state laser used in this thesis. Higher order demodulations did not produce a recognisable signal and as such the experiment was halted after the $1f$ data was collected.

7.2.4 Analysis

Wavelength modulation spectroscopy does not improve the signal-to-noise ratio of the MUMAS spectrum, in fact it is substantially worse than regular direct absorption method. The most likely cause of this is attributed to the laser alignment and how the laser modes respond to the change in PZT length. The power modulation of the individual laser modes, as they are scanned through the mode spacing, has a high amount of random fluctuation which averages out very efficiently. When WMS is applied, this highly non-linear power fluctuation will not be removed and results in a substantial baseline noise level. Furthermore, this baseline noise is not reproducible so cannot be removed by taking a background trace of an empty gas cell.

Another possible cause is the PZT response to the applied voltage. Access to a device which would allow the high frequency laser modulation to be measured was not available. Such a device could be a FP etalon with a FSR of $\sim$5 MHz. As a result it was not possible to determine how the frequency output of the laser corresponds to the applied voltage at high frequencies and small modulation amplitudes.

Finally, the multimode laser is highly sensitive to feedback which determines the mode packet. It is not known how the feedback from the laser optical elements responds to the high frequency modulation of the PZT and this could result in a noisier power output and potential nonlinear effects which the lock-in amplifier cannot remove, and cannot be currently modelled.

7.3 Summary and conclusions

Three calibration-free wavelength modulation spectroscopy methods have been discussed, and their non-suitability for solid-state MUMAS has been demonstrated. The lack of power amplitude modulation in the solid-state laser rules out the phasor decomposition method and normalization through the $1f$ signal. The quantitative method discussed in this chapter

is generally not applicable to MUMAS as this relies on the transition line being spectrally isolated.

Nevertheless, an attempt was made to gauge the signal-to-noise ratio improvement that could be obtained with the solid-state laser system using a calibration. It was found that WMS in fact reduced the signal-to-noise ratio and thus did not provide any sensitivity enhancement. The nonlinear response of the power output with respect to the frequency modulation was suggested as a cause. Further possibilities of unknown feedback mechanisms and the response of the laser output frequency with respect to the applied voltage were also proposed.

For WMS to enhance the sensitivity of the solid-state laser, an engineering upgrade of the laser design is needed such that the power fluctuations of each laser mode are stable. Verification of the frequency modulation caused by the PZT at high frequencies should also be performed using a suitable FP interferometer.

Chapter 8

Conclusions and future work

This chapter summarizes the results of the work on simultaneous in-situ detection of CO and CO_2 and outlines some proposals for future work related to engineering improvements and enhanced data capture schemes. Potential applications of MUMAS in medical diagnostics using analysis of exhaled breath are briefly discussed.

8.1 Conclusions

This thesis has described the further development of the MUMAS technique and its application to the industrially relevant issue of simultaneous multi species detection. By being able to monitor multiple gas species using a single laser unit MUMAS has the potential to offer cheap diagnostics to a range of industrial applications. The chief achievements are listed below.

1. MUMAS has been demonstrated for the first time in the 1571 nm region.

2. MUMAS has been applied to an in-situ combustion application for the first time.

3. Improvements in laser design have resulted in a narrow laser mode linewidths providing high spectral resolution.

4. MUMAS has been applied to the simultaneous detection of industrially relevant gases - carbon monoxide and carbon dioxide.

5. Improvements to the MUMAS simulation code have led to decreased computational times.

8.1.1 Experimental apparatus and procedure

After determining the spectral region where the target gases of carbon monoxide and carbon dioxide overlap, a custom laser system was designed and built to operate at 1571 nm. The use of high-grade erbium:ytterbium-doped phosphate glass resulted in a high quality cavity and thus a narrow laser modewidth of less than 8 MHz.

A planar-concave cavity was built to ensure resonator stability and the use of an angular wedge and AR coating on the erbium laser glass eliminated potential inter-cavity etalons. The custom mirror coating designed by Layertec forced the laser to operate at the desired frequency and, even with the reduction in available gain, a power output of ∼30 mW was achieved.

The PZT used to modulate the cavity length and scan the laser modes performed poorly and could not produce a stable mode structure at scanning frequencies greater than 10 Hz. For that reason a compromise of 2 Hz was used.

Finally, the trial of different mode spacings was done to demonstrate the ease at which the mode spacing can be selected, and to optimize the mode spacing for the absorption spectrum of the target gases. This provides a method for avoiding different absorption features in one gas appearing at the same place in the MUMAS fingerprint.

8.1.2 Data analysis and MUMAS simulation

Improvements to the MUMAS modelling code have been made along with the analysis tools used to prepare the data for fitting to the MUMAS simulation. The oscilloscope termination had been chosen so that high frequency laser noise could be filtered out and also to remove the need for neutral density filter in the beam path to prevent saturation of the detector.

The nonlinear response of the PZT was corrected with the use of a high finesse Fabry-Pérot interferometer, which allowed any repeating laser mode to be indexed and a polynomial created to convert the time axis to frequency.

The MUMAS simulation code now models the laser modes as Lorentzian profiles which reflected the behaviour of a passive cavity. The improved resolution of the linewidth required that the simulated laser comb be made using sparse matrices to avoid computer memory problems. This also has the added benefit of improving the computation speed of this step. The broadened profile of the absorption spectrum was modelled using a numerical approximation of a Voigt line. This yielded excellent results along with much-improved computational time. The generation of the MUMAS spectrum was done using a cross-correlation command which permitted the use of high resolution without running out of memory.

Finally, the use of a nonlinear least-square method of optimising certain unknown parameters was discussed. The use of Newton's method for optimisation is found to be valid for the MUMAS model, and the Hessian matrix indicates how orthogonal the variables are. Partial pressures of the constituent gas to be measured were found to be orthogonal, so Newton's method would be suitable for parameter optimization.

8.1.3 MUMAS and its application to engine exhaust gas monitoring

The in-situ monitoring of carbon monoxide and carbon dioxide from exhaust gas using the MUMAS technique has been demonstrated for the first time. MUMAS was able to determine the ratio of carbon monoxide to carbon dioxide with reasonable precision. In an initial experiment carried out on mock exhaust gas, the ratio of CO/CO_2 was determined to be within the manufacturers certified precision of 1.4%. When the MUMAS system was applied to exhaust gas from a SI engine a 5 s measurement at 2 Hz scanning rate would result in an error of 0.258 and 0.268 on the percentage composition of carbon monoxide and

carbon dioxide respectively. By looking at the carbon dioxide/carbon monoxide ratio it was found that MUMAS started to deviate from the readings of the gas analyser when the CO concentration fell below 0.43% owing to the low signal strength of the absorption at low concentrations.

By examining the signal-to-noise ratio of carbon monoxide, the minimum detectable amount was found to be the equivalent of 1486 ppm in 0.1 atm of exhaust gas. By extrapolating up to atmospheric pressure the MUMAS technique is predicted to have a sensitivity of 941 ppm for carbon monoxide. However this comes at the loss of resolution due to increased pressure broadening. This in itself would not necessarily be a problem for MUMAS in general, however it could result in a loss of precision of particular gas species concentrations if their contribution to the MUMAS spectra is effected by interference from other broadened transitions from gases with a higher concentration.

The MUMAS technique is also able to yield individual gas concentrations measurements with reasonable confidence. The narrow range of concentrations of carbon dioxide emissions encountered in this situation made it difficult to attribute a precision to this gas species.

Instability of the mode structure is the current dominant factor of noise and deviation from the MUMAS model. Engineering improvements of the laser system should yield further immunity to vibrations, however a full quantitative description of the feedback mechanisms in a multimode laser is difficult to achieve. Implementation of etalon reduction techniques by angular modulation of the laser beam relative to the optical axis could improve the technique further.

8.1.4 Sensitivity enhancement

With the present version of the solid-state near infrared laser, wavelength modulation spectroscopy does not improve the sensitivity, in fact it makes it substantially worse. This is largely caused by the nonlinear power response of the individual laser modes which results in a high noise level. Other factors such as feedback and the frequency response of the laser

to the applied Voltage across the PZT are also proposed as possible causes.

8.2 Future work

8.2.1 Infrared MUMAS

As discussed in chapter 4.1.1, carbon monoxide and carbon dioxide overlap in the mid infrared region between 4.4 µm and 5.2 µm. Within the infrared spectrum there are two potential sites which could be utilised: 4.475 µm and 4.850 µm. At 4.475 µm the line strength of carbon monoxide and carbon dioxide is $1 \times 10^{-20}\,\mathrm{cm^{-1}\,molecule^{-1}\,cm^{-2}}$ and $1 \times 10^{-21}\,\mathrm{cm^{-1}\,molecule^{-1}\,cm^{-2}}$ respectively. This is a factor of 100 to 1000 increase on the overtone line strengths accessed at 1571 nm. At 4.85 µm, the carbon monoxide is an order of magnitude higher, whereas the carbon dioxide is an order of magnitude weaker, thus this region is not as suitable for engine exhaust analysis because of the three orders of magnitude difference between the line strengths.

Assuming identical laser parameters listed in section 4.4 except that the centre wavelength is 4.475 µm, a simulated MUMAS trace would give a peak transmission absorption of 0.2, which is 500 times stronger than the measurements taken for chapter 6. An example is shown in figure 8.1.

This improvement in the signal strength could result in either a better sensitivity, or more likely, a smaller gas cell, or both. A reduction in path length to 10 cm would still yield a significantly larger signal than the overtones with the additional benefit of having a compact size. A total path length of 10 cm gives a peak transmission dip of 0.03. This would reduce the overall cost of any sensor system, make it far more practical to install, and easily portable.

Access to this region could be achieved using quantum cascade lasers (QCLs), interband cascade lasers (ICLs), or through difference frequency generation (DFG). The first two would be the more convenient as they would consist of a single diode module complete with drivers

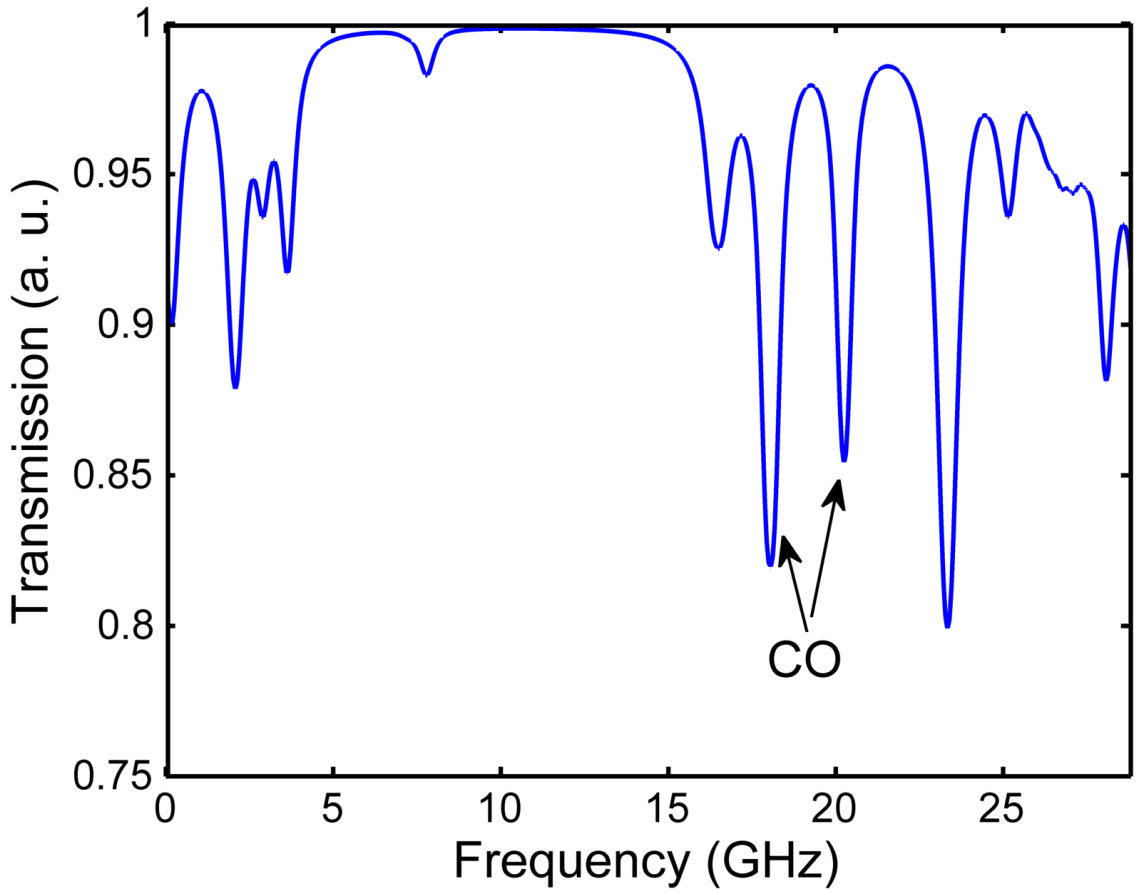

Figure 8.1: Simulated MUMAS fingerprint showing the transmission spectrum at 4.475 µm, which is significantly stronger than the overtones absorption features used in chapter 6. The two carbon monoxide absorption lines are labelled.

and optics. Their disadvantage however is two fold. Firstly, limited research has been done on multimode QCLs and ICLs. Whilst there has been significant progression in their development, most applications require single mode operation. Multimode QCLs and ICLs often have hundreds of modes which makes them directly inappropriate for use with the MUMAS technique. A bandpass filter would be needed to ensure only a small number of modes were used and the technology to create such filters is not yet mainstream.

Secondly, the detector technology in this region is not as advanced as the near infrared. So whilst a line strength improvement of 100 is possible, the increase in noise from using mid IR technology would prevent the full potential from being realized. Detectors are now commercially available which operate at room temperature, but this is only a recent development. Significant investment must also go into the laser current driver as that is often the limiting factor for these types of laser systems.

Difference frequency generation (DFG) is a nonlinear process of combining two frequencies in a nonlinear crystal and outputting the difference of the two, so it is suitable for generating mid IR radiation. MUMAS using a DFG system has been successfully demonstrated in the 3.3 µm region on methane and ammonia. Providing the appropriate lasers can be obtained to produce the necessary mid IR radiation, then this technique could work [138].

It is however quite a bulky setup. Not only are two lasers required, one multimode and one single mode, but the nonlinear crystal must be held and temperature controlled whilst alignment is extremely sensitive to vibrations. DFG also suffers from the same limitations in detector technology discussed previously. This leads to DFG being a very suitable technology for proof-of-principle experiments, however its application in the field will be limited.

8.2.2 MUMAS near 2 µm

The near infrared region between 1.8 µm and 2.1 µm contains a number of interesting molecular species, and those which are available in the HITRAN database are displayed in figure 8.2.

One strong candidate is ammonia which has a very high line strength value in the region $1 \times 10^{-20}\,\mathrm{cm^{-1}\,molecule^{-1}\,cm^{-2}}$. The detection of ammonia relative to combustion is important because it can be used to remove the nitrogen oxides from the exhaust gas. Nitrogen oxides (NO and NO_2) are formed by the oxidation of atmospheric nitrogen at very high temperatures inside the combustion chamber. Nitrogen oxides are a major source of air pollution world wide coming from combustion devices, and their reduction from exhaust gases is mandated by current legislation.

By mixing the exhaust gas with the correct amount of ammonia and passing it over a suitable catalyst, all of the nitrogen oxides can be removed [47]. Two possible chemical reactions which could occur are

$$4\,NH_3 + 4\,NO + O_2 \longrightarrow 4\,N_2 + 6\,H_2O \tag{8.1}$$

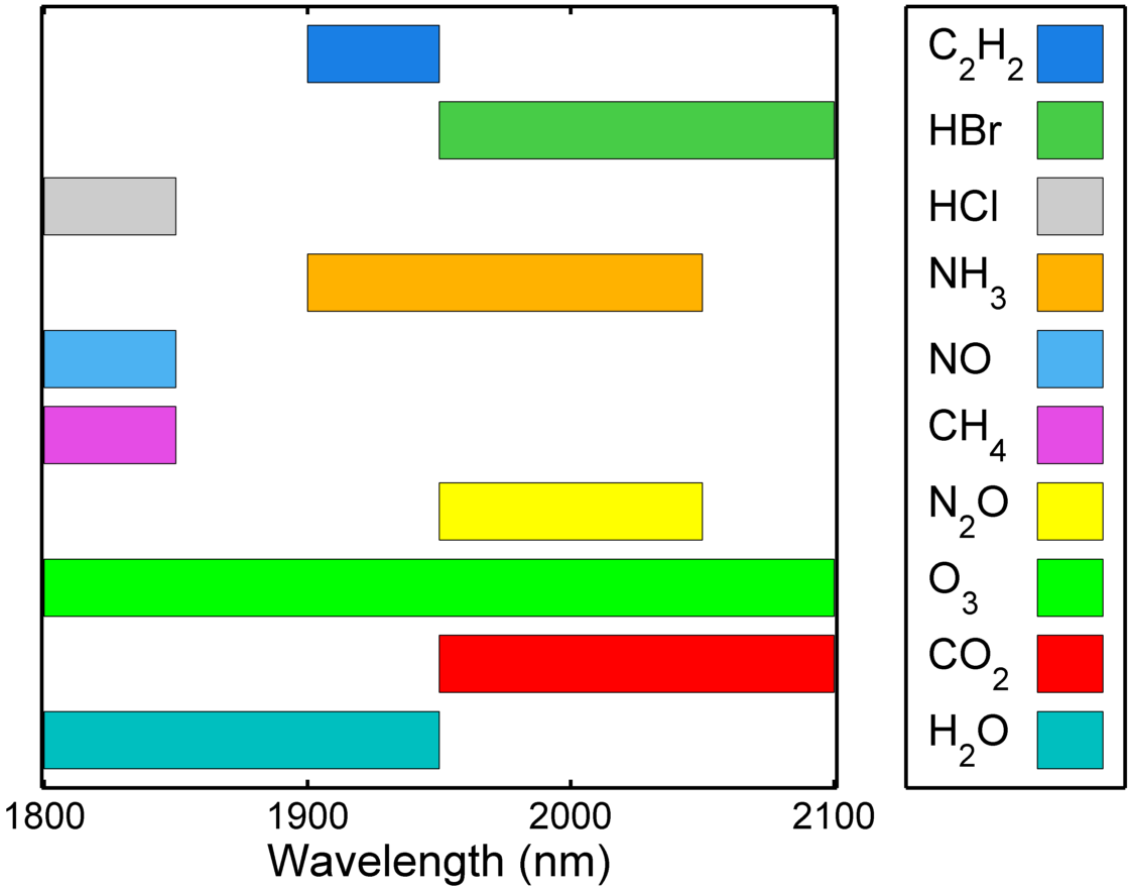

Figure 8.2: Gases taken from the HITRAN database that are available between 1.8 µm and 2.1 µm. The line strengths vary between the gas species as this is a mixture of overtone, fundamental and electronic transitions.

or

$$4\,NH_3 + 2\,NO + 2\,NO_2 \longrightarrow 4\,N_2 + 6\,H_2O. \tag{8.2}$$

A major drawback of this proposal is the amount of ammonia must be exactly right to remove the nitrogen oxides, otherwise if too much is added then another pollutant will be emitted into the atmosphere instead. Any sensor which actively monitors for ammonia in exhaust gas must have a temporal resolution well in excess of 1 kHz to allow a fast closed-loop feedback process to be built.

Laser medium

There are two suitable laser mediums which have been identified as potential candidates. These are holmium doped and thulium doped glasses. Both dopants would be placed inside a

heavy glass, such as germanium oxide glass which can be polished to a laser-grade standard, or tellurite glass. The thulium-doped glass would be pumped with a 794 nm diode, whereas the holmium doped glass would pumped using a 808 nm diode if sensitized using thulium, or 980 nm if sensitized with ytterbium. All of these diodes are readily available with the desired power output of ∼1 W. The literature explains how different amounts of each dopant affects the emission spectrum of the glass, and thus how to acquire the desired output wavelength [139, 140, 141, 142, 143].

Combining a lasing medium with suitable cavity mirrors will result in a multimode laser capable of performing MUMAS near the 2 µm region. A wide variety of industrially-relevant gases are accessible in this region, with some of the lines, such as ammonia, being very strong fundamental transitions. By combining this lasing medium with an improved design as discussed in section 6.5.3 a versatile sensing unit could be made.

8.2.3 Breath analysis

A heavily pursued area of research is that of breath gas analysis and its use as a medical diagnostic tool. The benefits of such diagnostic equipment is that it is non-invasive, quick, and simple to perform. By merely breathing into a gas cell the amount of certain trace gases can be determined which can lead to a diagnosis of some medical conditions. The main components of exhaled human breath are nitrogen, oxygen, carbon dioxide and water, which constitute more than 99% in total. The gases contained within the ∼ 1% not accounted for are the target of breath analysis. Over 1000 individual gases have been determined to constitute this group and they are all naturally synthesized by the body in numerous organic processes [3, 144]. It has been shown that the existence of, or change from the normal level, of any of these gases can be correlated with a particular illness or disease and are called biomarkers. Biomarkers are not necessarily unique to any particular ailment, however 35 have been identified and established with certain disorders if their levels rise above normal. Some natural trace gases are shown in table 8.1, and some disease biomarkers are shown in table 8.2.

Gas	Chemical formula	Typical level	Production source
Acetone	$OC(CH_3)_2$	0 ppm to 1 ppm	Oxidation of fatty acids
Ammonia	NH_3	0 ppm to 3 ppm	Catabolism of proteins
Carbon monoxide	CO	1 ppm to 10 ppm	Degradation of haemoglobin
Carbonyl sulphide	CS_2	0 ppb to 10 ppb	Gut bacteria
Ethane	C_2H_6	0 ppb to 10 ppb	Lipid peroxidation
Hydrogen Cyanide	HCN	0 ppb to 15 ppb	Pseudomonas aeruginosa
Nitrous Oxide	NO_2	50 ppb to 200 ppb	Sythesis of enzymes

Table 8.1: A selection of naturally occurring gases in human breath [144].

Biomarker	Chemical formula	Disease
Acetone	$OC(CH_3)_2$	Lung cancer, diabetes
Ammonia	NH_3	Renal diseases, asthma
Butane	C_4H_{10}	lung cancer
Carbon monoxide	CO	Asthma
Carbonyl sulphide	CS_2	Liver disease, transplant rejection
Formaldehyde	CH_2O	Breast cancer
Hydrogen Cyanide	HCN	Cystic fibrosis
Toluene	$C_6H_5CH_3$	Lung cancer

Table 8.2: A selection of biomarkers and their causes [144, 3].

As some of these biomarkers exist naturally in the breath, any diagnosis device needs to have a precision sufficient to be able to differentiate between normal levels and elevated levels. In the case of acetone, a precision of 200 ppb is likely to be needed given that 1 ppm is the natural amount in human breath. Such devices have been built and a precision of 250 ppb has been demonstrated [145]. Formaldehyde can be a biomarker for breast cancer and techniques have been devised which demonstrate a minimum detectable amount of 74 ppt with a measurement time of 60 s [146].

Longer term ambitions for MUMAS are potentially centred around its use in medical diagnostics. The capability of non-intrusively monitoring multiple species to detect biomarkers is less stressful for the patient, easy to conduct, cheap to implement, and very quick in providing results. This technology if built to the necessary accuracy, precision and sensitivity required for medical diagnostics would remove the need for some blood tests which can be distressing to some patients, particularly vulnerable adults and children. Should the MUMAS technology and precision improve to meet the required specifications, then another avenue of possible applications will open up.

8.3 Final summary and conclusions

Multi species gas detection using multimode absorption spectroscopy has been demonstrated in-situ on an industrially relevant pair of gases. Carbon monoxide and carbon dioxide, chosen as a test case, were simultaneously detected in the exhaust gases of a spark ignition Smart engine and a proof-of-principle for the application of MUMAS to this relevant gas mixture has been demonstrated. This work further highlights the advantages of using MUMAS and has shown it can be applied in an industrially relevant setting for emission monitoring or process control.

Appendix A

Nomenclature of line strengths

In equation 3.19, S_v is the vibrational band strength is the ν_0 is the band centre frequency, ν_{ij} is the transition frequency, L is the square of the matrix element of the direction cosines connecting the upper state to the lower state, E_i is the lower state rotational energy, T is temperature, F is the F factor, and Q_R is the rotational partition sum. [108]

S_v can be expressed as

$$S_v = 8\pi^3 \left|R\right|^2 \nu_0 \exp(-\frac{E_{\nu_i}}{k_B T}) \frac{1}{3hcTQ_v}, \tag{A.1}$$

where Q_v is the vibrational partition function, E_{ν_i} is the lower vibrational state, and R is the matrix element of the rotationless electric dipole moment.

L and F are independent of temperature, and are given as follows for $\Delta J = \pm 1$, $\Delta l = 0$ transitions:

$$L = \frac{m^2 - l^2}{|m|} \tag{A.2}$$

and

$$F = \left(1 + a_1 m + a_2 J' \left(J' + 1\right)\right)^2. \tag{A.3}$$

l is the vibrational angular momentum quantum number, $m = J'' + 1$ for the R-branch ($\Delta J = +1$) and $m = -J'$ for the P-branch ($\Delta J = -1$). Prime and double prime represents

the upper and lower states respectively.

Bibliography

[1] N. L. J Gense, N. Jackson & Z. Samaras. "Euro 5 technologies and costs for Light-Duty vehicles The expert panels summary of stakeholders responses". Technical report, TNO Science and Industry (2005).

[2] Beth L Cummings. "Applications of infrared laser spectroscopy to breath analysis A thesis submitted for the degree of Doctor of Philosophy". Ph.D. thesis, University of Oxford (2011).

[3] Chuji Wang & Peeyush Sahay. *Sensors (Basel, Switzerland)*, **9**, 10 (2009) 8230–62. ISSN 1424-8220. http://www.ncbi.nlm.nih.gov/pubmed/22408503

[4] K. Krzempek, R. Lewicki, L. Nähle, M. Fischer, J. Koeth, S. Belahsene, Y. Rouillard, L. Worschech & F K Tittel. *Applied Physics B*, **106**, 2 (2012) 251–255. ISSN 0946-2171. http://www.springerlink.com/index/10.1007/s00340-011-4857-9

[5] F. M. Schmidt, O. Vaittinen, M. Metsälä, P. Kraus & L. Halonen. *Applied Physics B*, **101**, 3 (2010) 671–682. ISSN 0946-2171. http://www.springerlink.com/index/10.1007/s00340-010-4027-5

[6] J Riegel, H Neumann & HM Wiedenmann. *Solid State Ionics*, **153** (2002) 783–800. http://www.sciencedirect.com/science/article/pii/S0167273802003296

[7] US Department of State. http://www.state.gov/e/oes/rls/rpts/car4/index.htm

[8] Dilip Lashof, Daniel; Ahuja. *Letters to Nature*, **344** (1990) 529 – 531.

[9] S Gordon, R H Knipe, B Y Alvin S Gordon, Chemistry Division, U S Naval Ordnance & Test Station. *The Journal of Chemical Physics*, **59** (1952) 1160–1165.

[10] S Barrass, Y Gérard, R J Holdsworth & P a Martin. *Spectrochimica acta. Part A, Molecular and biomolecular spectroscopy*, **60**, 14 (2004) 3353–60. ISSN 1386-1425. http://www.ncbi.nlm.nih.gov/pubmed/15561620

[11] P A Martin, Edward D Mcnaghten, K A Grant & Alistair M Parkes. *Applied Physics B: Lasers and Optics*, **107** (2012) 861–871.

[12] Y Arita, R. Stevens & P Ewart. *Applied Physics B*, **90**, 2 (2008) 205–211. ISSN 0946-2171. http://www.springerlink.com/index/10.1007/s00340-007-2917-y

[13] Y Arita & P Ewart. *Optics Express*, **16**, 7 (2008) 4437–4442. ISSN 1094-4087. http://www.ncbi.nlm.nih.gov/pubmed/18542540

[14] Y Arita & P Ewart. *Optics Communications*, **281**, 9 (2008) 2561–2566. ISSN 00304018. http://linkinghub.elsevier.com/retrieve/pii/S0030401807013995

[15] V. Weldon, P. Pineda-Vadillo, M. Lynch, R. Phelan & J. F. Donegan. *Applied Physics B*, pages 433–440. ISSN 0946-2171. http://www.springerlink.com/index/10.1007/s00340-012-5167-6

[16] Jos G. J. Olivier, Greet Janssens-Maenhout & Jeroen Peters. "Trends in global CO2 emissions 2012". PBL Netherlands Environmental Assessment Agency (2012). ISBN 9789279253812.

[17] B. Hardy, M. Raybaut, J. B. Dherbecourt, J. M. Melkonian, A. Godard, A. K. Mohamed & M. Lefebvre. *Applied Physics B*, **107** (2012) 643–647. ISSN 0946-2171. http://www.springerlink.com/index/10.1007/s00340-012-5039-0

[18] V. L. Kasyutich, D. Poulidi, M. Jalil, I. S. Metcalfe & P. A. Martin. *Applied Physics B*, **110**, 2 (2012) 263–269. ISSN 0946-2171. http://link.springer.com/10.1007/s00340-012-5154-y

[19] Grady J Koch, Bruce W Barnes, Mulugeta Petros, Jeffrey Y Beyon, Farzin Amzajerdian, Jirong Yu, Richard E Davis, Syed Ismail, Stephanie Vay, Michael J Kavaya & Upendra N Singh. *Applied Optics*, **43**, 26 (2004) 5092–9. ISSN 0003-6935. http://www.ncbi.nlm.nih.gov/pubmed/15468711

[20] J. A. Nwaboh, J. Hald, J. K. Lyngsø, J. C. Petersen & O. Werhahn. *Applied Physics B*, **110**, 2 (2012) 187–194. ISSN 0946-2171. http://link.springer.com/10.1007/s00340-012-5047-0

[21] Alistair M Parkes, Katherine A Keen & Edward D McNaghten. "Trace gas detection using a novel cantilever-based photoacoustic spectrometer with multiplexed optical fiber-coupled diode lasers and fiber-amplification". In "Optics East 2007", pages 67701C–67701C. International Society for Optics and Photonics (2007).

[22] Guangzhen Gao, Baoxue Chen & Tingdong Cai. *Optics and Spectroscopy*, **114**, 3 (2013) 340–346. ISSN 0030-400X. http://link.springer.com/10.1134/S0030400X13030120

[23] V. Koskinen, J. Fonsen, K. Roth & J. Kauppinen. *Applied Physics B*, **86**, 3 (2007) 451–454. ISSN 0946-2171. http://www.springerlink.com/index/10.1007/s00340-006-2560-z

[24] R.M. Mihalcea, D.S. Baer & R.K. Hanson. *Symposium (International) on Combustion*, **27**, 1 (1998) 95–101. ISSN 00820784. http://linkinghub.elsevier.com/retrieve/pii/S0082078498803949

[25] R M Mihalcea, D S Baer & R K Hanson. *Applied Optics*, **36**, 33 (1997) 8745–52. ISSN 0003-6935. http://www.ncbi.nlm.nih.gov/pubmed/18264424

[26] S. Guillon, E. Pili & P. Agrinier. *Applied Physics B*, **107**, 2 (2012) 449–457. ISSN 0946-2171. http://www.springerlink.com/index/10.1007/s00340-012-4942-8

[27] D. Hofstetter, J. Francesco, L. Hvozdara, H.-P. Herzig & M. Beck. *Applied Physics B*, **103**, 4 (2011) 967–970. ISSN 0946-2171. http://www.springerlink.com/index/10.1007/s00340-011-4532-1

[28] D. A. Long, M. Okumura, C. E. Miller & J. T. Hodges. *Applied Physics B*, **105**, 2 (2011) 471–477. ISSN 0946-2171. http://www.springerlink.com/index/10.1007/s00340-011-4518-z

[29] K. Tanaka & K. Tonokura. *Applied Physics B*, **105**, 2 (2011) 463–469. ISSN 0946-2171. http://www.springerlink.com/index/10.1007/s00340-011-4666-1

[30] L. Dong, R. Lewicki, K. Liu, P. R. Buerki, M. J. Weida & F. K. Tittel. *Applied Physics B*, **107**, 2 (2012) 275–283. ISSN 0946-2171. http://www.springerlink.com/index/10.1007/s00340-012-4949-1

[31] J C Nicolas, a N Baranov, Y Cuminal, Y Rouillard & C Alibert. *Applied Optics*, **37**, 33 (1998) 7906–11. ISSN 0003-6935. http://www.ncbi.nlm.nih.gov/pubmed/18301632

[32] J Wang, M Maiorov, D S Baer, D Z Garbuzov, J C Connolly & R K Hanson. *Applied Optics*, **39**, 30 (2000) 5579–89. ISSN 0003-6935. http://www.ncbi.nlm.nih.gov/pubmed/18354555

[33] Xing Chao, Jay B. Jeffries & Ronald K. Hanson. *Applied Physics B*, **110** (2012) 359–365. ISSN 0946-2171. http://www.springerlink.com/index/10.1007/s00340-012-5262-8

[34] A Farooq, W Ren, R K Hanson & D F Davidson. *Applied Physics B: Lasers and Optics*, **107** (2012) 849–860.

[35] Anatoliy a Kosterev, Frank K Tittel, Rüdeger Köhler, Claire Gmachl, Federico Capasso, Deborah L Sivco, Alfred Y Cho, Shawn Wehe & Mark G Allen. *Applied Optics*, **41**, 6 (2002) 1169–73. ISSN 0003-6935. http://www.ncbi.nlm.nih.gov/pubmed/11900141

[36] X. Lin, X. L. Yu, F. Li, S. H. Zhang, J. G. Xin & X. Y. Chang. *Applied Physics B*, **110**, 3 (2012) 401–409. ISSN 0946-2171. http://link.springer.com/10.1007/s00340-012-5269-1

[37] J Houston Miller, S Elreedy, B Ahvazi, F Woldu & P Hassanzadeh. *Applied Optics*, **32**, 30 (1993) 6082–9. ISSN 0003-6935. http://www.ncbi.nlm.nih.gov/pubmed/20856436

[38] Yaping Xiao, Daniel J. Jacob & Solene Turquety. *Journal of Geophysical Research*, **112**, D12 (2007) 1–14. ISSN 0148-0227. http://www.agu.org/pubs/crossref/2007/2006JD008268.shtml

[39] O. Witzel, A. Klein, S. Wagner, C. Meffert, C. Schulz & V. Ebert. *Applied Physics B*, **109** (2012) 521–532. ISSN 0946-2171. http://www.springerlink.com/index/10.1007/s00340-012-5225-0

[40] M. A. Bolshov, Y. A. Kuritsyn, V. V. Liger, V. R. Mironenko, S. B. Leonov & D. A. Yarantsev. *Applied Physics B*, **100**, 2 (2010) 397–407. ISSN 0946-2171. http://www.springerlink.com/index/10.1007/s00340-009-3882-4

[41] D.W. Mattison, J.B. Jeffries, R.K. Hanson, R.R. Steeper, S. De Zilwa, J.E. Dec, M. Sjoberg & W. Hwang. *Proceedings of the Combustion Institute*, **31**, 1 (2007) 791–798. ISSN 15407489. http://linkinghub.elsevier.com/retrieve/pii/S1540748906000605

[42] AS Moore Jr, KE Brown & WM Hall. *Selected Papers of the* 18^{th} *International Laser Radar Conference (ILRC), Berlin*. http://link.springer.com/chapter/10.1007/978-3-642-60612-0_69

[43] H. Sumizawa, H. Yamada & K. Tonokura. *Applied Physics B*, **100**, 4 (2010) 925–931. ISSN 0946-2171. http://www.springerlink.com/index/10.1007/s00340-010-4138-z

[44] Y. Yamamoto, H. Sumizawa, H. Yamada & K. Tonokura. *Applied Physics B*, **105**, 4 (2011) 923–931. ISSN 0946-2171. http://www.springerlink.com/index/10.1007/s00340-011-4647-4

[45] S. M. Cristescu, D. Marchenko, J. Mandon, K. Hebelstrup, G. W. Griffith, L. A. J. Mur & F. J. M. Harren. *Applied Physics B*, **110**, 2 (2012) 203–211. ISSN 0946-2171. http://link.springer.com/10.1007/s00340-012-5050-5

[46] T Stacewicz, J Wojtas, Z Bielecki, M Nowakowski & J Mikoajczyk. *Opto-Electronics Review*, **20**, 1 (2012) 53–60.

[47] Sandro Brandenberger, Oliver Kröcher, Arno Tissler & Roderik Althoff. *Catalysis Reviews*, **50**, 4 (2008) 492–531. ISSN 0161-4940. http://www.tandfonline.com/doi/abs/10.1080/01614940802480122

[48] J Wojtas, T Stacewicz & Z Bielecki. *Opto-Electronics Review*, **21**, 2 (2013) 210–219. http://link.springer.com/article/10.2478/s11772-013-0082-x

[49] Rudy Peeters, Giel Berden, Ari Olafsson, Lucas J J Laarhoven & Gerard Meijer. *Chemical Physics Letters*, **337**, April (2001) 231–236.

[50] Sander Houweling, Thomas Kaminski, Frank Dentener, Jos Lelieveld & Martin Heimann. *Journal of Geophysical Research*, **104**, D21 (1999) 26137. ISSN 0148-0227. http://doi.wiley.com/10.1029/1999JD900428

[51] M Gabrysch, C Corsi, FS Pavone & M Inguscio. *Applied Physics B*, **79** (1997) 75–79. http://link.springer.com/article/10.1007/s003400050253

[52] D M Sonnenfroh & M G Allen. *Applied Optics*, **36**, 15 (1997) 3298–300. ISSN 0003-6935. http://www.ncbi.nlm.nih.gov/pubmed/18253339

[53] D B Oh, M E Paige & D S Bomse. *Applied Optics*, **37**, 12 (1998) 2499–501. ISSN 0003-6935. http://www.ncbi.nlm.nih.gov/pubmed/18273185

[54] B L Upschulte, D M Sonnenfroh & M G Allen. *Applied Optics*, **38**, 9 (1999) 1506–12. ISSN 0003-6935. http://www.ncbi.nlm.nih.gov/pubmed/18305774

[55] Holger Teichert, Thomas Fernholz & Volker Ebert. *Applied Optics*, **42**, 12 (2003) 2043–51. ISSN 0003-6935. http://www.ncbi.nlm.nih.gov/pubmed/12716144

[56] V. Ebert, J. Fitzer, I. Gerstenberg, K.-U. Pleban, H. Pitz, J. Wolfrum, M. Jochem & J. Martin. *Symposium (International) on Combustion*, **27**, 1 (1998) 1301–1308. ISSN 00820784. http://linkinghub.elsevier.com/retrieve/pii/S0082078498805341

[57] Scott a Diddams, Leo Hollberg & Vela Mbele. *Nature*, **445**, 7128 (2007) 627–30. ISSN 1476-4687. http://www.ncbi.nlm.nih.gov/pubmed/17287805

[58] RN Hall, GE Fenner & JD Kingsley. *Physical Review Letters*, **9**, 9. http://link.aps.org/doi/10.1103/PhysRevLett.9.366

[59] AT Ryan & GP Agrawal. *Journal of Quantum Electronics*, **30**, 3. http://ieeexplore.ieee.org/xpls/abs_all.jsp?arnumber=286153

[60] Christopher Davis. "Lasers and Electro-optics". CUP, 1st edition (1996).

[61] A. Hartmann, R. Strzoda & R. Weigel. *Applied Physics B*, **110**, 2 (2012) 195–202. ISSN 0946-2171. http://link.springer.com/10.1007/s00340-012-5048-z

[62] T. Kraetschmer & S. T. Sanders. *Applied Physics B*, **98**, 2-3 (2009) 249–252. ISSN 0946-2171. http://www.springerlink.com/index/10.1007/s00340-009-3836-x

[63] S. Schilt, K. Zogal, B. Kögel, P. Meissner, M. Maute, R. Protasio & M.-C. Amann. *Applied Physics B*, **100**, 2 (2010) 321–329. ISSN 0946-2171. http://www.springerlink.com/index/10.1007/s00340-010-3898-9

[64] Junji Ohtsubo. "Semiconductor Lasers". Springer, 1st edition (2005).

[65] Maximilian Lackner, Michael Schwarzott & Franz Winter. *Optics letters*, **31**, 21 (2006) 3170–3172.

[66] C. J. Smith, S. So, L. Xia, S. Pitz, K. Szlavecz, D. Carlson, A. Terzis & G. Wysocki. *Applied Physics B*, **110**, 2 (2012) 241–248. ISSN 0946-2171. http://link.springer.com/10.1007/s00340-012-5157-8

[67] Jerome Faist, Federico Capasso, Deborah Sivco, Carlo Sirtori, Albert Hutchinson & Alfred Cho. *Science*, **264**, 5158 (1994) 553–556.

[68] Antoine Godard. *Comptes Rendus Physique*, **8**, 10 (2007) 1100–1128.

[69] Raffaele Colombelli, Federico Capasso, Claire Gmachl, Albert L Hutchinson, Deborah L Sivco, Alessandro Tredicucci, Michael C Wanke, A Michael Sergent & Alfred Y Cho. *Applied physics letters*, **78**, 18 (2001) 2620–2622.

[70] S Barbieri, J Alton, HE Beere, EH Linfield, DA Ritchie, S Withington, G Scalari, L Ajili & J Faist. *Optics letters*, **29**, 14 (2004) 1632–1634.

[71] D Rabanus, UU Graf, M Philipp, O Ricken, J Stutzki, B Vowinkel, MC Wiedner, C Walther, M Fischer & J Faist. *Optics express*, **17**, 3 (2009) 1159–1168.

[72] Thomas Töpfer, Konstantin P Petrov, Yasuharu Mine, Dieter Jundt, Robert F Curl & Frank K Tittel. *Applied optics*, **36**, 30 (1997) 8042–8049.

[73] A. S. Arnold, J. S. Wilson & M. G. Boshier. *Review of Scientific Instruments*, **69**, 3 (1998) 1236. ISSN 00346748. http://link.aip.org/link/RSINAK/v69/i3/p1236/s1&Agg=doi

[74] K Liu & M G Littman. *Optics letters*, **6**, 3 (1981) 117–8. ISSN 0146-9592. http://www.ncbi.nlm.nih.gov/pubmed/19701346

[75] Steven Wagner, Moritz Klein, Trupti Kathrotia, Uwe Riedel, Thilo Kissel, Andreas Dreizler & Volker Ebert. *Applied Physics B*, **109** (2012) 533–540. ISSN 0946-2171. http://www.springerlink.com/index/10.1007/s00340-012-5242-z

[76] W Denzer, M. L. Hamilton, G Hancock, M Islam, C E Langley, R Peverall & G A D Ritchie. *The Analyst*, **134**, 11 (2009) 2220–3. ISSN 1364-5528. http://www.ncbi.nlm.nih.gov/pubmed/19838407

[77] HH Gao & A Krier. *Journal of Physics D: Applied Physics*, **32** (1999) 1768–1772. http://iopscience.iop.org/0022-3727/32/15/302

[78] C.F. Kaminski, R.S. Watt, A.D. Elder, J.H. Frank & J. Hult. *Applied Physics B*, **92**, 3 (2008) 367–378. ISSN 0946-2171. http://link.springer.com/10.1007/s00340-008-3132-1

[79] T. Wu, W. Chen, E. Fertein, F. Cazier, D. Dewaele & X. Gao. *Applied Physics B*, **106**, 2 (2011) 501–509. ISSN 0946-2171. http://www.springerlink.com/index/10.1007/s00340-011-4818-3

[80] H. S. Wang, Y. G. Zhang, S. H. Wu, X. T. Lou, Z. G. Zhang & Y. K. Qin. *Applied Physics B*, **100**, 3 (2010) 637–641. ISSN 0946-2171. http://www.springerlink.com/index/10.1007/s00340-010-4151-2

[81] OA Romanovskii. *Journal of Applied Spectroscopy*, **79**, 5 (2012) 799–805. http://www.springerlink.com/index/H2836382K07837Q3.pdf

[82] G. David, A. Miffre, B. Thomas, P. Rairoux & J.-P. Cariou. *Applied Physics B*, **108**, 3 (2012) 689–702. ISSN 0946-2171. http://www.springerlink.com/index/10.1007/s00340-012-5040-7 http://www.springerlink.com/index/10.1007/s00340-012-5066-x

[83] A. Yacomotti, L. Furfaro, X. Hachair, F. Pedaci, M. Giudici, J. Tredicce, J. Javaloyes, S. Balle, E. Viktorov & Paul Mandel. *Physical Review A*, **69**, 5 (2004) 1–9. ISSN 1050-2947. http://link.aps.org/doi/10.1103/PhysRevA.69.053816

[84] X. T. Lou, G. Somesfalean, F. Xu, Y. G. Zhang & Z. G. Zhang. *Applied Physics B*, **93**, 2-3 (2008) 671–676. ISSN 0946-2171. http://www.springerlink.com/index/10.1007/s00340-008-3167-3

[85] Xiutao Lou, Gabriel Somesfalean, Bin Chen & Zhiguo Zhang. *Applied Optics*, **48**, 5 (2009) 990–997. ISSN 1539-4522. http://www.ncbi.nlm.nih.gov/pubmed/19209216

[86] X. T. Lou, C. T. Xu, S. Svanberg & G. Somesfalean. *Applied Physics B*, **109**, 3 (2012) 453–460. ISSN 0946-2171. http://www.springerlink.com/index/10.1007/s00340-012-5115-5

[87] A. I. Nadezhdinsky, Ya. Ya. Ponurovsky, Y. P. Shapovalov, I. P. Popov, D. B. Stavrovsky, V. U. Khattatov, V. V. Galaktionov & A. S. Kuzmichev. *Applied Physics B*, **109** (2012) 505–510. ISSN 0946-2171. http://www.springerlink.com/index/10.1007/s00340-012-5226-z

[88] Anthony OKeefe & David A. G. Deacon. *Review of Scientific Instruments*, **59**, 12 (1988) 2544. ISSN 00346748. http://link.aip.org/link/RSINAK/v59/i12/p2544/s1&Agg=doi

[89] D. J. Hamilton, M. G. D. Nix, S. G. Baran, G. Hancock & A. J. Orr-Ewing. *Applied Physics B*, **100**, 2 (2009) 233–242. ISSN 0946-2171. http://www.springerlink.com/index/10.1007/s00340-009-3811-6

[90] A. Schocker, A. Brockhinke, K. Bultitude & P. Ewart. *Applied Physics B: Lasers and Optics*, **77**, 1 (2003) 101–108. ISSN 0946-2171. http://link.springer.com/10.1007/s00340-003-1237-0

[91] G A D Ritchie, M. L. Hamilton, P Ewart & Y Arita. *Applied Physics B: Lasers and Optics*, **100** (2010) 665–673.

[92] B. Ouyang & R. L. Jones. *Applied Physics B*, **109** (2012) 581–591. ISSN 0946-2171. http://www.springerlink.com/index/10.1007/s00340-012-5178-3

[93] W. Zhao, X. Gao, W. Chen, W. Zhang, T. Huang, T. Wu & H. Cha. *Applied Physics B*, **86**, 2 (2006) 353–359. ISSN 0946-2171. http://www.springerlink.com/index/10.1007/s00340-006-2451-3

[94] P. Malara, M. F. Witinski, F. Capasso, J. G. Anderson & P. Natale. *Applied Physics B*, **108** (2012) 353–359. ISSN 0946-2171. http://www.springerlink.com/index/10.1007/s00340-012-4975-z

[95] M Mürtz, B Frech & W Urban. *Applied Physics B*, **249** (1999) 243–249. http://link.springer.com/article/10.1007/s003400050613

[96] A. G. V. Bergin, G. Hancock, G. A. D. Ritchie & D. Weidmann. *Opt. Lett.*, **38**, 14 (2013) 2475–2477. http://ol.osa.org/abstract.cfm?URI=ol-38-14-2475

[97] P. Gorrotxategi-Carbajo, E. Fasci, I. Ventrillard, M. Carras, G. Maisons & D. Romanini. *Applied Physics B*, **110** (2013) 309–314. ISSN 0946-2171. http://link.springer.com/10.1007/s00340-013-5340-6

[98] J. Morville, S. Kassi, M. Chenevier & D. Romanini. *Applied Physics B*, **80**, 8 (2005) 1027–1038. ISSN 0946-2171. http://link.springer.com/10.1007/s00340-005-1828-z

[99] Sandip Pal & Hugh McCann. *Measurement Science and Technology*, **22** (2011) 115304.

[100] Philip C. D. Hobbs. *Applied Optics*, **36** (1997) 909 – 920.

[101] Kevin Duffin, Andrew James Mcgettrick, Walter Johnstone, George Stewart & David G Moodie. *Journal of Lightwave Technology*, **25**, 10 (2007) 3114–3125.

[102] J. H. Northern, A. W. J. Thompson, M. L. Hamilton & P. Ewart. *Applied Physics B*, **111**, 4 (2013) 627–635. ISSN 0946-2171. http://link.springer.com/10.1007/s00340-013-5382-9

[103] L.S. Rothman, I.E. Gordon, A. Barbe, D.Chris Benner, P.F. Bernath, M. Birk, V. Boudon, L.R. Brown, A. Campargue, J.-P. Champion, K. Chance, L.H. Coudert, V. Dana, V.M. Devi, S. Fally, J.-M. Flaud, R.R. Gamache, A. Goldman, D. Jacquemart, I. Kleiner, N. Lacome, W.J. Lafferty, J.-Y. Mandin, S.T. Massie, S.N. Mikhailenko, C.E. Miller, N. Moazzen-Ahmadi, O.V. Naumenko, A.V. Nikitin, J. Orphal, V.I. Perevalov, A. Perrin, A. Predoi-Cross, C.P. Rinsland, M. Rotger, M. Šimečková, M.A.H. Smith, K. Sung, S.A. Tashkun, J. Tennyson, R.A. Toth, A.C. Vandaele & J. Vander Auwera. *Journal of Quantitative Spectroscopy and Radiative Transfer*, **110**, 9-10 (2009) 533–572. ISSN 00224073. http://linkinghub.elsevier.com/retrieve/pii/S0022407309000727

[104] Anthony Siegman. "Lasers". University Science Books, U.S., 1st edition (1986). ISBN 0-935702-11-3.

[105] Christopher Foot. "Atomic Physics". OUP, 1st edition (2005). ISBN 0198506953.

[106] Yuyan Liu, Jieli Lin, Guangming Huang, Yuanqing Guo & Chuanxi Duan. *Journal of the Optical Society of America B*, **18**, 5 (2001) 666. ISSN 0740-3224. http://www.opticsinfobase.org/abstract.cfm?URI=JOSAB-18-5-666

[107] J J Olivero & R L Longbothum. *Journal of Quantitative Spectroscopy and Radiative Transfer*, **17** (1977) 233–236. http://www.sciencedirect.com/science/article/pii/0022407377901613

[108] Robert A Toth. *Applied Optics*, **32** (1993) 7326–7365. http://www.opticsinfobase.org/ao/abstract.cfm?URI=ao-32-36-7326

[109] Emmanuel Desurvire. *Lightwave Technology, Journal of*, **8**, October (1990) 1517–1527. http://ieeexplore.ieee.org/xpls/abs_all.jsp?arnumber=59191

[110] A G Fox & T Li. *Bell Syst. Tech. J*, **40**, 2 (1961) 453–488. http://mesoscopic.mines.edu/ mediawiki/images/6/62/Fox-Li1.pdf

[111] Martin A. Elliott, Gerge J. Nebel & Fred G. Rounds. *Journal of the Air Pollution Control Association*, **5**, 2 (1955) 103–108. http://www.tandfonline.com/doi/abs/10.1080/00966665.1955.10467686

[112] Thorlabs. "DET10C InGaAs Biased Detector User Guide", g edition (2013). http://www.thorlabs.de/thorcat/13100/DET10C-Manual.pdf

[113] L.S. Rothman, I.E. Gordon, R.J. Barber, H. Dothe, R.R. Gamache, A. Goldman, V.I. Perevalov, S.A. Tashkun & J. Tennyson. *Journal of Quantitative Spectroscopy and Radiative Transfer*, **111**, 15 (2010) 2139–2150. ISSN 00224073. http://linkinghub.elsevier.com/retrieve/pii/S002240731000169X

[114] S.M. Abrarov & B.M. Quine. *Applied Mathematics and Computation*, **218**, 5 (2011) 1894–1902. ISSN 00963003. http://linkinghub.elsevier.com/retrieve/pii/S0096300311009179

[115] Sandip Pal, Hugh McCann & K. B. Ozanyan. *Measurement Science and Technology*, **19**, 9 (2008) 094018.

[116] Lothar Wondraczek, Alireza Khorsandi, Ulrike Willer, Gerhard Heide, Wolfgang Schade & Guenther Heinz Frischat. *Combustion and flame*, **138**, 1 (2004) 30–39.

[117] Mordecai Avriel. "Nonlinear Programming: Analysis and Methods". Prentice-Hall, first edition (1976). ISBN 0-13-623603-0.

[118] "Safety data for carbon monoxide" (2003). http://physchem.ox.ac.uk/msds/CA/carbon_monoxide.html

[119] Y. Wang, J. W. Munger, S. Xu, M. B. McElroy, J. Hao, C. P. Nielsen & H. Ma. *Atmospheric Chemistry and Physics*, **10**, 18 (2010) 8881–8897. ISSN 1680-7324. http://www.atmos-chem-phys.net/10/8881/2010/

[120] J. C. Turnbull, A. Karion, M. L. Fischer, I. Faloona, T. Guilderson, S. J. Lehman, B. R. Miller, J. B. Miller, S. Montzka, T. Sherwood, S. Saripalli, C. Sweeney & P. P. Tans. *Atmospheric Chemistry and Physics*, **11**, 2 (2011) 705–721. ISSN 1680-7324. http://www.atmos-chem-phys.net/11/705/2011/

[121] Mark Goldstein. *Journal of emergency nursing: JEN : official publication of the Emergency Department Nurses Association*, **34**, 6 (2008) 538–42. ISSN 1527-2966. http://www.ncbi.nlm.nih.gov/pubmed/19022078

[122] Nicolas Docquier & Sbastien Candel. *Progress in Energy and Combustion Science*, **28**, 2 (2002) 107 – 150. ISSN 0360-1285. http://www.sciencedirect.com/science/article/pii/S0360128501000090

[123] Xiutao Lou, Gabriel Somesfalean & Zhiguo Zhang. *Applied Optics*, **47**, 13 (2008) 2392–2398. ISSN 0003-6935. http://www.ncbi.nlm.nih.gov/pubmed/18449306

[124] V.V. Liger. *Spectrochimica Acta Part A: Molecular and Biomolecular Spectroscopy*, **55**, 10 (1999) 2021–2026. ISSN 13861425. http://linkinghub.elsevier.com/retrieve/pii/S1386142599000748

[125] A. W. J. Thompson, J. H. Northern & P. Ewart. *Sensors and Actuators B: Chemical (To be published)*.

[126] G.B. Rieker, Jay B Jeffries & Ronald K Hanson. *Applied Optics*, **48**, 29 (2009) 5546–60. ISSN 1539-4522. http://www.ncbi.nlm.nih.gov/pubmed/19823239

[127] M Lindberg, Ove Axner U & Pawel Kluczynski. *Spectrochimica Acta Part B*, **56** (2001) 1277–1354.

[128] John H. Scofield. *American Journal of Physics*, **62**, 2 (1994) 129. ISSN 00029505. http://link.aip.org/link/?AJP/62/129/1&Agg=doi

[129] Andrew James McGettrick, Kevin Duffin, Walter Johnstone, George Stewart & David G. Moodie. *Journal of Lightwave Technology*, **26**, 4 (2008) 432–440. ISSN 0733-8724. http://ieeexplore.ieee.org/lpdocs/epic03/wrapper.htm?arnumber=4451270

[130] G. V. H. Wilson. *Journal of Applied Physics*, **34**, 11 (1963) 3276. ISSN 00218979. http://link.aip.org/link/JAPIAU/v34/i11/p3276/s1&Agg=doi

[131] D T Cassidy & J Reid. *Applied Optics*, **21**, 7 (1982) 1185–90. ISSN 0003-6935. http://www.ncbi.nlm.nih.gov/pubmed/20389829

[132] J. Henningsen & H. Simonsen. *Applied Physics B: Lasers and Optics*, **70**, 4 (2000) 627–633. ISSN 0946-2171. http://link.springer.com/10.1007/s003400050871

[133] G.B. Rieker. "Wavelength modulation spectroscopy for measurements of gas temperature and concentration in harsh environments". Ph.D. thesis, Stanford University (2009).

[134] Hejie Li, G.B. Rieker, Xiang Liu, JB Jeffries & RK Hanson. *Applied Optics*, **45**, 5. http://www.opticsinfobase.org/abstract.cfm?&id=87828

[135] K. Sun, X. Chao, R. Sur, J.B. Jeffries & R.K. Hanson. *Applied Physics B*, **110**, 4 (2013) 497–508. ISSN 0946-2171. http://dx.doi.org/10.1007/s00340-012-5286-0

[136] G.B. Rieker, H. Li, X. Liu, J.T.C. Liu, J.B. Jeffries, R.K. Hanson, M.G. Allen, S.D. Wehe, P.A. Mulhall, H.S. Kindle, A. Kakuho, K.R. Sholes, T. Matsuura & S. Takatani. *Proceedings of the Combustion Institute*, **31**, 2 (2007) 3041–3049. ISSN 15407489. http://linkinghub.elsevier.com/retrieve/pii/S1540748906001660

[137] G.B. Rieker, H Li, X Liu, J B Jeffries, R K Hanson, M G Allen, S D Wehe, P a Mulhall & H S Kindle. *Measurement Science and Technology*, **18**, 5 (2007) 1195–1204. ISSN 0957-0233. http://stacks.iop.org/0957-0233/18/i=5/a=005?key=crossref.5fffe8b40f523928fbe096f1cf33757d

[138] J. H. Northern, A. W. J. Thompson & P. Ewart. *To be published*.

[139] Rongrong Xu, Jiajia Pan, Lili Hu & Junjie Zhang. *Journal of Applied Physics*, **108**, 4 (2010) 43522. ISSN 00218979. http://link.aip.org/link/JAPIAU/v108/i4/p043522/s1&Agg=doi

[140] R. Xu, Y Tian, L. Hu & J. Zhang. *Applied Physics B*, **104**, 4 (2011) 839–844. ISSN 0946-2171. http://www.springerlink.com/index/10.1007/s00340-011-4461-z

[141] H. Gebavi, D. Milanese, R. Balda, S. Taccheo, J. Fernandez, J. Lousteau & M. Ferraris. *Journal of Luminescence*, **132**, 2 (2012) 270–276. ISSN 00222313. http://linkinghub.elsevier.com/retrieve/pii/S0022231311004893

[142] W J Zhang, Q Y Zhang, Q J Chen, Q Qian, Z M Yang, J R Qiu, P Huang & Y S Wang. *Optics Express*, **17**, 23 (2009) 20952–8. ISSN 1094-4087. http://www.ncbi.nlm.nih.gov/pubmed/19997333

[143] W. B. Liu, Y. P. Zeng, L. Wang, Y. Q. Shen, B. X. Jiang, J. Li, D. Zhang & Y. B. Pan. *Laser Physics*, **22**, 10 (2012) 1622–1626. ISSN 1054-660X. http://www.springerlink.com/index/10.1134/S1054660X12100155

[144] T Stacewicz & M Nowakowski. *Opto-Electronics Review*, **20**, 1 (2012) 26–39.

[145] A. A. Kosterev, P. R. Buerki, L. Dong, M. Reed, T. Day & F. K. Tittel. *Applied Physics B*, **100**, 1 (2010) 173–180. ISSN 0946-2171. http://link.springer.com/10.1007/s00340-010-3975-0

[146] D Richter, A Fried, B P Wert, J G Walega & F K Tittel. *Applied Physics B: Lasers and Optics*, **75**, 2-3 (2002) 281–288. ISSN 0946-2171. http://www.springerlink.com/openurl.asp?genre=article&id=doi:10.1007/s00340-002-0948-y